TURUN
YLIOPISTO
UNIVERSITY
OF TURKU

METAL COMPLEXES IN FLOW BATTERIES

Jenna Hannonen

TURUN YLIOPISTON JULKAISUJA – ANNALES UNIVERSITATIS TURKUENSIS
SARJA – SER. F OSA – TOM. 59 | TECHNICA – INFORMATICA | TURKU 2025

TURUN
YLIOPISTO
UNIVERSITY
OF TURKU

METAL COMPLEXES IN FLOW BATTERIES

Jenna Hannonen

TURUN YLIOPISTON JULKAISUJA – ANNALES UNIVERSITATIS TURKUENSIS
SARJA – SER. F OSA – TOM. 59 | TECHNICA – INFORMATICA | TURKU 2025

University of Turku

Faculty of Technology
Department of Mechanical and Materials Engineering
Materials Engineering
Doctoral programme in Technology (DPT)

Supervised by

Professor Pekka Peljo
University of Turku, Finland

Doctor Ulriika Mattinen
University of Turku

Reviewed by

Doctor Cristina Flox
Iberian Centre for Research in Energy Storage

Doctor Mathieu Etienne
LCPME-CNRS-University of Lorraine

Opponent

Professor Ulla Lassi
University of Oulu

The originality of this publication has been checked in accordance with the University of Turku quality assurance system using the Turnitin OriginalityCheck service.

ISBN 978-952-02-0190-6 (PRINT)
ISBN 978-952-02-0191-3 (PDF)
ISSN 2736-9390 (Print)
ISSN 2736-9684 (Online)
Painosalama, Turku, Finland 2025

UNIVERSITY OF TURKU
Faculty of Technology
Department of Mechanical and Materials Engineering
Materials Engineering
JENNA HANNONEN: Metal complexes in flow batteries
Doctoral Dissertation, 184 pp.
Doctoral Programme of Technology (DPT)
January 2025

ABSTRACT

There is an increasing need to develop energy storage materials to enable further utilization of renewable energy production. Energy storages are required due to the intermittency of solar and wind power, to add flexibility in the consumption. Flow battery (FB) is a promising energy storage technology to be integrated into renewable energy plants due to its many suitable characteristics. Abundant, environmentally friendly, and stable energy storage materials are needed for a cost-effective and competitive energy storage solution.

In this thesis, FB candidate materials were studied for their possible usage in flow battery applications. The material selection is abundant iron and titanium combined with easily tunable organic ligands to produce water-soluble metal complexes.

Metal complexes of iron with 2,2′-bipyridine, 1,10-phenanthroline, and 2,2′:6′,2′′-terpyridine, all with various functional groups, and titanium(IV) with 2,3-dihydroxynaphthalene were synthesized, characterized electrochemically via cyclic voltammetry and in lab-scale FB tests when applicable. Simulations were performed to obtain information on the kinetics of the redox pair from the experimental cyclic voltammograms. A commercial asymmetric $[Fe(II)(bpy)(CN)_4]^{2-}$ complex was also studied for flow battery applications.

Obtained redox potentials are sufficiently high (0.57 to 1.29V *vs.* SHE) for iron complexes to be utilized as posolytes for aqueous FB applications, while the titanium complex had a sufficiently low redox potential (–1.18 V *vs.* SHE) for usage as negolyte. In lab-scale flow battery studies, the symmetric iron complexes undergo side reactions leading to voltage drop and decreased energy efficiency, which is not detected for $[Fe(II)(bpy)(CN)_4]^{2-}$. Analysis of the voltammetry of $[Fe(II)(bpy)_3]^{2+}$ complexes by simulations revealed a counterion effect on the stability, while additional information on the kinetics of the redox process was obtained.

The complex decomposition mechanism of $[Fe(II)(bpy)_3]^{2+}$ led to the introduction of an in situ tool to monitor the battery electrolytes and their side reactions via the formation of other redox-active species during FB operation. The tool was also used to monitor the SOC of the redox active species during flow battery operation via half-cell OCP and simulations of CVs.

KEYWORDS: aqueous flow battery, electrochemistry, cyclic voltammetry, iron complex, simulations

TURUN YLIOPISTO
Teknillinen tiedekunta
Kone- ja Materiaalitekniikan laitos
Materiaalitekniikka
Jenna Hannonen: Metallikompleksit virtausakuissa
Väitöskirja, 184 s.
Teknologian tohtoriohjelma
Tammikuu 2025

TIIVISTELMÄ

Energiamateriaalien kehittämiselle on suuri tarve, jotta voimme käyttää enemmän uusiutuvia energialähteitä (tuuli- ja aurinkovoimaa) hyväksi. Näiden ajoittaisen saatavuuden takia tarvitsemme energiavarastoja, jotta voimme tasoittaa suuren energiakulutuksen huippuja suuren tuotannon huipuilla ja lisätä joustoa kulutukseen. Virtausakku on lupaava energiavarastoteknologia, joka voidaan integroida uusiutuvien energialähteiden voimaloihin monien sopivien ominaisuuksiensa puolesta. Yleisesti saatavilla olevia, ympäristöystävällisiä ja stabiileja energiamateriaaleja tarvitaan, jotta energiavarastosta saadaan kustannustehokas sekä kilpailukykyinen ratkaisu.

Tässä työssä tutkittiin metallikompleksien soveltuvuutta virtausakkuihin. Materiaalivalikoima oli yleinen rauta sekä titaani yhdistettynä orgaanisiin helposti muokattaviin ligandeihin, muodostaen vesiliukoisia metallikomplekseja.

2,2´-bipyridiinin, 1,10-phenantroliinin ja 2,2´:6´,2´´-terpyridiinin rautakompleksit useilla funktionaalisilla ryhmillä sekä titaanikompleksi 2,3-dihydroksinaftaleenilla syntetisoitiin, karakterisoitiin sähkökemiallisesti syklisen voltammetrian avulla sekä laboratoriomittakaavan virtausakussa tarvittaessa. Syklisiä voltammogrammeja (CV) simuloitiin saaden tietoa redox-parin kinetiikasta. Kaupallista asymmetristä $[Fe(II)(bpy)(CN)_4]^{2-}$-kompleksia tutkittiin myös.

Mitatut rautakompleksien redox-potentiaalit olivat sopivia (0.57–1.29V *vs.* SHE) ajatellen käyttöä virtausakuissa posolyyttinä, ja titaanikompleksin (–1.18 V *vs.* SHE) negolyyttinä. Laboratoriomittakaavan virtausakkututkimuksissa symmetriset rautakompleksit kävivät läpi sivureaktioita huonontaen akun energiatehokkuutta sivureaktiotuotteiden alhaisemman purkupotentiaalin takia. Vastaavia sivureaktioita ei havaittu $[Fe(II)(bpy)(CN)_4]^{2-}$-kompleksille. $[Fe(II)(bpy)_3]^{2+}$-kompleksien simulaatioista huomattiin vastaionin vaikutus kompleksin stabiilisuuteen, ja simulaatiomallia käytettiin myös redox-parien kinetiikan analysoimiseen.

Elektrolyyttejä karakterisoitiin akun ajon aikana CV:iden avulla analysoiden samalla puolikennojen varaustiloja puolikennopotentiaalien ja simulaatioiden avulla. Täten elektrolyyttien itsepurkautumisesta sekä redox-aktiivisten molekyylien rakennemuutoksista akkuajon aikana saatiin tietoa, mikä on erityisen hyödyllistä monimutkaisten systeemien kohdalla.

ASIASANAT: rautakompleksi, simulaatiot, syklinen voltammetria, sähkökemia, vesipohjainen redox-virtausakku

Table of Contents

Abbreviations

Ag/AgCl	silver/silver chloride electrode
AZON3	5-oxo-2-(3-(trimethylammonio)propyl)-5H-indeno[1,2-c]pyridin-2-ium bromide
bpy	2,2´-bipyridine
CC	constant current
CCCV	constant current and constant voltage
CE	counter electrode, when talking about cyclic voltammetry, or coulombic efficiency, when talking about flow battery performance
CV	cyclic voltammetry or cyclic voltammogram
$E^{0'}$	formal potential, redox potential of redox pair
EC	electrochemical reaction followed by chemical reaction
EDG	electron-donating group
EE	energy efficiency
EWG	electron-withdrawing group
FB	flow battery
HER	hydrogen evolution reaction
I	current
ncat	naphthacatechol, aka 2,3-dihydroxynaphthalene
NMR	nuclear magnetic resonance
OER	oxygen evolution reaction
OCP	open cell potential
OCV	open circuit voltage
ox	oxidized/oxidation
pH	potential hydrogen, a measure of hydrogen ion (proton) concentration in a substance
phen	1,10-phenanthroline
PVC	polyvinyl chloride
Q	charge
RE	reference electrode
red	reduced/reduction
redox	reduction and oxidation together as one process

RSD	relative standard deviation
SHE	standard hydrogen electrode
SOC	state of charge
terpy	2,2′:6′,2′′-terpyridine
UV-Vis	ultraviolet-visible light (spectroscopy)
V	voltage
VE	voltage efficiency
WE	working electrode
[Ar]	the electron configuration of Argon, $1s^2 2s^2 2p^6 3s^2 3p^6$

List of Original Publications

This dissertation is based on the following original publications, which are referred to in the text by their Roman numerals:

I Hannonen, J., Kiesilä, A., Mattinen, U., Pihko, P. M., and Peljo, P. Electrochemical characterization of redox activity and stability of various tris(2,2‘-bipyridine) derived complexes of iron(II) in aqueous solutions. *J. Electroanal. Chem.*, 2023; 950.

II Hannonen, J., Tuna, A., Gonzalez, G., Martínez González, E., and Peljo, P. Investigation of Fe(II) Complexes with 1,10-Phenanthroline and 2,2';6',2"-Terpyridine for Aqueous Flow Battery Applications. *ChemElectroChem*, 2025, 12, e202400574.

III Mehranfar, A., Hannonen, J., Tuna, A., Jafarishiadeh, M., Kiesilä, A., Pihko, P., Peljo, P. and Laasonen, K. Computational Evaluation of Redox Potentials of Metal Complexes for Aqueous Flow Batteries. *ChemPhysChem*, 2025, 2500046.

IV Nechaev A. A., Gonzalez, G., Verma, P., Peshkov, V. A., Bannykh, A., Hashemi, A., Hannonen, J., Hamza, A., Pápai, I., Laasonen, K., Peljo, P., Pihko, P. M. Exploration of Vitamin B6-Based Redox-Active Pyridinium Salts towards the Application in Aqueous Organic Flow Batteries, *Chem. Eur. J.,* 2024, e202400828.

V Hannonen, J., Jarju, J., Gonzalez, G., Martinez, E., Peljo, P. State of charge and decomposition mechanism analysis via cyclic voltammetry during flow battery operation. Submitted.

1 Introduction

Amidst the global energy crisis, options for enabling the green shift are required to be able to use renewable energy sources and diminish the use of fossil fuels. Renewable energy sources such as wind and solar energy have a problem with their intermittency: solar energy can be obtained on sunny days, and wind energy on windy days and nights. The advantage of fossil fuels is their availability when needed. Therefore, we need to make renewable energy a more practical option as the main energy source and available every hour of the day. This can be achieved by introducing energy storage to even out the energy consumption peaks, hence making renewable energy available all the time. Energy storages enable us to store the renewable energy when we have excess production and release it when we are producing less than what the consumption would be. This way, we are enabling the green shift away from fossil fuels by making the use of renewable energy sources more practical.

The flow battery (FB) is a promising technology for energy storage. The need to develop suitable molecules for the FB technology is growing to compete with other technologies. Understanding the characteristics of these energy-storing molecules to design suitable ones for flow battery operation, as well as understanding how their behavior changes during battery operation, are both important factors. They help us gain knowledge for the future design of energy-storing materials in FBs.

The purpose of this thesis is to screen computationally promising candidates in terms of redox potential, obtain information on their suitability for flow battery applications experimentally and via simulations, and understand the flow battery operation of the developed posolytes via characterizing the redox species present during the flow battery operation. The material selection of metal complexes with organic ligands and iron and titanium as metals originates from the abundance of these materials, leading to possibly a cost-effective, tunable, and scalable solution with an aqueous electrolyte.

Screening of redox-active molecules includes iron(II) complexes with organic ligands with various side groups. Iron(II) complexes with 2,2′-bipyridine (bpy) ligands were studied primarily (**publication I**) with experimental screening of redox potentials and investigation of the kinetics of the redox process via simulations, after

which the best-performing molecule was studied in a lab-scale flow battery. For the second study (**publication II**), 1,10-phenanthroline (phen) and 2,2′:6′,2′′-terpyridine (terpy) were studied with various functional groups. Redox potentials were obtained, as well as information on the kinetics and characteristics of the redox process, and cyclability and stability in a lab-scale flow battery for the best-performing compounds. The third study included in this thesis (**publication III**) is a computational paper, where my part was providing experimental redox potential values for metal complexes. In **publication IV**, my part was to analyze the number of electrons involved in the redox process. The final part of my thesis (**publication V**) concentrated on characterizing redox-active species during FB operation by utilizing CVs and UV-Vis. SOC analysis was performed via half-cell OCP and COMSOL simulations. We obtained information on the self-discharge of the compounds in storage tanks and chemical reactions involved in capacity decay. Additionally, information on the redox active species and its structural changes was obtained, proving to be especially useful in characterizing complex systems, such as $[Fe(II)(bpy)_3]^{2+}$.

2 Overview of storing energy in metal complexes for flow batteries

2.1 Storing energy

Energy can be stored in many ways: chemically, thermally, electrochemically, etc. The food we eat contains energy bound in chemical form, and breaking the bonds in the food gives us energy. Thermal energy can be a water tank next to a sauna, which is charged when the sauna is on and heats the water. This water can be used to warm us and the house by radiating thermal energy, regardless of the low energy efficiency via losses via conduction and convection. Potential energy can be stored, for example in water supplies at higher ground and discharged when let flow down through turbines for electric energy production. Electrochemical energy is charged by moving electrons from one place to another by using energy, then discharging the electrons by letting them flow spontaneously. The latter one is what this thesis is focused on, the movement of electrons to one place upon charge, and discharge when electrons return spontaneously to their original place. This can also be described as changing electric energy into chemical energy upon charge, and back to electric energy via discharge.

The first thing that comes to mind when thinking about electrochemical energy storage is usually batteries, and to be more exact, lithium-ion batteries[1]. They are everywhere in consumer products: phones, laptops, spare batteries, etc. However, lithium-ion battery is not the most suitable for all applications. Therefore, there are many other energy storage technologies to fill the gaps, such as flywheels[2], compressed air[3], hydro storage[4], supercapacitors[5], and lead-acid batteries[6]. All have their pros and cons and suitability for different applications.[7–11]

Energy storage can indirectly improve the living conditions on Earth. This is achieved by maintaining the health of nature since that is the one giving us living creatures our lives and health. Climate change is threatening that, and one way to fight for the globe to stay liveable is to stop using fossil fuels due to their pollutants released into the air.[12] Utilizing more and more renewable energy is inevitable for the green shift, but due to the intermittency of renewable energy,[9] we cannot access the energy whenever needed. Solar energy is available only on sunny days and wind energy on windy days and nights. To enable the green shift, we need to change the

approach we have to producing energy and incorporate energy storages into renewable energy plants.

At the moment, we are producing energy based solely on consumption; when we need to use energy, we use it, regardless of the source of it. However, the green shift requires us to take on a new approach. We need to be more flexible on the consumption, and use energy storages. Flexibility on consumption means using the energy when it is more available, available from renewable sources, and when it is economically a good option. Integrating energy storages to the renewable energy plants, evens out the consumption peaks by discharging energy from the renewable energy sources, hence adding flexibility. These actions reduce the usage of fossil fuels and increase the usage of renewable energy sources, hence enabling the green shift.

Energy storages come in many shapes and sizes, as briefly mentioned earlier. To incorporate energy storage into a renewable energy plant, it is required to store the energy efficiently and enable full charge and discharge, while also having a suitable amount of energy to be stored and the power at which we can charge and discharge. The size of the energy storage is not an important criterion, since these energy plants are usually located further away. Safety of the technology is an important criterion, as well as the levelized cost and ecological endurance of the energy storage. Flow battery fulfils all these criteria as discussed next.

2.2 Flow battery

Redox flow cell was originally introduced by Thaller 50 years ago as an energy storage technology.[13] In the 1970s energy crisis, flow battery was developed by NASA.[14–16] Since then, there have been a lot of studies to find suitable redox-active molecules for this energy storage technology. The first metal complex to be studied in a flow battery was ferricyanide in 1979,[17] and it has been the best-performing metal complex since then. Vanadium flow batteries, however, are the state of the art among flow battery materials, developed since the 1980s.[18] Their stability exceeds 200 000 cycles.[19,20] Regardless of the toxicity of the V(V) oxidation state and the non-abundancy of vanadium, vanadium flow batteries have been commercialized.[19] Using rare vanadium is questionable on a large scale, since some countries, like China, produce most of the vanadium, which is classified as a critical raw material by the European Union.[21] It is also an ingredient in making steel alloys, therefore, market changes in steel affect the price of vanadium, making it sensitive to changes.[22] These facts open the window to expand the material selection beyond vanadium. Recently, other compounds have been studied, such as organic molecules and metal complexes for posolytes and negolytes,[23–25] to find more cost-effective and

sustainable flow battery materials, of which iron complexes are promising due to their suitable redox potentials and the tunability of the ligands.[26–29]

Flow battery (FB) involves a flow of the electrolytes (negolyte and posolyte) from the reservoir tanks to the cell, where the charging and discharging of the redox active materials take place with the electrodes in the cells. Posolyte is oxidized during charge and negolyte is reduced during charge. During discharge, the opposite reactions occur spontaneously, hence releasing electron flow to the load. The membrane separates the posolyte and negolyte in the cell chambers, not allowing the redox active materials to mix and therefore preventing a shortcut of the battery. Typically, posolyte and negolyte are chosen to have the same molecular charge, and a membrane is chosen based on that: anion-exchange membrane for positively charged molecules and cation-exchange membrane for negatively charged molecules. This way the cross-over leading to capacity decay should stay minimal, while the conductivity between the solutions is enabled, allowing the cell to function with better efficiency due to smaller ohmic drop (**Fig 1.**)

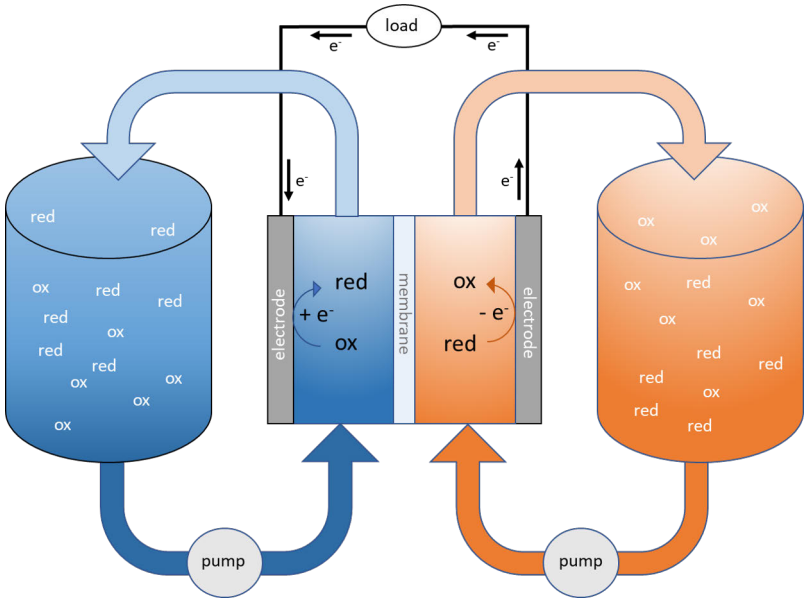

Figure 1. Schematic picture of an FB. Storage tanks are located on the sides and the cell with electrodes and membrane in the middle. Pumps enable the flow of electrolytes to the cell, where the energy-storing material is charged and discharged with redox reactions via applied potential.

As mentioned, the electrolytes are charged and discharged in the cell. The cell consists of end plates, current collectors, gaskets or flow frames, electrodes, and membrane when moving from outside parts to inner parts. The schematic picture of

the cell and its parts is in **Fig 2**. The experimental set-up with material selection is discussed later.

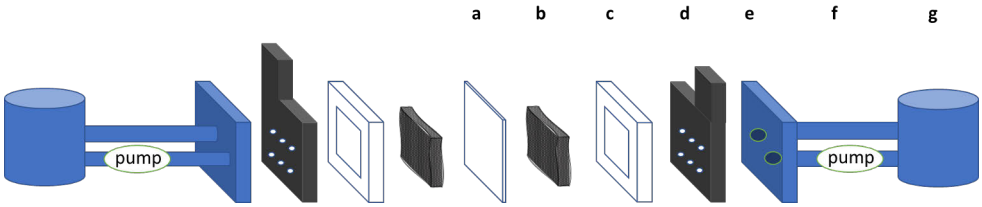

Figure 2. Schematic picture of the cell. **a.** membrane, **b.** electrode, **c.** flow frame, **d.** current collector/bipolar plate, **e.** end plate, **f.** tubing and pump, **g.** storage tank.

FB has energy tied into a less energy-dense liquid compared to if the energy were tied into solid material. Therefore, FB with the same energy capacity as a lithium-ion battery, is larger due to the larger storage tanks needed to store the amount of energy. However, the larger size of the storage tanks is not considered a problem in a stationary application. The battery energy storage capacity of the FB can be improved by simply increasing the volume of the tank. In case of the battery power, cells of the electrodes can be added or the electrode active area increased to obtain a higher power output. Aqueous FBs are safer than lithium-ion batteries in terms of possible problems in the operation of the batteries.[30–32] The maintenance of the cells and tanks can be done separately from each other since they are physically separated in the energy storage. Recycling the electrolytes is, in theory, easier than within solid composites in lithium-ion batteries, and some solutions have started to surface. Since f. ex. in vanadium flow batteries, no vanadium is consumed, therefore it is possible to recycle it in the future.[33] Also, electrodes in FBs can be changed independently of the tanks, if needed. Recycling and purifying the electrolytes and electrodes enhances the lifetime of the FB, which is excellent: up to 20 years[34] and 10 000 to 15 000 cycles.[35] Even up to 200 000 cycles have been reported for a vanadium flow battery in Japan.[20] With the right material selection, the environmental aspects of FBs can be improved even further by utilizing aqueous electrolytes with abundant and sustainable options. Additionally, the synthetic routes of the compounds should follow green chemistry principles when produced on a large scale. Abundant materials also have the potential to be cost-effective, therefore leading to a competitive energy storage solution price-wise. All this gives FB a fighting chance to be a real competitor in the energy storage markets in the future.

2.2 Metal complexes

The material selection in this work is metal complexes. Their structure is briefly explained, followed by the justification of the material selection and later factors affecting their design for flow battery applications.

Metal complexes consist of a central metal ion and ligands coordinated with the metal ion. Transition metal ion has free orbitals, and ligands have free electron pairs. A coordination bond is formed when the ligands give a lone electron pair to a free orbital of the metal ion (**Fig 3**). The coordination number and the number of ligands connected to a metal center differ based on the size, charge, and electron configuration of the metal ion and the ligands. Ligands affect the electron configuration of the complex; therefore, metals may have different coordination numbers.[36]

Figure 3. Metal ion´s empty hybrid atomic orbital and the ligand´s lone electron pair in a hybrid atomic orbital result in a coordinate covalent bond. Figure based on ref 36.[36]

The electron configuration of iron(II) is $[Ar]4s^0 3d^6 4p^0$. When the oxidation of iron(II) to iron(III) occurs, the electron leaves the 3d orbital, leaving the electron configuration of $[Ar]4s^0 3d^5 4p^0$. As a result, the forming Fe(III) complex is paramagnetic due to non-paired electrons in the structure, whereas iron(II) can be considered diamagnetic due to 6 electrons with the used ligands organized in pairs at the lower energy level orbitals of t_{2g}, due to splitting of the energy levels on the 3d orbital: t_{2g} at lower energy (3 orbitals) and e_g at higher energy (2 orbitals).[36]

The coordination number of Fe(II) and Fe(III) is generally 6. The electron-vacant orbitals marked in the electron configuration will get electron density from the ligands. However, the electrons will remain associated in the ligands in the atoms providing the electrons for the sigma bonds between the iron and the ligand.[36]

As mentioned, iron has 6 coordination sites, leading to an octahedral structure. Examples of monodentate ligands forming hexacomplexes with Fe include H_2O, Cl^- and CN^-. 2,2´-bipyridines and 1,10-phenanthrolines have two nitrogens per ligand and both nitrogens have one free electron pair each. Therefore, they are bidentate ligands: they can coordinate with both nitrogen atoms to the iron center. Three bpy ligands can be coordinated simultaneously to iron center ion to occupy all its coordination sites. 2,2´:6´,2´´-terpyridine has 3 lone electron pairs per ligand (one e^- pair in each nitrogen). They are tridentate ligands, therefore, only two such ligands are sufficient to coordinate to iron(II) and iron(III) fully. If one of the ligands breaks

off, the free coordination sites can be used to coordinate water molecules or other possible ligands in the solution.

The reason for material selection, including Fe and the mentioned organic ligands, lies in the abundance and therefore cost-efficiency of these materials, hence making the possible final storage solution cost-efficient. Ligands are tunable, and the synthesis of the metal complexes could be scalable. The compounds can be synthesized in a relatively environmentally friendly manner, as the yield exceeds 97 % in organic solvents, and the synthesis of some of the studied compounds can also be performed in water. At least for primary screening of the redox potentials of the formed compounds, the latter can be a good option with as small an amount of ligand and iron salt as possible.

2.2.1 Brief history of iron complexes in flow batteries and comparison to organic molecules

Metal complexes have been studied for flow batteries earlier, however, only the history relevant to the studied materials is discussed here, focusing therefore on the selected ligands and their iron complexes.

Fe(II) complexes with bipyridine have been known since 1898, when their coordination chemistry was discovered, as well as the ability of $[Fe(II)(bpy)_3]^{2+}$ to be oxidized,[37] only 10 years after the synthesis of the bpy.[38] The redox ability of Fe compounds took three more decades to be discovered, occurring in 1931.[39] This acted as a boost to research iron complexes electrochemically.

The study of metal complexes with bpy for FBs started in 1988 with $[Ru(II)(bpy)_3]^{2+}$.[40] In recent years, other metals have also been complexed with bpy and bpy-based ligands, like phen, to be studied for FB applications.[41–45] Interest in using bpy, phen, and terpy as ligands is due to the sufficiently high redox potentials of the formed iron complexes, hence suitable for posolyte materials in FBs. The redox potential of aqueous $Fe^{2+/3+}$ is 0.77 V *vs.* SHE,[46] but when complexed with phen and terpy, the redox potential is 1.06 V *vs.* SHE for both iron complexes.[47] When Fe(II) is complexed with bpy, the redox potential increases to 1.08 V *vs.* SHE, and with functional group design of bpy (adding 4,4′-carboxylate (Dc) to the ligand), the redox potential of $[Fe(II)(Dcbpy)_3]^{4-}$ can reach 1.18 V *vs.* SHE.[46,48,49]

Some exceptionally well-performing iron complexes have been reported for flow battery applications. The best performing one regarding stability during cycling is still $[Fe(II)(CN)_6]^{4-}/[Fe(III)(CN)_6]^{3-}$ developed in the 1970s,[17] regardless of its rather low redox potential (0.358 V *vs.* SHE).[46] It has a stable FB performance with 100 % capacity retention in optimized conditions,[50] but applications are limited to neutral and alkaline pH.[51]

Certain $[Fe(II)(bpy)_3]^{2+}$ derivatives, such as $[Fe(II)(Dcbpy)_2(CN)_2]^{4-}$ with asymmetric ligand design of Dcbpy and CN ligands,[48] and $[Fe(II)(Bhmbpy)_3]^{2+}$ (tris(4,4′-bis(hydroxymethyl)-2,2′-bipyridine) iron),[52] are among the best-performing iron complexes available now, regardless of the slow dimerization of $[Fe(II)(Bhmbpy)_3]^{2+}$. Their capacity decays are 0.217 % per day (0.00158 % per cycle) and 0.07 % per day (0.0007 % per cycle), respectively.[48,52] Both are excellent values, but do not compare to hexacyanoferrate stability.

When comparing these to some of the best organic molecules in FBs, the iron complexes compete in solubility and hence in the obtained energy density of the FB. Asymmetric ligand design yields solubilities of 1.22 M $M_4[Fe(II)(Dcbpy)_2(CN)_2]$ (M = Na, K),[48] while solubilities as high as 1.91 M in water were reached with symmetric ligands when optimizing the counteraction.[50] Organic molecules are smaller, and when water-solubilizing groups are added, solubilities of 2.2 M in water are reached, for example, with 1,8-bis(2-(2-(2-hydroxyethoxy)ethoxy)-ethoxy)anthracene-9,10-dione (AQ1,8-3E-OH).[53] While metal complexes compete in solubility, they usually store only one electron, whereas some organic molecules can have a 2-electron transfer in one step. In these cases, the organic molecule would obtain a higher energy density and an advantage in competing in FBs if its other parameters, such as redox potential, capacity decay, etc., were suitable.

A smaller size of organic molecules can cause a problem related to the crossover of the active species, resulting in capacity decay. Cross-over is slower for metal complexes, as they are larger, giving an advantage in utilizing metal complexes in long-term energy storage. Redox potentials of metal and organic compounds are comparable and adjustable, hence not giving an advantage to either one regarding cell potential or power of the FB. In general, comparison of these materials is difficult because lab-scale FBs are tested in very different conditions (capacity utilization, current/voltage cycling, pH, etc.) and very different flow battery set-ups (electrodes, membranes, flow rates, etc.). Additionally, costs are difficult to estimate, as synthesis is done on a small scale, and starting material costs are higher than those of larger quantities. FB field is such a new field that there are no standardized battery testing methods, which makes the performance difficult to compare between different electrolyte materials. Still, both organic molecules and metal complexes have a lot of potential for FBs.

In this thesis, the focus is solely on metal complexes, as they can be a competitive solution for FBs and cost-effective when considering organic ligands and abundant metals. Metal complex design can lead to a low capacity decay and good solubility with a suitable redox potential in FB applications for the metal complexes, and their crossover is slow. The design of the metal complexes for this thesis work is discussed next.

2.2.2 Metal complex design for flow batteries

Metal complex design for flow batteries includes obtaining a sufficiently high redox potential (or sufficiently low if considering negolytes), good solubility in the chosen electrolyte to increase the energy density, as well as stability in both stages of redox reaction. Theory of the chemistry behind them, experimental solutions from literature, and computational tools can be utilized to evaluate these characteristics before experimental work. Computational work in finding redox potentials of metal complexes is rather reliable, as will be discussed later. Tuning the redox potential via functional groups and things affecting the solubility are known rather well in the literature. We can use simulations to estimate the decomposition rates from the cyclic voltammograms, but the most reliable method is to study the compounds experimentally in a lab-scale flow battery to determine the characteristics and stabilities of the redox species.

2.2.2.1 Redox potential

Redox potential is usually approximated to be the halfway potential, aka the mean value of the oxidation and reduction peaks in potential. This is evaluated based on the oxidation and reduction peak placement in a cyclic voltammogram presented later, with the measurement technique in question. Regarding posolytes in flow batteries, we are expecting the redox potential to be as high as possible, considering the electrolyte stability window, to obtain a suitable cell potential for the flow battery.

Ligands affect the electron density of the metal ion center, as do the functional groups of the ligand. The electron-withdrawing groups (EWG) in the ligand make the electron density less dense at the metal ion, therefore making the oxidation of the compound harder. Therefore, these kinds of functional groups change the redox potential of the metal complex to a more positive potential, as their electronegative parts draw electrons from the ligand towards themselves, further from the metal ion center. Electron-donating groups (EDG) push electrons toward the metal ion center, hence making the metal ion environment more negative. Therefore, in these kinds of metal complexes, oxidizing the metal ion becomes easier as it is energetically more favorable. Hence, the redox potential lies at less positive potentials than that of the non-substituted metal complex.

The ligands themselves are always donating the electron pair to the metal ion for the coordination bond, but there is a difference in their distribution between the ligand and the metal ion. The differences in the electronegativity between the ligand and metal ion cause differences in the electron density near the metal center, which then dictates the redox potential of the metal complex. The functional groups in the ligands affect this, but of course, the parent ligand itself is mainly responsible.

The size of the ligand is also one thing to consider, since the larger the ligand is, the further the metal complex is from the electrode during electron transfer. Large separation between oxidation and reduction peak potentials seen in the cyclic voltammogram due to slow kinetics of the electron transfer can lead to charge and discharge plateau separation in the flow battery applications, hence decreasing the energy efficiency of the energy storage. Large ligands might, on the other hand, shield the metal ion center from undergoing side reactions and therefore improve the stability of the active material during redox reactions. The functional groups also affect the ligand size, and if positioned well, they take part in shielding the iron ion center from attacks via steric hindrance.

2.2.2.2 Solubility

To increase energy density in FBs, the metal complexes need to have good solubility in the used solvent, in this thesis work, in water with salt. When dissolving something into water, which has a dipolar nature, the dissolved compound also needs to be polar, aka have a dipole moment. The dipole moment is achieved when the molecule has a positive center of charge and a negative center of charge, or several of these within a molecule. The bonds need to have an uneven distribution of electrons inside the molecule, caused by different electronegativity values, where some elements pull electrons more strongly towards themselves than others. In the case of a symmetric molecule, the opposed polarities of the bonds might cancel each other, in case the bond dipoles are of opposite directions. For example, when a symmetric compound has a charge (characteristic of metal complexes), the dipole moment is present if the bond dipoles point in the same place. In the case of metal complexes, the metal ion is positively charged, therefore, the bond dipoles point toward it, leading usually to dipole moment and water-solubility of the compound. If the bond dipoles all point away from each other and the molecule is symmetric, the compound does not have a dipole moment, but usually neither charge. The dipole moment gives the charge distribution of the molecule, and this electric behavior is necessary to be able to dissolve a metal complex into water.

In the synthesis of the metal complex, we are aiming for charged metal complexes when taking into account the charge of the metal ion and the neutral or charged state of the ligands. Functional group design to enhance the charge of the compound in terms of solubility can be taken into account, with for example deprotonated COOH groups, that can change the charge of the complex to a larger negative charge as in $[Fe(II)(Dcbpy)_3]^{4-}$ (charge upon deprotonation –4) compared to the charge of the unsubstituted $[Fe(II)(bpy)_3]^{2+}$ complex that has charge of +2. In general, the charge of the metal complex usually leads to a dipolar nature, unless the functional groups change the charge of the metal complex to 0 and the metal complex

structure were to be also symmetrical. Another strategy to enhance the asymmetry in the molecule and therefore improve the dipolar nature of the metal complex is to incorporate different kinds of ligands into the metal ion to complement the asymmetry of electron distribution in the metal complex structure. Carnelley´s rule[54] dictates that asymmetric compounds have better solubility than symmetric ones. The reason for better solubility is that asymmetric solid crystals have lower energies, hence, less energy is needed to dissolve them than if the crystal were very stable. Therefore, an asymmetric structure should be aimed for in the metal complex design to increase the energy density of the final energy storage.

When the metal complexes are synthesized, the metal salt can play a role in terms of the performance of the synthesized metal complex in the solution, since it gives the counterion to the metal complex ion. If the counterion is bonding strongly to the metal complex, it might be harder for the compound to dissolve. For the iron salts, the counterions used in the thesis work were tetrafluoroborate (BF_4^-), sulfate (SO_4^{2-}), and chloride (Cl^-). The tetrafluoroborates cause side reactions with the bpy ligands of $[Fe(II)(bpy)_3]^{2+}$, therefore participating in the decomposition of these complexes.[55] Another challenge with tetrafluoroborate is that the fluoride can be substituted with a hydroxide, therefore causing the formation of HF. $B(OH)_4^-$ also possesses low solubility, which might lead to precipitation out of the solution. Chloride ions, on the other hand, have good solubility and were utilized towards the end of the lab work as counterions for the iron complexes during synthetic steps. Sulfates can also be used, since a larger ionic size compared to chlorides might enable faster dissociation from the complex ion due to being further from the complex than chloride.

2.2.2.3 Side reactions limiting the FB operation

The side reactions are considered as unwanted chemical reactions that are not part of the preferred main reaction. In the best case, side reactions can be self-discharge reactions with oxygen, but in the worst case, they lead to irreversible decomposition of the active species. In FBs, these reactions are usually decomposition reactions that break down the redox active structure or change it into something else that is not beneficial in the FB operation. These reactions can be irreversible or reversible, as they can also create non-redox-active or redox-active compounds. We are next going through the relevant side reactions regarding this thesis work.

As the starting material, we have the ligands coordinated to the center metal ion. The preferred reaction is the electrochemical redox reaction, where the iron(II) center oxidizes by giving an electron away, and later reduces and receives an electron, without any further chemical reactions. This would be the ideal case and we would have a stable FB operation. However, the iron(II) complexes studied in

this thesis seem to undergo chemical reactions in most cases. Below are the expected chemical reactions to occur to the studied iron(II) complexes presented in **Fig 4**. Below the figure, the equations are given, which are referred to later when discussing the iron complex stability

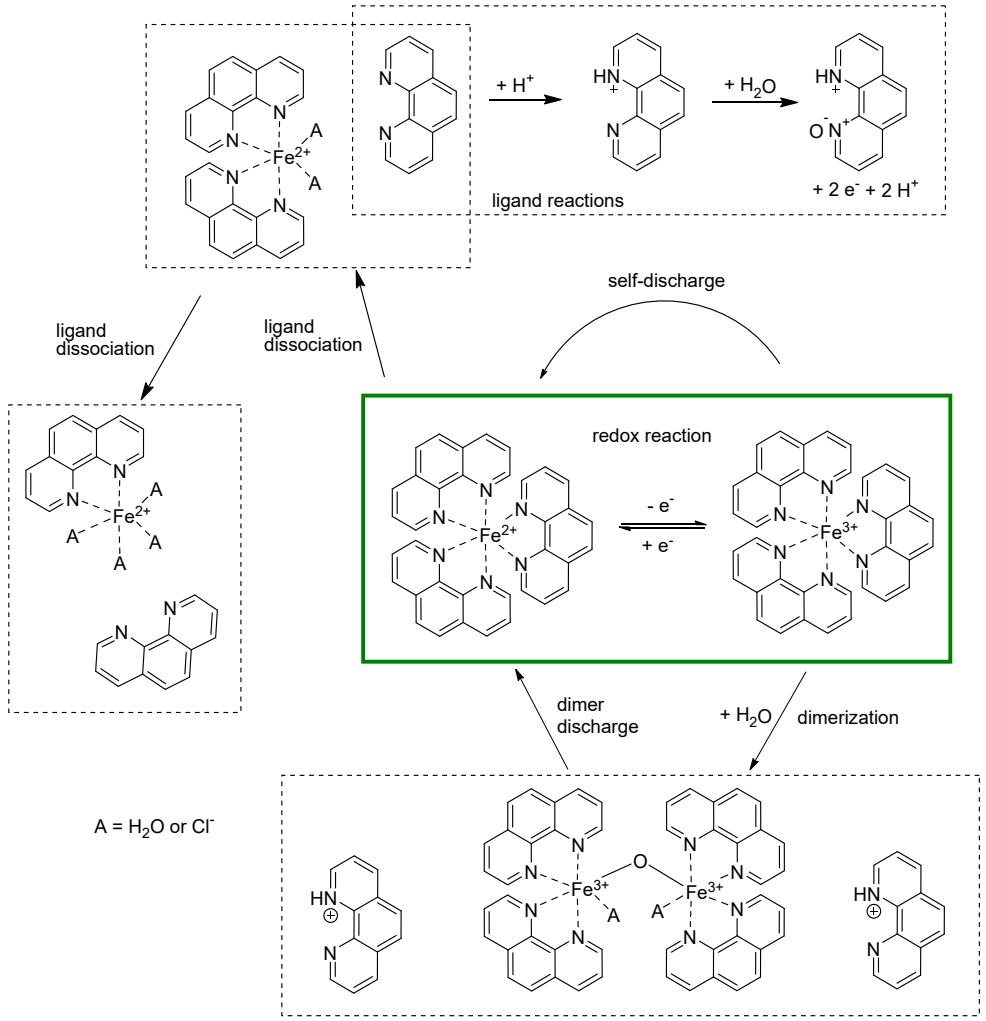

Figure 4. Electrochemical reaction and side reaction routes are demonstrated with $[Fe(II)(phen)_3]^{2+}$. The decomposition mechanism corresponds to the one presented in the literature for $[Fe(II)(bpy)_3]^{2+}$ and its derivative $[Fe(II)(D(CH_2OH)\text{-}bpy)_3]^{2+}$ in refs [52,56], which follow our results.[v]

The equations, including all participants in the side reactions, are given below. (i) is the main redox reaction. (ii) shows the ligand dissociation with the release of protonated ligands. (iii) to (iv) show the dimerization starting from a nucleophilic

attack of the water molecule. (v) shows the dimer reduction (reduction is an electrochemical process, reorganization of ligands to Fe(II) center a chemical process). (vi) represents the oxidation of the ligand with self-discharge of the monomer. Free ligand reactions are implemented in reactions (ii)-(iii) and (v)-(vi). Water molecules and chlorides are competing for the free coordination sites, and therefore, the free coordination sites in the following equations could be occupied by either chloride or water molecules, altering the equations in those parts. Reactions are written and graphed according to literature references[52,56] describing the decomposition mechanisms of $[Fe(II)(bpy)_3]^{2+}$ compounds.

$$\left[\mathrm{Fe^{(II)}}L_3\right]^{2+} \overset{k^0}{\rightleftarrows} \left[\mathrm{Fe^{(III)}}L_3\right]^{3+} + e^- \quad \text{(i)}$$

$$\left[\mathrm{Fe^{(II)}}L_3\right]^{2+} + H^+ + 2\,Cl^- \rightarrow \left[\mathrm{Fe^{(II)}}L_2\right]Cl_2 + H(L)^+ \rightarrow$$

$$[\mathrm{Fe^{(II)}}L_1(OH_2)_2]Cl_2 + H(L)^+ \quad \text{(ii)}$$

$$\left[\mathrm{Fe^{(III)}}L_3\right]^{3+} + H_2O \rightarrow \left[\mathrm{Fe^{(III)}}L_3(OH)\right]^{2+} + H^+ + Cl^- \rightarrow$$

$$\left[\mathrm{Fe^{(III)}}L_2Cl(OH)\right]^{+1} + HL^+ \quad \text{(iii)}$$

$$2\left[\mathrm{Fe^{(III)}}L_2Cl(OH)\right]^{+1} + H_2O \rightarrow \mu\text{-}O\text{-}[\mathrm{Fe^{(III)}}L_2(H_2O)]_2^{4+} + Cl^- \quad \text{(iv)}$$

$$\mu\text{-}O\text{-}[\mathrm{Fe^{(III)}}L_2(H_2O)]_2^{4+} + 2\,HL^+ + 2\,e^- \rightarrow 2\left[\mathrm{Fe^{(II)}}L_3\right]^{+2} + 2\,H_2O \quad \text{(v)}$$

$$2\left[\mathrm{Fe^{(III)}}L_3\right]^{3+} + HL^+ + H_2O \rightarrow 2\left[\mathrm{Fe^{(II)}}L_3\right]^{2+} + H(L-O)^+ + 2\,H^+ \quad \text{(vi)}$$

Regarding side reactions, in aqueous solutions, metal complexes are always prone to water´s nucleophilic attacks on the metal ion center, while the attack can be performed by a chloride ion, for example, too, depending on the supporting electrolyte salt. In this work, the electrolyte is mostly 0.1 M NaCl. The concentration of the analyte is a considerable factor since the higher its concentration, the more we are pushing the side reactions to occur. The lower the concentration, the less interaction there is between the molecules, and therefore, fewer side reactions should occur. Another important factor to consider is that the side reaction products might give out protons; for example, that might make other side reactions more favorable, therefore, accelerating the consumption of the redox species. pH can be seen to affect the self-discharge reaction, for example.

The reversibility of the side reactions is favorable if they exist; however, for example, the discharge of the dimer occurs at a lower voltage than the charge of the monomer, hence leading to poor energy efficiency, while side reactions also lead to a capacity decay.

2.3 Characterization of flow battery materials

Characterization can be performed before, during, and/or after flow battery operation. Next, some of the characterization techniques used in this thesis are discussed.

2.3.1 Cyclic voltammetry and simulations

Cyclic voltammetry is a technique that employs linearly changing potential at a set scan rate while current is being measured as a function of the potential.[57,58] Measurement equipment includes a potentiostat controlled by a computer to obtain a cyclic voltammogram that represents the redox behavior of the redox molecule obtained as a current as a function of the potential (**Fig 5**). The redox reaction was given in equation (i), and in **Fig 5,** the rising current represents the oxidation, and the peak with the returning negative current represents the reduction.

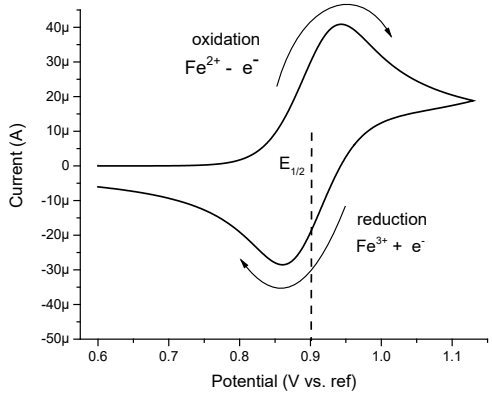

Figure 5. Schematic cyclic voltammogram with the redox reaction and peak separation marked.

Cyclic voltammetry is mostly measured with a three-electrode set-up. Below is a schematic picture (**Fig 6**) of the measurement cell. The potential of the working electrode (WE) is changed linearly in time at a set scan rate to have the redox reaction occur on the electrode surface. The potential of the working electrode is changed in reference to a reference electrode (RE), whose potential is known and stable. The current of the redox reaction is measured at the counter electrode (CE).

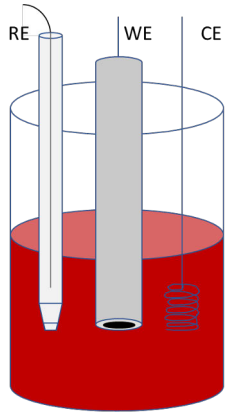

Figure 6. Schematic CV measuring cell on the left with RE as reference electrode, WE as working electrode, and CE as counter electrode.

The redox pair should be reversible in the CV studies, meaning that the returning current should not decrease during the CV cycle. If the returning current is decreased, the reason is most likely a chemical reaction that is using the charged species. This is known as an EC reaction[57], where E stands for Electrochemical and C for the following Chemical reaction. This behavior can lead to irreversible behavior if the returning current is clearly decreased.

Redox peak separation gives information on the number of electrons involved in the redox process; a 60 mV difference indicates a 1-electron redox process and 30 mV a 2-electron redox process. This is best illustrated by drawing the peak separation *vs.* the scan rate and taking the value from the intercept of that graph as the peak separation value. Further peak separation indicates a decreased electron transfer rate, hence giving information about the kinetics of the redox process. The scan rate and high ohmic resistance may affect this determination. Therefore, the number of electrons can be determined with CV simulations with the COMSOL Multiphysics model that is presented later.

More detailed analysis of the CVs can be obtained with the CV-related equations presented next and also via the mentioned finite element model (COMSOL), where diffusion coefficient, standard rate constant, charge transfer coefficient, number of the electrons, and chemical reaction rate of the EC reaction can be evaluated once the other required parameters are known.

2.3.1.1 Related equations

Butler-Volmer describes an electrochemical system when it is not in equilibrium, meaning when a potential or current is forced upon the studied system. This is, for example, in cyclic voltammetry measurements when a potential is applied to the

working electrode. The formula below is the derivation of Butler-Volmer[58] used in the COMSOL model simulations.

$$k_{\mathrm{ox}} = k^0 e^{\alpha n \frac{F}{RT}\left(E - E^{0'}\right)} \tag{1a}$$

$$k_{\mathrm{red}} = k^0 e^{(\alpha - 1) n \frac{F}{RT}\left(E - E^{0'}\right)} \tag{1b}$$

where, k_{red} and k_{ox} are the rate constants for reduction and oxidation reactions, k^0 is the standard rate constant, α charge transfer coefficient, n number of electrons, F is Faraday´s constant, R the gas constant, T temperature, E is the sweeping potential and $E^{0'}$ the formal potential (halfway potential is used instead of the formal potential in simulations).

Fick´s second law defines the diffusion equation, where the diffusion coefficient D_i is involved in providing the change in the concentrations over time.

$$\frac{\partial c_i}{\partial t} + \nabla(-D_i \nabla c_i) = \frac{\partial c_i}{\partial t} + \nabla(J_i) \tag{2a}$$

The flux with the oxidation and reduction rate constants and the concentrations of oxidized and reduced species is based on the diffusion equation accordingly:

$$J_{0,c_O} = k_{\mathrm{ox}} \cdot c_{\mathrm{R}} - k_{\mathrm{red}} \cdot c_{\mathrm{O}} \tag{2b}$$

Randles-Ševčík equation enables the study of the diffusion coefficient D, number of electrons n involved in the redox process or to calculate the theoretical peak current i_p with the D and n values. The equation is provided below.

$$i_p = 0.4463 * nFAC \left(\frac{nFvD}{RT}\right)^{1/2} \tag{3}$$

where, i_p is the maximum peak current [A], n number of electrons, A electrode area [cm^2], D diffusion coefficient [cm^2/s], C concentration [mol/cm^3], scan rate v [V/s], T temperature [K]. Constants are Faraday´s constant F [C/mol] and gas constant R [J/(K*mol)]

As the Randles-Ševčík equation is only applicable for reversible cases, it can also be used to obtain information on the reversibility of the redox process, as peak currents should be dependent on the square root of the scan rate and therefore their relation linear in a reversible case. Therefore, normalizing the currents with the

square root of the scan rate can give us information on the reversibility of the process and additional current sources, such as adsorption or side reactions. Some of these applications are in the results section, and the rest are found in the supplementary information (SI) parts of the attached publications.

Nernst equation describes the electrochemical redox reaction in equilibrium, meaning there is no current or potential forced upon the system. The Nernst equation relates the standard potential E^0 with the potential of the electrochemical cell E with the relative activities of the ox and red species. However, experimentally more usable is the formula presented below with concentrations and formal potential. This way we can obtain the concentrations of the redox active species in equilibrium by measuring the open circuit potential.

$$E = E^{0'} + \frac{RT}{nF} \ln\left(\frac{[c_{\mathrm{ox}}]}{[c_{\mathrm{red}}]}\right) \quad (4)$$

where E is the cell potential, $E^{0'}$ is the formal potential, $[c_{ox}]$ is the concentration of the oxidized species and $[c_{red}]$ is the concentration of the reduced species. Constants F is the Faraday´s constant [C/mol] and R is the gas constant [J/(K*mol)].

2.3.2 Flow battery operation

A flow battery consists of storage tanks and a minimum of one cell, as explained earlier. Its operation includes many parameters, which are discussed next, after which the equations related to the FB operation are discussed.

Charge and discharge of the FB can be done via constant current, constant voltage, or their combination, constant current and constant voltage. In constant current (CC), the current used to charge and discharge the battery is constant, until a certain voltage cut-off is reached. The same goes for constant voltage, which is applied until a certain amount of current remains. This way, the capacity utilization can be adjusted to stay on a set level, deepening the capacity utilization if need be. In the constant current and constant voltage (CCCV) operation, first, constant current is applied and then constant voltage to ensure deeper charge and discharge. This way we can see the stability of the redox active material in the ultimate state of charge. Additionally, in constant current operation, the state of charge reached at the cut-off is affected by the voltage cut-off. If the resistance of the cell changes during operation, *iR* drop changes, affecting the cell voltage. In constant voltage operation, current decreases towards the end of the step, and consequently, the same state of charge can be reached even when resistance and other conditions change.

Current densities for constant current step are chosen based on the concentration primarily, as 1 mA/cm^2 is chosen for 5 mM sample etc. Current density can be increased if side reactions are occurring, and their speed and effect on the capacity decay are studied. Theoretical capacitance is calculated based on concentration and volume before the battery studies to ensure we are not exceeding the theoretical capacity. If it is exceeded, we can get information on the number of electrons involved or another redox process at a similar potential. The flow rate of the electrolytes from the storage tanks to the cell can be adjusted, as the higher the flow rate, the faster the electrolyte moves to the cell, and this might be useful to adjust if charge/discharge is required to be performed fast. Analyzing the data obtained by adjusting these parameters can be done using, for example, the equations shown in the next section.

2.3.2.1 Related equations

Flow battery data can be analyzed with the following equations to obtain information about the operational parameters of the FB.[59]

Coulombic efficiency (CE) indicates the electron efficiency during charging and discharging. CE is calculated by dividing the electrons obtained from discharging the redox active material by the electrons used for charging the material. As CE is usually given in percentage, the value is then multiplied by 100 %. This is calculated with the electrically charged and discharged capacity per cycle.

$$CE = \int \frac{I_{\text{discharge}}}{I_{\text{charge}}} dt * 100\ \% = \frac{Q_{\text{discharge}}}{Q_{\text{charge}}} * 100\ \% \qquad (5)$$

CE is therefore a measure of how many electrons were lost in one cycle. Reasons for low CE can be a crossover of the charged species to the other side of the FB or side reactions where electrons can be lost. Crossover is not that common with iron complexes due to their rather large size compared to the membrane holes, whereas side reactions are more common with the studied iron(II) complexes, as described earlier. Sometimes, side reactions may not be well visible in CE during battery cycling if the side reactions are reversible.

Voltage efficiency (VE) indicates the differences in the voltage used to charge the battery and the voltage used to discharge the battery. In the ideal case, the voltages would be equal. However, resistance, slow kinetics of the redox reaction, and side

reactions can cause losses in voltage efficiency. Side reactions can create another redox active species, for example, a dimer, that can be discharged at a lower potential than the charging and discharging of the monomer; therefore, lowering the voltage efficiency of the battery. The equation for calculating voltage efficiency is presented below.

$$VE = \frac{V_{\text{discharge}}}{V_{\text{charge}}} * 100\ \% \tag{6}$$

VE and CE are both connected to the **energy efficiency** (EE). In the core, the energy efficiency gives the ratio of the energy received from the system *vs.* the energy given to the system. EE can be calculated as a division according to the previous sentence or as a multiplication of VE and CE. Both equations are presented below. As CE gives the electrical losses and VE the voltage losses, EE includes all the losses in FB, without the additional losses originating for example from pumps, which then need to be calculated separately if needed.

$$EE = \frac{E_{\text{discharged}}}{E_{\text{charged}}} = VE * CE \tag{7}$$

Capacity decay is the capacity lost during battery cycling and indicates the instability of the FB materials in the reported conditions. This parameter is affected by side reactions decreasing the amount of redox species, and by crossover, where redox-active species are lost through the membrane to the other storage tank. As mentioned earlier, the crossover is not a major concern in this thesis work: metal complexes are relatively large and the crossover of the organic negolyte species has a negligible effect on the battery performance due to adding it in excess compared to the metal complex side. Capacity decay is calculated as presented below. It can be calculated per cycle or by day; both equations are shown below.

$$Capacity\ decay = \frac{\Delta Q_{\text{discharge}}}{Q_{\text{initial discharge}} * N_{\text{cycles}}} * 100\ \% \tag{8}$$

$$Capacity\ decay\ (\%/day) = \frac{\Delta Q_{\text{discharge}}}{Q_{\text{initial discharge}} * t_{\text{cycles}}} * 24\ h * 100\ \% \tag{9}$$

Another flow battery parameter that needs to be discussed here is the **open circuit voltage** (OCV). OCV is defined as the voltage that the battery can deliver and, in an ideal case, is determined as the difference in the redox potentials of the negolyte and the posolyte. Therefore, the higher the posolyte redox potential is, and the lower the negolyte redox potential is, the higher the OCV is obtained.

2.3.3 Combination of flow battery and CV

In most cases, FB electrolytes are studied before and after flow batteries. Their behavior in the FB and the forming decomposition products are usually studied ex-situ by CV, EPR, NMR, UV-Vis, etc. Changing the sample environment from a nitrogen atmosphere in the glove box to a normal atmosphere (air, light, etc.) might provoke changes in the structure of these molecules. Therefore, the battery data and the obtained characterization results might not be consistent if the conditions are changed. Characterization techniques require the sample to stay the same as in the FB. Sealing the tube well and measuring fast can help avoid self-discharge and decomposition between the FB operation and the characterization. However, the most reliable measurements can be obtained in situ, and NMR and EPR techniques have been introduced to FB outlet hoses to enable this.[60,61] However, work on these characterization systems continues to obtain more flexible and cost-effective measurement systems. A limitation of NMR lies in analyzing paramagnetic species, while EPR is useful in analyzing paramagnetic species. Both are also rather expensive techniques.[62,63] When considering the analysis of Fe(II) complexes during FB operation, Fe(III) is paramagnetic whereas Fe(II) is not.[36] Therefore, it is not useful to utilize these characterization techniques when studying iron complex FB electrolytes. UV-Vis, on the other hand, has a problem with the detection limit, specifically when a second-order decomposition reaction such as dimerization is involved.

Only a few in situ tools are available for FB electrolyte characterization.[63–65] SOC is monitored via OCP measurement or with conductivity measurement for vanadium flow batteries,[64] however, this does not provide information on the decomposition reactions. Cross-over through the membrane has been studied via CV,[65] while most of the time CV is used before and after FB operation to characterize the FB materials and electrodes.[59,62,63] Microelectrodes have been used in situ for state of charge and state of health analysis of FB electrolytes.[66–68] However, these are rather expensive and break easily. For lithium-ion batteries, it is possible to determine and even forecast the state of the health of a lithium-ion battery, as well as determine device degradation in real-time.[69,70] Flow batteries are a new field, and no conventional methods of studying FB electrolytes in situ exist. Thus, cost-

effective measurement set-ups are needed to reach the state of health and charge analysis for FB electrolytes during FB operation.

Cyclic voltammetry is useful in determining redox activity,[57] even in mixtures of redox-active species. In addition, kinetic parameters can be derived from the cyclic voltammograms. CV is used to analyze the FB electrolytes, mostly before the lab-scale FB studies, to see whether the cyclic voltammogram indicates reversible redox behavior. However, reversibility in the time-scale of CV measurements indicates that no severe decomposition happens in that time due to the low effective concentration at the WE surface. This makes detecting redox-active side reaction products in a CV measurement unlikely, as the salt concentration and the non-transformed species concentration affect the formation of side products via chemical reactions. When a CV is run in an FB storage tank, where the effective concentration is higher due to electrogenerating the charged species, the side reaction products can be seen via CV measurement, and this information can be compared to the battery data.

By combining FB with CV electrode set-up on the storage tanks, information on the structural changes and changes in the redox active species could be obtained in real-time in a cost-effective and simple manner. This would be especially useful for the metal complexes studied in this thesis, since their electrochemical and chemical reactions are complex. Hence, further understanding of the changes during FB operation is needed. By integrating the 3-electrode set-up into the electrolyte reservoirs in the FB, we could obtain additional information on the concentration differences in the storage tanks of each species and about the decomposition and self-discharge in real-time. Concentrations could be used to obtain the state of charge (SOC) via OCP of the half-cells and simulations of the peak currents in CVs. Both storage tanks could be characterized individually from each other. Below is a schematic figure (**Fig 7**) of this kind of measurement set-up.

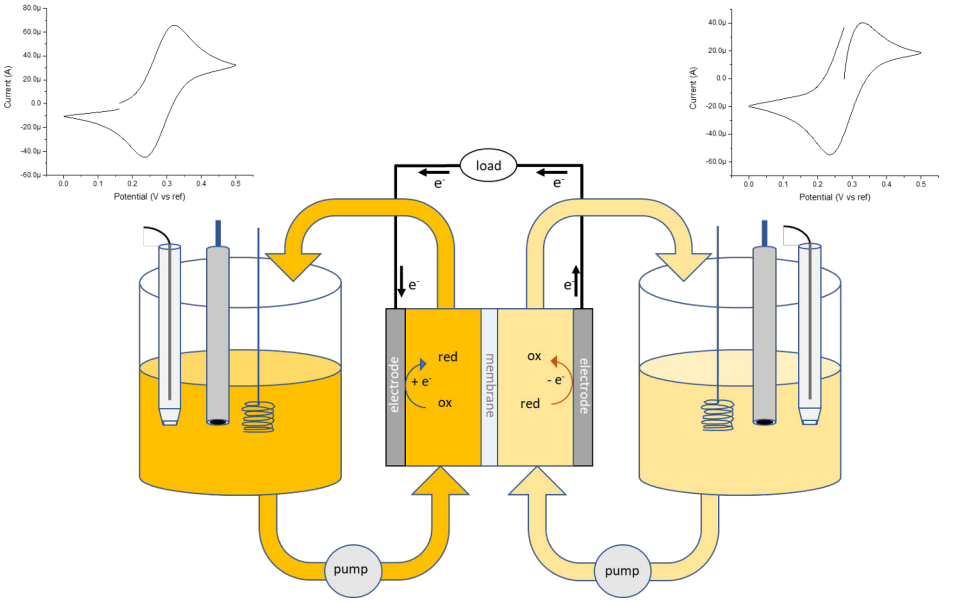

Figure 7. Schematic measurement set-up of the cyclic voltammetry and FB operation combined.[v]

2.3.3.1 Related equations

By using the **Nernst equation**, concentrations of the redox species in storage tanks based on the **open cell potential** (OCP) can be calculated during flow battery operation.

$$E = E^{0'} + \frac{RT}{nF} \ln\left(\frac{c_{\text{ox}}}{c_{\text{red}}}\right) \tag{10a}$$

$$c_{\text{ratio}} = \frac{C_{ox}}{c_{red}} = exp\left(\frac{nF}{RT} * (E_i - E^0)\right) \tag{10b}$$

$$c_{\text{red}} = c_{total} - c_{\text{ox}} \tag{11}$$

$$c_{\text{ox}} = \frac{c_{\text{ratio}}}{1 + c_{\text{ratio}}} * c_{total} \tag{12}$$

To calculate the **state of charge** SOC for storage tanks, we need to know the concentrations. We can calculate those from the OCP as in the equations above. The equation for calculating SOC is presented below first for posolyte, then to negolyte.

$$SOC = \frac{C_{\text{ox}}}{C_{\text{total}}} * 100\ \% \tag{13}$$

$$SOC = \frac{C_{\text{red}}}{C_{\text{total}}} * 100\ \% \tag{14}$$

2.3.4 Structural characterization

All the synthesis products were characterized with NMR as the complexes were in iron(II) form. However, this is not a practical technique for iron complexes after or during operation due to the presence of water and the paramagnetic nature of Fe(III), as explained earlier. Therefore, other characterization methods were utilized during battery cycling. Mostly, the characterization was performed via CV measurements, but also structural characterization techniques were also utilized. The most important of these was UV-Vis, as we can obtain information on the structure in solution even at low concentrations.

2.3.4.1 Spectroscopical techniques

2.3.4.1.1 UV-Vis

UV-Vis (UltraViolet-Visible) spectroscopy measures the absorbance or transmission of the measured sample at the ultraviolet and visible light wavelengths. The used wavelengths need to excite electrons to transition between energy levels so that the molecule can absorb light at that wavelength. The energy pulse needs to correspond to a transition in the structure. Oxidation states and conjugation in the structures are common sources of absorbance. Changes in these lead to differences in absorbance spectra.

The sample is measured against a known reference, whose UV-Vis spectra are measured first to account for its response. Absorbance maxima and absorbance peaks, as well as changes in their position and intensity, indicate changes in the structure corresponding to those wavelengths. Usually, the literature has a good library of compound spectra that can be used to compare the transitions in the experimental data.

Lambert-Beer law needs to be addressed when talking about absorbance, and its equation is given below. Once a calibration curve with known concentration samples has been obtained, it can be used to determine concentrations in sample solutions. Therefore, UV-Vis can also be a quantitative tool to determine the maximum solubilities of compounds.

$$A = l * c * \varepsilon \tag{15}$$

where A is the absorbance (no unit), l is the optical path length (cm), the concentration of the absorbing species (mol/dm^3) and ε is the molar absorptivity of the studied species (dm^3/mol/cm).

3 Materials and Methods

3.1 Materials

Material selection in **publication I** was $[Fe(II)(bpy)_3]^{2+}$ complexes synthesized in the University of Jyväskylä. Used functional groups for $[Fe(II)(bpy)_3]^{2+}$ complexes were 4,4′-positioned: methyl (Me), methoxy (MeO), *tert*-butyl (*t*Bu), methylcarboxylate (CO_2Me), carboxylic acid (c) and bromo (Br). Counterions were sulfate (SO_4^{2-}) and tetrafluoroborate (BF_4^-). Complexes will be referred to as $[Fe(II)(DR\text{-}bpy)_3]^{2+}$, where DR means **d**i-4,4′-placed functional groups **R**. Negolyte (NDI, naphthalene-diimide) was synthesized[71] in the University of Turku. Detailed synthesis is reported in the **publication I** with the NMR characterization.

In **publication II**, Fe(II) complexes with phen and terpy ligands were studied. Functional groups for $[Fe(II)(phen)_3]^{2+}$ complexes were 4,7-dimethyl, 3,4,7,8-tetramethyl and 4,7-dichloro. For $[Fe(II)(terpy)_2]^{2+}$ complexes the studied functional groups were 4'-carboxylic acid, 4,4',4''-tricarboxylic acid, 4'-chloro and 4'-(4'''-pyridyl). Counterions for Fe(II) complexes with phen and terpy ligands were chlorides. Detailed synthesis is reported in **publication II** with the characterization. The utilized negolyte AZON3 (azoniafluorenone, 5-oxo-2-(3-(trimethylammonio)propyl)-5H-indeno[1,2-c]pyridin-2-ium bromide) was obtained[72] from the University of Jyväskylä.

Titanium(IV) complex with 2,3-dihydroxynaphthalene ligands ($[Ti(IV)(ncat)_3]^{2-}$) was synthesized as reported in **publication III** with NMR characterization.

$[Fe(II)(bpy)_3]^{2+}$ for **publication V** was synthesized similarly to the one in **publication I**, but with chloride counter ions. Characterization was performed with NMR. Commercial $K_3[Fe(III)(CN)_6]$ and $K_4[Fe(II)(CN)_6]$ were purchased from VWR.

$[Fe(II)(bpy)(CN)_4]^{2-}$ was purchased from HetCat company as a commercial compound.

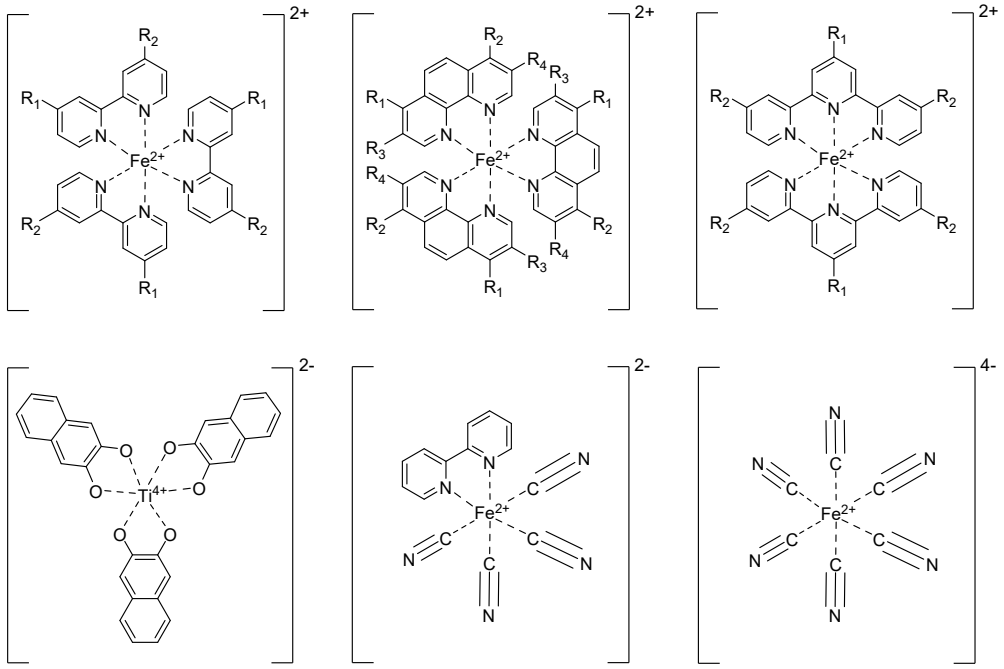

Figure 8. Studied metal complexes starting from top left: $[Fe(II)(bpy)_3]^{2+}$, $[Fe(II)(phen)_3]^{2+}$, $[Fe(II)(terpy)_2]^{2+}$, $[Ti(IV)(ncat)_3]^{2-}$, $[Fe(II)(bpy)(CN)_4]^{2-}$, $[Fe(II)(CN)_6]^{4-}$.

3.2 Characterization of FB materials

3.2.1 Cyclic voltammetry

The materials used in CV measurements were glassy carbon as WE (3 mm diameter, BASi), Ag/AgCl in 3 M KCl as RE (BASi), and spiraled platinum wire to ensure the area of the CE is larger than the area of WE. Electrodes were cleaned with water and ethanol and occasionally with the corresponding solvents for each solution. WE was polished with alumina paste of different sizes (1 µm, 0.3 µm, and 0.05 µm diameter) and rinsed with reverse-osmosis water. Potentiostats of Gamry Reference 600+, Biologic Potentiostat SP-240, and PalmSens4 (software PSTrace 5.8) were utilized during thesis work.

3.2.2 Simulations

Simulations of the CVs were performed with COMSOL Multiphysics software using a finite element model. The model contains 2 “Transport of Diluted species” (Physics). One of these simulates the oxidation of the reduced species on the electrode, and the other one simulates the reduction of the oxidized species on the

electrode and the chemical reaction consuming the oxidized species. The triangle and interpolation functions were used to utilize the sweep potential, considering the ohmic losses. Only diffusion is considered, flux is taken according to Fick´s second law, the rate constants depend on the potential according to the Butler-Volmer equation and chemical reaction rates are implemented as basic 1st and 2nd order reactions. The models are in detail in the SIs of **publications I**, **II**, **IV**, and **V**.

The fitting of the simulated CV to the experimental was performed by fitting the following parameters. First k^0 was fit to obtain the correct peak placement, where the higher k^0 value brings the peaks closer to one another in potential and a lower value correspondingly distances the peaks further from one another. D was utilized to fit the simulated oxidation current to the experimental peak current, where a higher value brings more species to the WE surface and therefore raises the current. Finally, k_c value was utilized to fit the experimental and simulated reduction peaks, where higher k_c value reduces the reduction current from reversible redox reactions. The effect of these parameters on the cyclic voltammogram is illustrated in **Fig 9**.

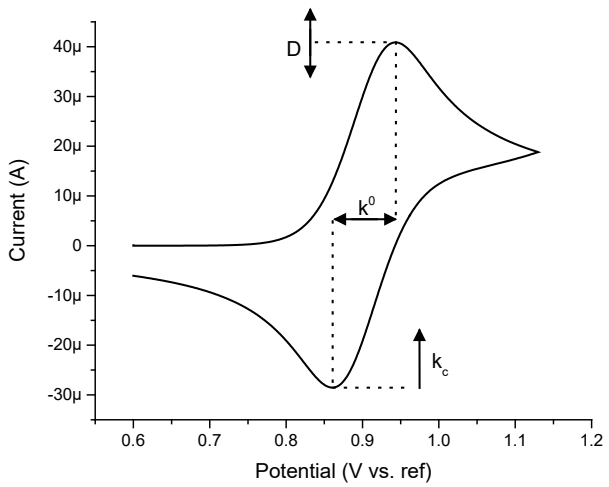

Figure 9. Effects of the fitting parameters on the shape of the cyclic voltammogram.

3.2.3 Flow battery tests

Lab-scale flow battery tests were performed with a battery cycler LANHE Battery Testing System G340A. Flow battery set-up (**Fig 10**) consisted (when moving from outer to inner layers) of endplates (PVC), o-rings to seal the electrolyte flow to the cell, current collectors/bipolar plates (fabricated from carbon composite plates from Pinflow ES, Czech Republic), carbon felt electrodes (thickness 4.6 mm, thermally

activated, SGL GFD 4.65) in expanded Teflon gaskets (thickness 3 mm, expanded PTFE, cut from 24SH-ePTFE gasket sheets from TEADIT, Switzerland) and a membrane (anion exchange membrane Selemion DSVN for positively charged compounds and cation exchange membrane Nafion 117 for negatively charged compounds). The area of the cell was 5 cm^2. Flow battery set-up was located in a glovebox with a nitrogen atmosphere. Cycling conditions included CC, in which the charge/discharge was performed with constant current until a set voltage was reached, and CCCV, where the constant current was utilized as mentioned after which the charging/discharging was performed with constant voltage until a set current was reached, to obtain a more thorough charge and discharge of the molecules.

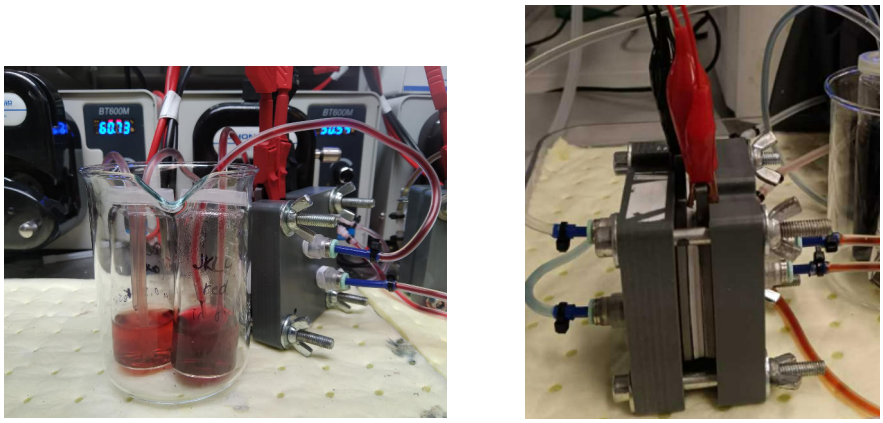

Figure 10. Experimental lab-scale flow battery set-up. On the left, the storage vials are on the front and the battery cell with the connections can be seen behind the storage vials. The pump is located behind the battery cell. In the picture on the right, we can see the cell assembly from the side. From the outer parts to the inner parts: the endplates have tube connections to storage vials sealed with o-rings, graphite current collectors touching the carbon felt electrodes located inside the white Teflon gaskets, and a membrane. Connections to the battery cycler are with the crocodiles connected to carbon plates.

3.2.4 Combined battery and CV measurement set-up

Two lab-scale flow batteries were assembled as described earlier, one for a symmetric battery of hexacyanoferrate and one for an asymmetric battery of $[Fe(II)(bpy)_3]^{2+}$ *vs.* azoniafluorenone. Concentrations for hexacyanoferrates and $[Fe(II)(bpy)_3]^{2+}$ were 5 mM and for the azoniafluorenone 10 mM. The electrolyte was 0.1 M NaCl and pH was adjusted to be above 7 for stability reasons of hexacyanoferrates and the azoniafluorenone. Material selection was chosen based on hexacyanoferrate stability and a simple redox process,[50,73] and $[Fe(II)(bpy)_3]^{2+}$ for

the double-discharge plateaus and known dimerization process during battery operation.[52,56]

The study was performed by running CVs and measuring OCP from the storage tanks individually during battery cycling. The electrodes were 3- and 2-mm glassy carbon working electrodes (BASi), leakless Ag/AgCl reference electrodes (ET072 electrode from eDAQ) provided by Pinflow, and Pt wire as counter electrodes. For the asymmetric battery, only the $[Fe(II)(bpy)_3]^{2+}$ side was monitored, while for the symmetric hexacyanoferrate battery, both storage tanks were monitored. The idea in this was to obtain information on the states of charge, side reactions, decomposition, and self-discharge during battery operation. Hexacyanoferrate battery was run outside the glovebox, while $[Fe(II)(bpy)_3]^{2+}$ *vs.* azoniafluorenone was run inside the glovebox, and CVs were run outside and inside the glovebox, respectively, starting from the OCP.

The OCP values and CV peak current values were utilized to obtain information on the concentrations via the Nernst equation. Simulations of the CVs of hexacyanoferrates were done to obtain information on the concentrations during battery cycling via peak currents of the CV. Peaks in the CVs were assigned and their responses were monitored during battery cycling for hexacyanoferrates and $[Fe(II)(bpy)_3]^{2+}$, obtaining information on the redox activity of the species during charging and discharging in a lab-scale FB.

This set-up was additionally utilized for obtaining information on the charged states of $[Fe(II)(phen)_3]^{2+}$ and $[Fe(II)(terpy)_2]^{2+}$.

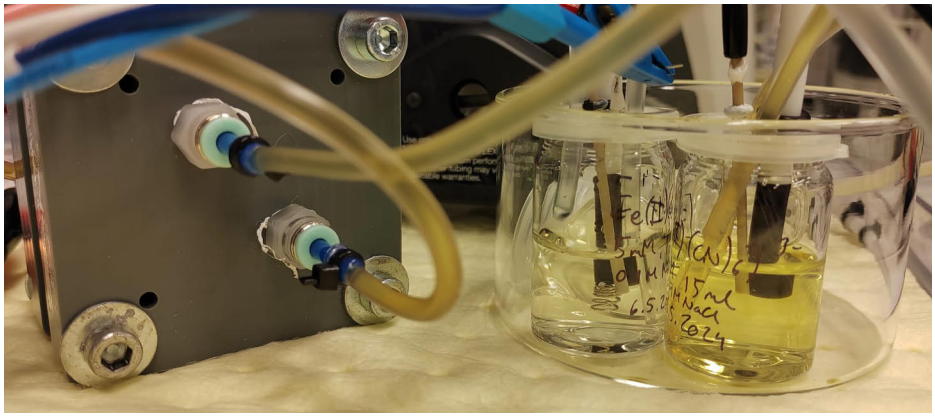

Figure 11. Experimental lab-scale flow battery set-up with a 3-electrode set-up on electrolyte tanks to enable the cyclic voltammetry measurements.[v]

3.2.5 Spectroscopical methods

UV-Vis samples of $[Fe(II)(bpy)_3]^{2+}$, $[Fe(II)(phen)_3]^{2+}$ and $[Fe(II)(terpy)_2]^{2+}$ at different stages of battery cycling were measured with Specord 200 plus (analytik jena) spectrophotometer *vs.* 0.1 M NaCl reference, which was the used supporting electrolyte in the battery studies. Information on the structural changes in the compounds was obtained before cycling, at charged state(s) and discharged state(s) of the posolytes.

4 Redox potentials and CV analysis

Several synthesized Fe(II) complexes with bpy, phen, and terpy ligands with various functional groups (Me, *t*Bu, COOH, OMe, COOMe, Cl, Br, 4-py), commercial $[Fe(II)(bpy)(CN)_4]^{2-}$ and $[Ti(IV)(ncat)_3]^{2-}$ were measured via cyclic voltammetry to obtain information about redox potentials and the effect of the functional groups on the redox potentials. CV analysis was performed with the Randles-Ševčík equation for Fe(II) complexes with phen and terpy ligands and the adsorption of these compounds on a glassy carbon working electrode was studied.

4.1 Redox potentials

The obtained redox potentials are listed in **Table 1**, where values from the literature and computational values from **publication III** are also compared. Most of the found literature values are reported in organic solvents, but we were interested in the redox potentials of the compounds in aqueous solvents, therefore, only those values and corresponding literature references are given.

Table 1. Redox potentials of the studied metal complexes in aqueous solutions. Values are combined from **publications I, II and III**, and the value of $[Fe(II)(bpy)(CN)_4]^{2-}$ is unpublished.

Compound	Experimental $E^{0'}$ [V *vs.* SHE]	$E^{0'}$ in literature [V *vs.* SHE]	$E^{0'}$ computational [V *vs.* SHE]
$[Fe(II)(bpy)_3]^{2+}$	1.080	1.030 [52]	1.122
$[Fe(II)(DMe\text{-}bpy)_3]^{2+}$	0.910		0.923
$[Fe(II)(Dt\text{Bu}\text{-}bpy)_3]^{2+}$	0.930		1.15
$[Fe(II)(D(OMe)\text{-}bpy)_3]^{2+}$	0.765		0.779
$[Fe(II)(D(CO_2Me)\text{-}bpy)_3]^{2+}$	-0.745; 0.016; ca. 1.5 V		1.475
$Na_{4+x}[Fe(II)(Dcbpy)_3](BF_4)_x$	1.175	1.30 [52] 1.15 [48]	1.518 (protonated)

Compound	Experimental $E^{0'}$ [V *vs.* SHE]	$E^{0'}$ in literature [V *vs.* SHE]	$E^{0'}$ computational [V *vs.* SHE]
$[Fe(II)(bpy)(CN)_4]^{2-}$	0.57		
$[Fe(II)(phen)_3]^{2+}$	1.115	1.06 [47]	1.178
$[Fe(II)(DMe\text{-}phen)_3]^{2+}$	0.920	0.93 [47]	0.944
$[Fe(II)(TMe\text{-}phen)_3]^{2+}$	0.879		0.884
$[Fe(II)(DCl\text{-}phen)_3]^{2+}$	1.290		1.37
$[Fe(II)(terpy)_2]^{2+}$	1.130	1.06 [47]	1.027
$[Fe(II)(COOH\text{-}terpy)_2]^{2+}$	1.173		1.20 (protonated)
$[Fe(II)(3COOH\text{-}terpy)_2]^{2+}$	1.245		1.51 (protonated)
$[Fe(II)(Cl\text{-}terpy)_2]^{2+}$	1.191		1.37
$[Fe(II)(4py\text{-}terpy)_2]^{2+}$	1.185		1.12
$[Ti(IV)(ncat)_3]^{2-}$	–1.175		–1.61

All of the studied iron(II) compounds in **Table 1** show sufficient redox potentials for usage as posolytes in flow battery applications. Titanium(IV) complex with naphthacatechol ligands shows a sufficient redox potential for a negolyte in flow battery applications. Since it was not stable in aqueous solution, it was not further tested nor were cyclic voltammograms analyzed. Some of the obtained posolyte redox potentials can be at too high potentials considering the oxygen evolution reaction OER. pH of these solutions shifts the potential window of water, so in mildly acidic solutions, the redox potentials would still be below the OER (0.82 V *vs.* SHE in neutral conditions) on the carbon electrode. Regardless of the rather low thermodynamic potential value when compared to the obtained posolyte redox potentials, the stability window is at more positive potential values in practice due to the sluggish kinetics of the OER.

The functional group effect is clear; the EDGs shift the redox potential to more negative values, as the EWGs have the opposite effect. The functional groups change the electron density near the iron center accordingly and affect the redox potential of the compound. Some of the redox potentials of the complexes in the literature correspond to the experimental values rather well. The computational redox potential values fit in general well for the iron complexes, even though the complexes with COOH functional groups seem to have a small deviation between the experimental

and computational values. The redox potential of $[Ti(IV)(ncat)_3]^{2-}$ differs from the computational redox potential value, but the difficulty of computationally obtaining redox potentials of similar complexes has been discovered earlier also.[74]

4.2 CV analysis

4.2.1 Additional peaks in CVs

Most of the compounds showed one redox pair for the metal complex redox reaction. However, some of the studied compounds in **publication II**, $[Fe(II)(DCl\text{-}phen)_3]^{2+}$, $[Fe(II)(Cl\text{-}terpy)_2]^{2+}$, and $[Fe(II)(4py\text{-}terpy)_2]^{2+}$, showed an extra oxidation peak overlapping the oxidation of the iron redox pair as well as an additional reduction peak at lower potentials that was related to additional oxidation current at redox pair oxidation peak potential. Below in **Fig 12** is the CV of one of these compounds, $[Fe(II)(DCl\text{-}phen)_3]^{2+}$, where we can see the relation of the additional oxidation and the additional reduction peaks and the independence of the redox pair from them. We do not have an explanation for this behaviour, nor did we study it further. However, it seems that since the additional oxidation and reduction are related to each other, we could have one redox pair with a large peak separation, which could indicate a larger molecule formation with slow kinetics. Another explanation is that they are a ligand oxidation and a dimerization reduction process.

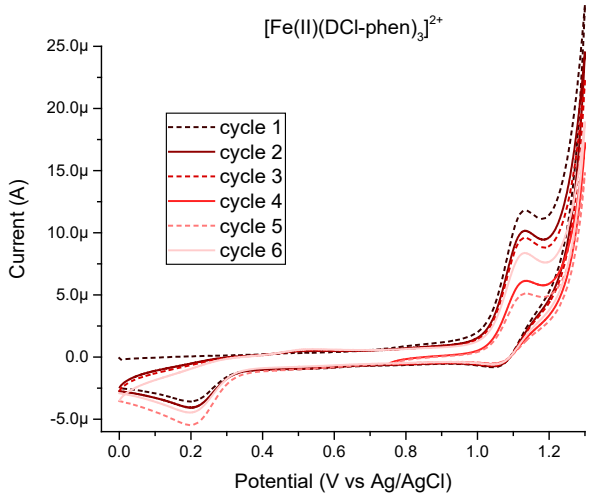

Figure 12. CV of $[Fe(II)(DCl\text{-}phen)_3]^{2+}$. WE 3 mm glassy carbon, scan rate 100 mV/s. Concentration 1 mM in 0.1 M NaCl.[II]

$[Fe(II)(D(CO_2Me)\text{-}bpy)_3]^{2+}$ showed redox pairs at potentials -0.745 and 0.016 V *vs.* SHE, as seen in **Fig 13** below, whereas it seems that the oxidation of the redox pair is irreversible and located at ca. 1.5 V *vs.* SHE. Computational studies in **publication III** confirmed that the redox pair is the one located at ca. 1.5 V *vs.* SHE, the computational value being 1.475 V *vs.* SHE. The response at -0.745 V *vs.* SHE likely originates from iron deposition, whereas the redox pair at 0.016 V *vs.* SHE remains unknown, however, it may be a decomposition product of the irreversible oxidation of the iron complex.

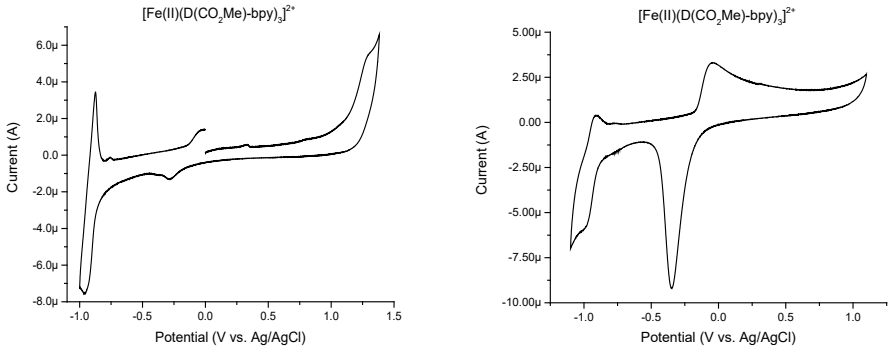

Figure 13. $[Fe(II)(D(CO_2Me)\text{-}bpy)_3]^{2+}$ (0.5 mM) in phosphate buffer (0.1 M, pH 7). Iron redox pair is expected to originate from an irreversible oxidation peak at 1.3 V *vs.* Ag/AgCl. Scan rate is 100 mV/s.[III]

4.2.2 Adsorption

$[Fe(II)(phen)_3]^{2+}$, $[Fe(II)(DMe\text{-}phen)_3]^{2+}$, and $[Fe(II)(terpy)_2]^{2+}$ were studied in different concentrations (1, 2.5, and 5 mM) and with several scan rates within one concentration, to detect changes in the redox peak currents in **publication II**. The current was normalized with the concentration to compare the different concentration samples with each other within the same scan rate. The currents were also compared within a sample concentration, hence, the cyclic voltammograms were normalized by the square root of the scan rate. Cyclic voltammograms were recorded at several scan rates to be able to see the difference between the diffusion-controlled system and the system with a mixed mechanism (diffusion and adsorption) in between the concentrations.

The adsorption on the glassy carbon working electrode occurs to the oxidizing species, while the phenomenon is not significant to the reduced species of the studied compounds. We can state that the adsorption is weak for the oxidized species, similar to certain ferrocene derivatives.[75] It has been established that for these ferrocene derivatives, the oxidation process in the cyclic voltammogram is diffusion-controlled

as corresponding to the Randles-Ševčík equation. When the scan rate was increased, the oxidation peak current increased significantly more compared to the reduction peak current with a 1 mM sample concentration. With a 5 mM sample, the changing scan rate demonstrated the marginal contribution of the adsorption to the studied oxidation current. This can be seen in **Fig 14**.

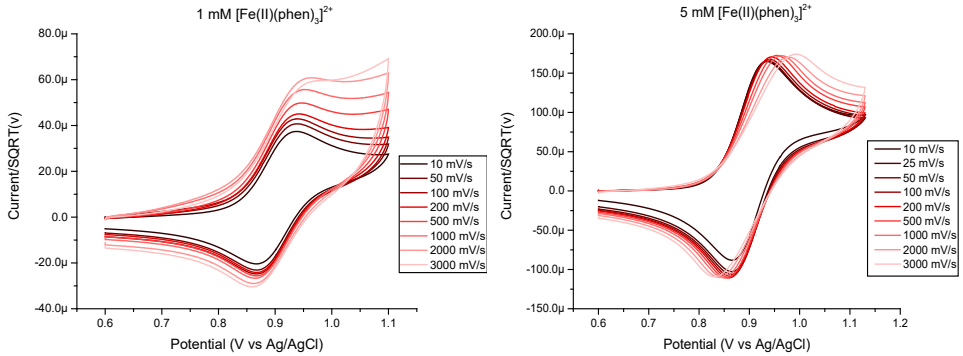

Figure 14. Cyclic voltammograms of $[Fe(II)(phen)_3]^{2+}$ with concentrations of 1 and 5 mM were recorded with several scan rates. The current was normalized with the square root of the scan rate.[II]

Comparing solutions of different concentrations of the studied Fe(II) complexes is another way to prove the mixed mechanism of adsorption and diffusion-controlled behavior.[76] This is demonstrated in **Fig 15**, where the oxidation peak current increases with the decrease in concentration, while the reduction current remains at similar values regardless of the change in the concentration. Increasing the concentration frees the redox process from the effect of adsorption on the current, and therefore allows examination of the favored diffusion-controlled system. Decreasing the concentration leads to a mixed mechanism of adsorption and diffusion control. The reason for this behavior is that the higher concentration leads to an almost saturated WE surface; therefore, the adsorption of the oxidizing species is constant and negligible.[76]

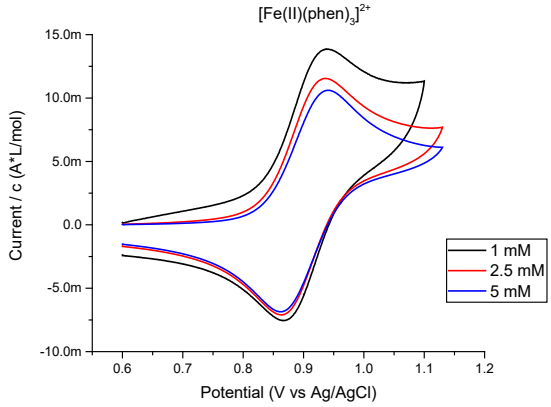

Figure 15. CVs of $[Fe(II)(phen)_3]^{2+}$ in different concentrations demonstrate the adsorption of the oxidized species. Scan rate 100 mV/s, WE glassy carbon 3 mm, electrolyte 0.1 M NaCl, currents divided by the concentration.[II]

While only the graphs related to $[Fe(II)(phen)_3]^{2+}$ are shown here, $[Fe(II)(terpy)_2]^{2+}$ and $[Fe(II)(DMe\text{-}phen)_3]^{2+}$ behaved similarly, regardless of slightly smaller reduction currents detected at decreased scan rates for $[Fe(II)(terpy)_2]^{2+}$. All the graphs are available in the Supplementary Information of **publication II**. Analysis of these compounds with this evidence was continued with a 5 mM sample concentration.

5 Simulations

COMSOL Multiphysics Software was utilized to measure the diffusion coefficient D, the standard rate constant k^0 and the chemical reaction rate k_c for the chemical reaction that follows the electron transfer. We were able to evaluate the electrochemical kinetics and the stability of the $[Fe(II)(bpy)_3]^{2+}$ complexes with different counterions in **publication I**. For Fe(II) complexes with phen and terpy ligands, we were able to get diffusion coefficients out reliably from the simulations in **publication II**; however, the standard rate constants k^0 and the rates for the chemical reaction k_c were open to deviation. Next, we are going through the results first and then assessing the sensitivity of the model per the obtained parameter.

5.1 $[Fe(II)(bpy)_3]^{2+}$ derivatives

Computational CVs were fitted to the experimental CVs of various $[Fe(II)(bpy)_3]^{2+}$ complexes, obtaining information about the kinetics and diffusion of the iron redox pair in **publication I**. Experimental CVs were measured in different aqueous electrolytes with several scan rates. Resistances and real concentrations were considered in the simulations.

The first part of the results, **Table 2**, showed that the BF_4^- should be avoided as a counter ion during the synthesis of these compounds. The $[Fe(II)(bpy)_3]^{2+}$ complexes showed higher chemical reaction rates for the complexes having BF_4^- instead of SO_4^{2-} as a counterion. This was an interesting observation, especially because the counterion concentration is very small compared to the supporting electrolyte concentration. A possible explanation is found in the literature, where the BF_4^- hydrolyses when in contact with water and reacts with the nitrogens in the bipyridines, forming $bpy(BF_3)_2$ and therefore affecting the decomplexation rate.[55,77] Available BF_4^- ions from the $NaBF_4$ salt shown by ^{19}F NMR are most likely the reason for the instability of our $Na_{4+x}[Fe(II)(Dcbpy)_3](BF_4)_x$ when compared to the same complex reported in the literature by Li *et al*,[48] for which we did not detect a chemical reaction rate upon simulations.

Table 2. Obtained values from simulations of $[Fe(II)(bpy)_3]^{2+}$ complexes with different counterions in phosphate buffer (pH 7, 100 mM). Relative standard deviations are in brackets after each value.[I] Experimental and simulated CVs, parameters per scan rate, and standard deviations are in SI in **publication I**.

Complex and counterion	$D \times 10^6$ [cm²/s]	$k^0 \times 10^2$ [cm/s]	α	k_c [1/s]
$[Fe(II)(bpy)_3]SO_4$	1.90 (16.5 %)	1.13 (61.7 %)	0.5	0.017 (7.1 %)
$[Fe(II)(bpy)_3](BF_4)_2$	1.89 (5.8 %)	3.16 (84.6 %)	0.5	0.045 (18.6 %)
$[Fe(II)(DMe\text{-}bpy)_3]SO_4$	0.85 (3.7 %)	1.18 (50.3 %)	0.5	0.009 (5.3 %)
$[Fe(II)(DMe\text{-}bpy)_3](BF_4)_2$	2.32 (6.7 %)	1.28 (45.8 %)	0.5	0.020 (48.8 %)
$[Fe(II)(D\textit{t}Bu\text{-}bpy)_3]SO_4$	1.28 (8.2 %)	1.05 (54.0 %)	0.5	0.016 (56.0 %)
$[Fe(II)(D\textit{t}Bu\text{-}bpy)_3](BF_4)_2$	0.39 (12.9 %)	0.35 (40.2 %)	0.5	0.059 (53.5 %)
$[Fe(II)(D(OMe)\text{-}bpy)_3]SO_4$	0.66 (7.8 %)	1.12 (37.2 %)	0.5	0.075 (21.3 %)
$[Fe(II)(D(OMe)\text{-}bpy)_3](BF_4)_2$	0.12 (6.0 %)	0.49 (42.0 %)	0.5	0.048 (16.3 %)
$Na_{4+x}[Fe(II)(Dcbpy)_3](BF_4)_x$	0.38 (7.9 %)	0.05 (0 %)	0.3	0.158 (62.7 %)
$Na_{4+x}[Fe(II)(Dcbpy)_3](BF_4)_x$*	0.59 (2.9 %)	0.44 (25.0 %)	0.5	0.015 (66.1 %)
$Na_4[Fe(II)(Dcbpy)_3]$ ** **ref** [48]	2.30	0.40	0.5	0.000

*In phthalate buffer.
**Data from ref [48].

The iron complexes with sulfate counterions were further tested in different electrolytes, **Table 3**. Change of electrolyte had a positive effect on the diffusion coefficients of the studied metal complexes, increasing them greatly when compared to D values obtained in phosphate buffer. Along with D, k^0 values improve within iron complexes by obtaining higher values than in phosphate buffer, in some cases even quadrupling. This might originate from the effect of anions in the solution on the electron transfer, by not ruling out the cation effect as it can influence too.[78] k_c value was also improved by choosing another electrolyte than phosphate buffer.

Table 3. Obtained values from simulations of $[Fe(II)(bpy)_3]^{2+}$ complexes in different electrolytes.[I] Experimental and simulated CVs, parameters per scan rate, and standard deviations are in the SI of **publication I**.

Complex and electrolyte	$D \times 10^6$ [cm²/s]	$k^0 \times 10^2$ [cm/s]	α	k_c [1/s]
$[Fe(II)(bpy)_3]SO_4$				
0.1 M phosphate buffer pH 7	1.90 (16.5 %)	1.13 (61.7 %)	0.5	0.017 (7.1 %)
0.1 M KNO_3	3.03 (2.2 %)	2.51 (63.1 %)	0.5	0.006 (61.2 %)
0.1 M K_2SO_4	2.73 (2.8 %)	2.02 (53.5 %)	0.5	0.010 (8.8 %)
0.1 M NaCl	2.89 (0.6 %)	2.26 (44.9 %)	0.5	0.003 (14.3 %)
$[Fe(II)(DMe\text{-}bpy)_3]SO_4$				
0.1 M phosphate buffer pH 7	0.85 (3.7 %)	1.18 (50.2 %)	0.5	0.009 (5.3 %)
0.1 M KNO_3	1.7 (1.6 %)	2.12 (61.0 %)	0.5	0.003 (20.5 %)
0.1 M K_2SO_4	1.32 (2.4 %)	1.97 (52.5 %)	0.5	0.002 (99.1 %)
0.1 M NaCl	1.35 (2.5 %)	2.46 (63.5 %)	0.5	0.002 (83.6 %)
$[Fe(II)(D\textit{t}Bu\text{-}bpy)_3]SO_4$				
0.1 M phosphate buffer pH 7	1.28 (8.2 %)	1.05 (54.0 %)	0.5	0.016 (56.0 %)
0.1 M KNO_3	n/a	n/a	n/a	n/a
0.1 M K_2SO_4	1.92 (2.6 %)	1.44 (42.6 %)	0.5	0.014 (55.7 %)
0.1 M NaCl	1.82 (3.4 %)	2.69 (63.8 %)	0.5	0.009 (77.2 %)
$[Fe(II)(D(OMe)\text{-}bpy)_3]SO_4$				
0.1 M phosphate buffer pH 7	0.66 (7.8 %)	1.12 (37.2 %)	0.5	0.075 (21.3 %)
0.1 M KNO_3	1.77 (10.8 %)	1.67 (40.9 %)	0.5	0.024 (36.1 %)
0.1 M K_2SO_4	1.42 (2.3 %)	4.08 (54.2 %)	0.5	0.028 (28.2 %)
0.1 M NaCl	1.68 (4.9 %)	3.97 (56.2 %)	0.5	0.030 (31.9 %)

In general, the diffusion coefficients correspond to the literature values (D for $[Fe(II)(bpy)_3]SO_4$ reported to be 1.6-2.1x10^{-6} cm²/s in 1 M 2-propanol and 1 M NaCl),[79] when we consider the counterion effect; some of the WE area can be blocked due to decomposition products, or the counterion affects the diffusion via ion pair formation. The D values corresponded rather well with the size of the compound; smaller compounds are expected to exhibit higher D. In addition, higher D value seems to correlate with lower k_c value. This could be originating from detached ligands blocking the WE surface area, leading to a misleading decrease in the D values, as well as k_c values.

The lowest k_c value was obtained for $[Fe(II)(DMe\text{-}bpy)_3]^{2+}$, leading to a conclusion that the electron-donating nature of the methyl groups might be decreasing the rate of the decomposition of the Fe(III) species. Electron-donating nature of the methyl groups could hinder the ligand breaking off when the Fe center radius gets smaller during oxidation. Ligand oxidation could also be located further

away due to the smaller redox potential of the iron complex compared to the non-substituted iron complex. Ligand oxidation might interfere with the oxidation peak of the iron redox pair, particularly at higher redox potentials, where for example the oxidation of Dcbpy is located at ca. 1.3 V *vs.* SHE.[48]

Relative standard deviation (RSD) values seem rather large for some of the complexes; however, k_c is a time-dependent variable. k^0 values have high RSD values also and their variation is on the sensitivity of the model; therefore, more accurate values of these could be obtained with the rotating disk electrode (RDE) method, for example. Additionally, we need to keep in mind that the ligand oxidation, as well as OER, are starting to be close to the most positive values, therefore causing a possible deviation to the obtained values by raising the baseline. For example for $[Fe(II)(D(OMe)\text{-}bpy)_3]^{2+}$ complex, the baseline is rising. The reason for this is unknown, and therefore the values obtained for this compound are not as accurate as they would be without the cause of the rising baseline prior to the oxidation peak.

5.2 $[Fe(II)(phen)_3]^{2+}$, $[Fe(II)(DMe\text{-}phen)_3]^{2+}$ and $[Fe(II)(terpy)_2]^{2+}$

The same COMSOL model was also utilized for $[Fe(II)(phen)_3]^{2+}$, $[Fe(II)(DMe\text{-}phen)_3]^{2+}$ and $[Fe(II)(terpy)_2]^{2+}$ to simulate experimental CVs of 5 mM samples in 0.1 M NaCl in **publication II**. The obtained diffusion coefficients were compared to the ones obtained with the Randles–Ševčík equation. Below in **Table 4** are the obtained values. Values are reasonable considering the obtained value for $[Fe(II)(bpy)_3]^{2+}$ earlier in 0.1 M NaCl (2.89×10^{-6} cm^2/s) and regarding the sizes of the compounds.

Table 4. Obtained diffusion coefficients with COMSOL model and Randles–Ševčík equation.[II]

Compound	D_C × 10^6 [cm^2/s]	D_{R-S} × 10^6 [cm^2/s]
$[Fe(II)(phen)_3]^{2+}$	3.38 (8.4 %)	3.32
$[Fe(II)(DMe\text{-}phen)_3]^{2+}$	2.66 (6.5 %)	2.62
$[Fe(II)(terpy)_2]^{2+}$	3.80 (8.2 %)	3.68

The chemical reaction rates were attempted to obtain as 1st and 2nd order reactions (ligand dissociation and dimerization), due to not knowing the rate-limiting step of the decomposition mechanism sequence. The chemical reaction rate should be independent of the scan rate, and we did not find this to be the case. Instead, the chemical reaction rates at higher scan rates were considerably higher. We believe this to be due to not having enough information on the underlying reactions, including ligand oxidation. This data is available at the SI of **publication II**.

5.3 $[Fe(CN)_6]^{3-/4-}$

Simulations of $[Fe(CN)_6]^{3-/4-}$ storage tanks were a part of **publication V**. The experimental CVs were run from the storage tank during battery operation. Experimental and simulated CVs are presented here to show the determination of the concentration via simulations and other fitting parameters. In **Fig 16**, the posolyte CVs are presented with simulated curves on the 45th cycle of a symmetric battery. The model used is described in detail in **publication V**. It uses the interpolation function, interpolating the potential sweep according to the experimental data. This was more convenient since the sweeps start from various OCP values and the sweep direction is changed twice instead of once. Fitting parameters are given in **Table 5**.

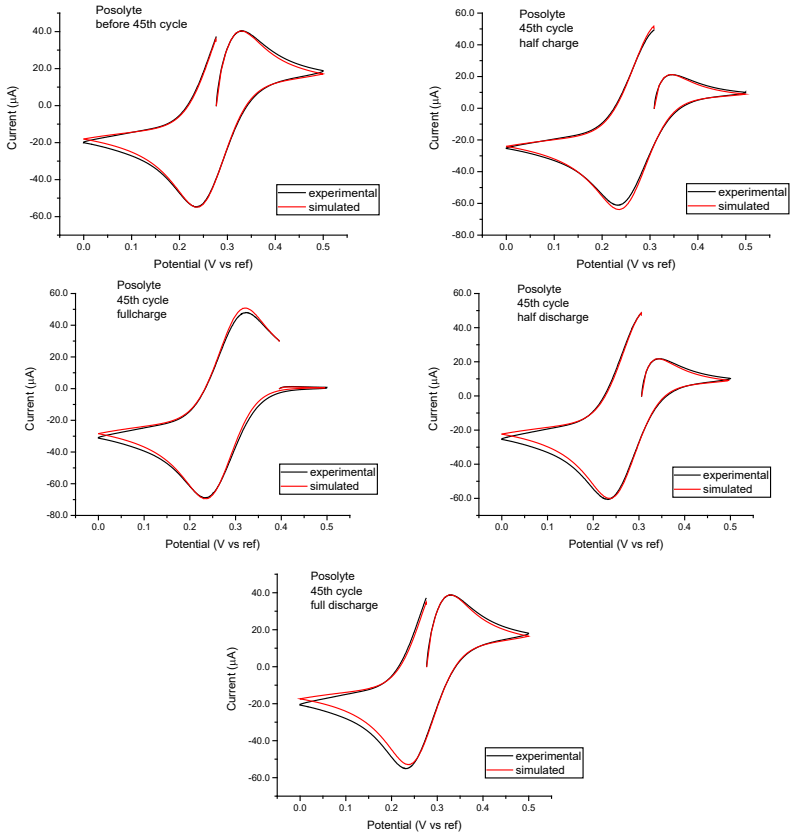

Figure 16. Experimental and simulated CVs of hexacyanoferrate during the 45th battery (symmetric) cycle. The scan rate was 100 mV/s and the WE 3 mm glassy carbon electrode, RE Ag/AgCl, and Pt wire as the counter electrode. The supporting electrolyte was 100 mM NaCl, and the total concentration of the analyte was 5 mM.[V]

Table 5. Obtained D and k^0 values from fitting the simulated CVs to the experimental ones. The concentrations were calculated based on OCP with the Nernst equation.[v]

Posolyte 45th cycle	OCP	c_{0_red} [mM]	c_{0_ox} [mM]	D and k^0 used for fitting
before charging	0.277	2.60	2.40	D 5.13 x10^{-6} cm^2/s k^0 0.04 cm/s
charge at 0.51251 mAh	0.310	1.19	3.81	D 5.70 x10^{-6} cm^2/s k^0 0.04 cm/s
charge at 0.98618 mAh	0.396	0.05	4.95	D 5.80 x10^{-6} cm^2/s k^0 0.04 cm/s
discharge at 0.493 mAh	0.310	1.30	3.70	D 5.10 x10^{-6} cm^2/s k^0 0.04 cm/s
discharge at 0.96594 mAh	0.277	2.60	2.40	D 4.75 x10^{-6} cm^2/s k^0 0.04 cm/s

* For posolyte, the experimental data of full charge was baseline corrected to fit the oxidation current of the Fe(II) due to the low concentration of Fe(II) by deducting the starting value from the current values of the CV.

The model works well in terms of sweeping the potential with the int function. The fitting parameters seem suitable and the simulated CVs fit the experimental ones well with the used values. D value is shifting slightly, but the diffusion coefficients of the negolyte and posolyte seemed to differ from each other from the beginning. Therefore, upon the charge, the posolyte diffusion coefficient fluctuated toward the D value of the negolyte in the discharged state. The opposite was observed for the negolyte; upon charge D value decreases and upon discharge increases. The D values are consistent with the magnitude of literature values (ca. 6-7x10^{-6} cm^2/s).[80,81] The k^0 values seem to agree with each other, although the value is sensitive. The simulations were used to confirm that the total concentration had not decreased, meaning the capacity decay in the battery was not the decomposition of the metal complex in this case, and that the OCP values are accurate in giving the concentration ratios of the studied species in the electrolytes.

5.4 Determination of the number of electrons

For organic compounds, the number of electrons involved in the redox process is not always as straightforward as it is with metal complexes, where the metal center most likely undergoes a one-electron redox process at a time. The COMSOL model was utilized in **publication IV** to determine the number of electrons involved in the redox process for 4-benzoyl-3-ethoxy-5-(hydroxymethyl)-1,2-dimethylpyridin-1-ium iodide in 0.1 M NaOH, where the peak separation and Randles–Ševčík analysis

suggested a 2-electron redox process. However, the process was quasi-reversible at 10 mM concentration. Hence, the roles of the iR drop and k^0 on the electrochemical reaction were evaluated with COMSOL simulations.

The determined diffusion coefficient by NMR studies was 4.33×10^{-6} cm^2/s for a 10 mM compound. Finite element simulations agree with this value for the 2-electron redox process, as seen in **Figure 17** below with the parameters used in the simulations.

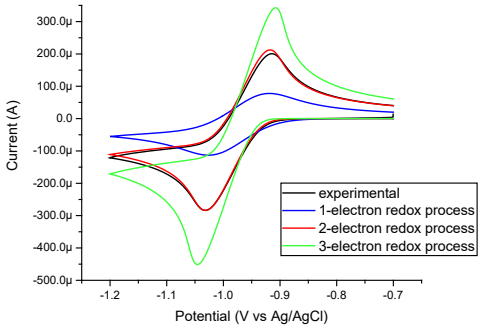

Parameter	Value	Unit
D	4.13×10^{-6}	cm^2/s
k^0	0.0088	cm/s
alpha	0.5	
n	1, 2, 3	
scan rate	100	mV/s
c	10	mM

Figure 17. Experimental CV (black) with simulated CVs of 1-, 2- and 3-electron redox processes. The parameters used are presented in the table next to the graph.[IV]

5.5 Sensitivity of the model

COMSOL simulations include the effects of the Ohmic drop and quasi-reversible kinetics, allowing the evaluation of the electrochemical parameters of these kinds of systems. Sensitivity was originally described in **publication I**, but the simulations in **publications II and V** showed the problems in the model simplicity when complex decomposition routes affect the current baseline and absorbance occurs.

For all studied iron complexes with bpy, phen, and terpy ligands, the current rises on the forward scan after the oxidation peak, and for some also before the oxidation peak, causing deviations in the obtained parameters due to the model only focusing on the redox pair reactions. These rising baselines can be, in certain cases, due to oxidation of the ligand (which is near the oxidation of the Fe(II) complex), OER, electrolyte effects (especially in low concentrations of the analyte), and adsorption. None of these phenomena were modelled due to a lack of knowledge of the underlying processes.

The model was found to be rather sensitive to k^0 and k_c values. Even large changes in k^0 values were not necessarily visible on the simulated CV curves since the obtained values are rather small, considering their effect on the simulated curve.

D was a less sensitive parameter, but the rising baseline might slightly affect the determination of this value for some of the studied compounds.

During the evaluation of Fe(II) complexes with phen and terpy ligands, k_c seemed to be reliant on the scan rate. This led to the conclusion that the baseline might influence this value by increasing more at higher scan rates after the Fe(II) oxidation. This could originate from ligand oxidation. We are determining the k_c value from the returning current, so the shifts in baselines expose the determined values for deviations.

For hexacyanoferrates, which are a simple, reversible, and stable system, the model worked well. This was most likely due to not having a rising baseline after the iron redox peak, as the redox potential is at rather low potentials away from OER.

All in all, we concluded the model is too simple as it is for some of the studied complexes. Possible deviations from the determined values are caused by rising baselines. There are many options for rising baselines: OER, ligand oxidation, other side reactions, electrolyte effects, and adsorption. Introducing all of these to the model would improve the accuracy of the simulations, but it would require detailed information on each process. Unfortunately, this is not possible due to too many unknown variables. However, we still believe that the model can be used to evaluate the kinetic parameters and reversibility of the system.

6 Flow battery studies

$[Fe(II)(bpy)_3]^{2+}$, $[Fe(II)(DMe\text{-}bpy)_3]^{2+}$, $[Fe(II)(bpy)(CN)_4]^{2-}$, $[Fe(II)(phen)_3]^{2+}$, $[Fe(II)(DMe\text{-}phen)_3]^{2+}$ and $[Fe(II)(terpy)_2]^{2+}$ lab-scale flow battery results are discussed next in parts, after which they are compared.

6.1 $[Fe(II)(bpy)_3]^{2+}$, $[Fe(II)(DMe\text{-}bpy)_3]^{2+}$ and $[Fe(II)(bpy)(CN)_4]^{2-}$

$[Fe(II)(bpy)_3]^{2+}$ experiences the charge originally in one plateau and discharge in 2 plateaus, leading to a voltage drop and poor energy efficiency as seen in **Fig 18**. According to the literature, the higher charge and discharge plateaus originate from the charge and discharge of the monomer, and the lower voltage discharge plateau originates from a dimer formed of charged monomers via an oxo-bridge.[56] During cycling, an additional charge plateau forms at a lower voltage. This is expected to originate from monomer charge with one ligand dissociated, as the difference in the voltage plateau (ca. 300 mV) of $[Fe(II)(bpy)_3]^{2+}$ and this additional plateau suggests, as it corresponds to the difference in reduction potentials of $[Fe(II)(bpy)_3]^{2+}$ (1.03 V *vs.* SHE) and (0.78 *vs.* SHE) reported for $[Fe(II)(bpy)_2]^{2+}$.[46] During cycling, the side reactions forming the $[Fe(II)(bpy)_2]^{2+}$ species and dimer seem to slow down, most probably due to decreased capacity utilization, and the resulting lower concentration of the dimer decomposition species. The increased current density has the same effect.

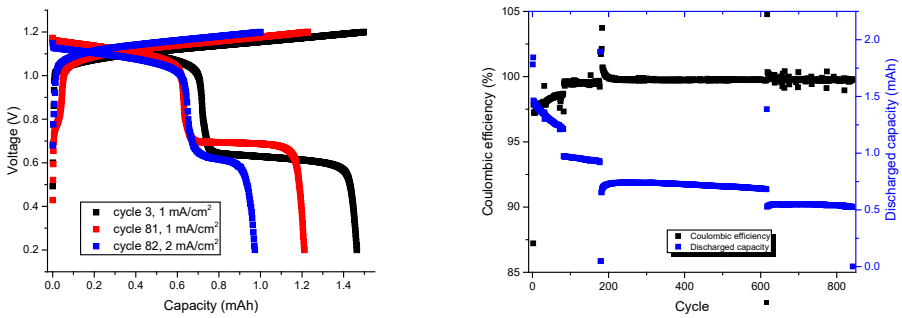

Figure 18. $[Fe(II)(bpy)_3]^{2+}$ 5 mM in 0.1 M NaCl against AZON3 (10 mM). On the left are capacity-voltage curves, and on the right CE and discharged capacity *vs.* cycle number.[V] Graphs are also discussed in section 7.2. Breaks in the latter curve data correspond to changes in the cut-offs and/or current densities, leading to changes in capacity utilization.

$[Fe(II)(DMe\text{-}bpy)_3]^{2+}$ battery (2 mM) was cycled as a symmetric battery, and its capacity decay was determined to be 0.35 % per cycle in **publication I**. This high capacity decay was not obtained from a linear curve, as seen in **Fig 19**. Due to the charge as one plateau and discharge as 2 plateaus, we believe this one also has dimerization. We ran this also as an asymmetric battery *vs.* NDI (**publication I**), where the plateaus were more clearly seen, due to having a one charge and discharge plateau from NDI.

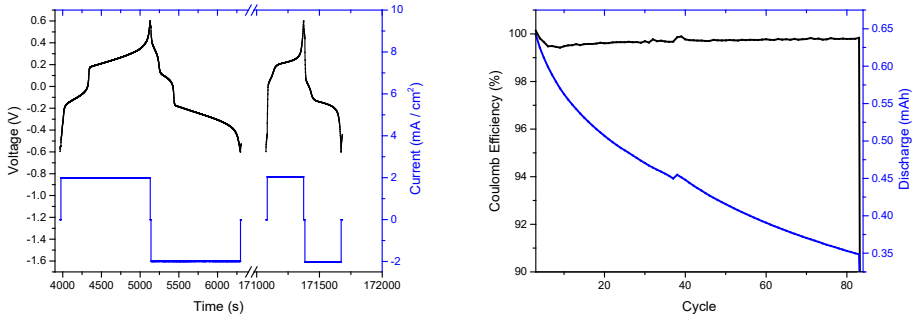

Figure 19. $[Fe(II)(DMe\text{-}bpy)_3]^{2+}$ battery (2 mM) was run as a symmetric battery against $[Fe(III)(DMe\text{-}bpy)_3]^{3+}$ in 0.1 M K_2SO_4. On the left are time-voltage curves, and on the right CE and discharged capacity *vs.* cycle number.[I]

From $[Fe(II)(bpy)(CN)_4]^{2-}$ battery against $[Fe(III)(CN)_6]^{3-}$ (unpublished result) (**Fig 20**), we can see that the charge and discharge occur in 1 plateau each. The capacity decay of 0.0099 % per cycle is the best value obtained in this work. The

commercial compound was impure after the primary battery tests, leading to a concentration approximated to 1.7 mM from the obtained capacity in lab-scale FB tests. The compound could not be purified further, however, it shows promise in asymmetric ligand design to block side reactions of the charged monomer.

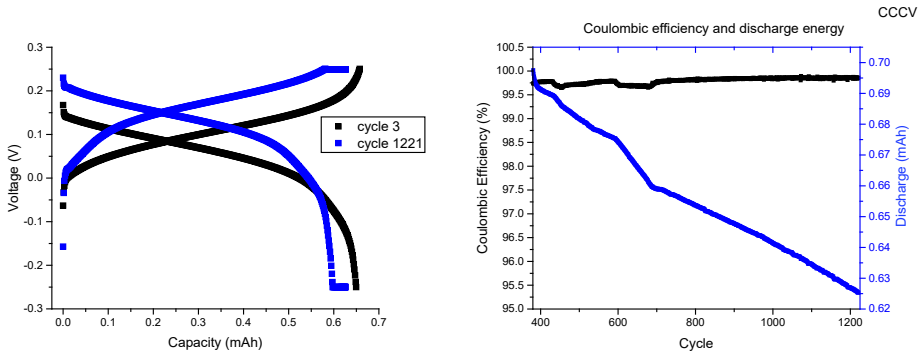

Figure 20. $[Fe(II)(bpy)(CN)_4]^{2-}$ in pH 10 carbonate buffer, reached capacity at the first cycle was 0.83 mAh corresponding to ca. 2 mM sample, CCCV was used for charging and discharging. Negolyte was $[Fe(III)(CN)_6]^{4-}$. This is an unpublished result.

To conclude these graphs, $[Fe(II)(bpy)_3]^{2+}$ and $[Fe(II)(DMe\text{-}bpy)_3]^{2+}$ dimerized in the oxidized state during battery studies, as seen from the lower discharge plateau and literature.[56] However, the preliminary FB studies of $[Fe(II)(bpy)(CN)_4]^{2-}$ show only one discharge plateau, indicating increased stability and no occurring dimerization with obtained capacity decay of 0.0099 % per cycle. Nevertheless, the cycled capacity was ca. 1.7 mM, clearly smaller than the other studied compounds, meaning the dimerization rate might not be enough to be visible during cycling. The commercial compound was found to be impure after the primary battery tests and could not be purified further. However, the preliminary result of the asymmetric Fe(II) complex with bpy and CN ligands agrees with the compound reported in the literature, $[Fe(II)(Dcbpy)_2(CN)_2]^{4-}$, where the dimerization was suppressed and the cycling stability of the iron complex was significantly improved with blocking the dimerization.[48]

6.2 $[Fe(II)(phen)_3]^{2+}$, $[Fe(II)(DMe\text{-}phen)_3]^{2+}$ and $[Fe(II)(terpy)_2]^{2+}$

In **publication II**, $[Fe(II)(phen)_3]^{2+}$ battery (**Fig 21**) exhibited a large capacity decay, losing over 60 % of the accessed capacity during the first 30 cycles, after which the capacity stabilized to 0.5 mAh. The charge occurs initially as one charge plateau and the discharge in 2 plateaus. This behaviour is similar to the one obtained earlier for

$[Fe(II)(bpy)_3]^{2+}$, and as is reported in the literature, indicating the discharge product at the lower voltage plateau is a dimer of the Fe(III) species.

When the discharge plateau at lower potential decreases, we can see that the CE value increases to 97.5 %, meaning the discharged side product at lower voltage is not completely reversible. While the discharge plateau at lower potentials decreases during cycling in capacity, the higher discharge plateau decreases much less in size compared to the initial capacity. During battery cycling, we are also obtaining a new charge plateau at a lower potential, which is most likely originating from the decomposition products of either the charged monomer or during the discharge of the molecule responsible for the lower discharge plateau. Therefore, it could originate from one ligand lost species, similar to $[Fe(II)(bpy)_3]^{2+}$.

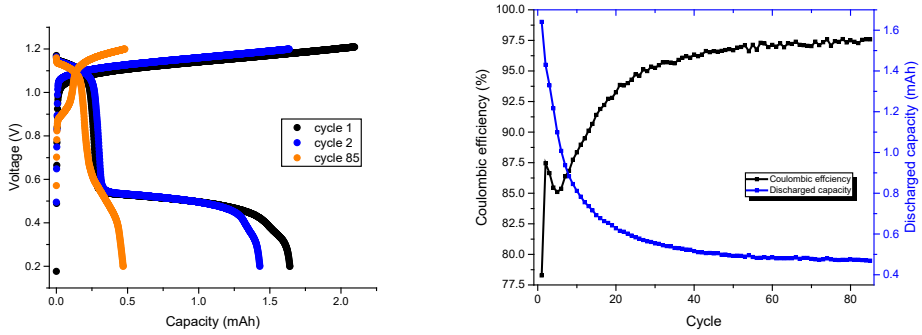

Figure 21. 5 mM $[Fe(II)(phen)_3]^{2+}$ battery in 0.1 M NaCl. Current density 1 mA cm^{-2}, expected capacity 2 mAh, capacity utilization 80 %. On the left: capacity-voltage curves from different cycles. On the right: capacity decay with the CE.[II]

$[Fe(II)(DMe\text{-}phen)_3]^{2+}$ (**Fig 22**) was also cycled at a low concentration of 5 mM. The results were presented in **publication II**. 2 discharge plateaus were detected, one at the charging voltage and another at a lower voltage, indicating dimerization as the reason for the lower discharge plateau, as also a pH drop was detected, agreeing with the side reaction mechanisms presented earlier. For the first 10 cycles, the discharge cut-off was kept at a higher voltage and after that, the discharge cut-off was lowered to 0.1 V. This led to a capacity increase, as we can see in Fig **17** below. The first discharge plateau at lower voltage was higher in capacity than the following ones, indicating we could discharge the side products formed during cycling at higher cut-offs, and in the next cycle they were charged and discharged as monomers. It is worth noting, that the size of the lower discharge plateau is smaller compared to the monomer discharge plateau for $[Fe(II)(phen)_3]^{2+}$ compound. This

could also be the reason for the lower capacity decay of 0.06 % per cycle (2.78 % per day).

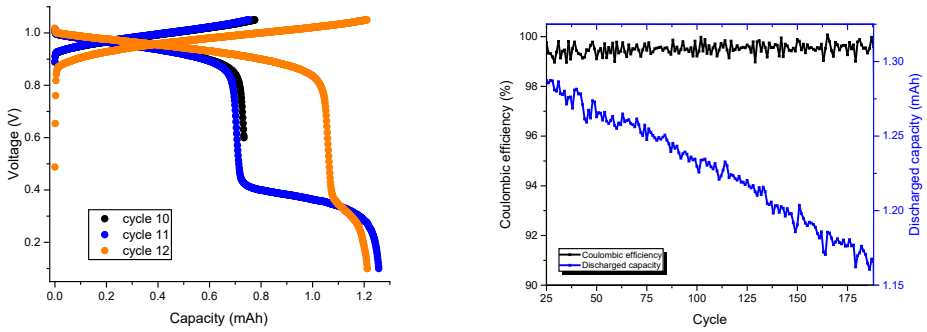

Figure 22. 5 mM $[Fe(II)(DMe\text{-}phen)_3]^{2+}$ battery in 0.1 M NaCl. Used current density 1 mA cm^{-2}, expected capacity 2 mAh. On the left: charge-discharge plateaus with altering cut-offs of 0.6 V and 0.1 V for discharge, and for charge 1.05 V. On the right: discharged capacity and CE *vs.* cycle number with cut-offs 0.1–1.05 V.[II]

5 mM $[Fe(II)(terpy)_2]^{2+}$ battery (**Fig 23**) also exhibited discharge on lower potentials than the charge, while one discharge plateau was located at the higher voltage of the charging plateau, as reported in **publication II**. The relatively low CE of 98.5 % and the capacity decay of 0.16 % per cycle (10.1 % per day) indicate that the electrons used in the charging process for side reactions are not utilized fully during discharge, indicating the side reactions are not fully reversible. The rising trend of the CE indicates, that the decreasing concentration of the active compound might be stabilizing the battery, as the charged species concentration becomes smaller and the Fe(III) species are further from each other, leading to a smaller amount of side reactions upon decomposition of the compound. pH drop as well as the lower discharge plateaus indicate dimerization while the ligand is tridentate and possibly differs in some way. We do suggest that there is dimerization due to the mentioned observations and the similar structure to the $[Fe(II)(bpy)_3]^{2+}$ and $[Fe(II)(phen)_3]^{2+}$ molecules. In addition, ligand dissociation could be one of the observed side reactions visible during battery cycling.

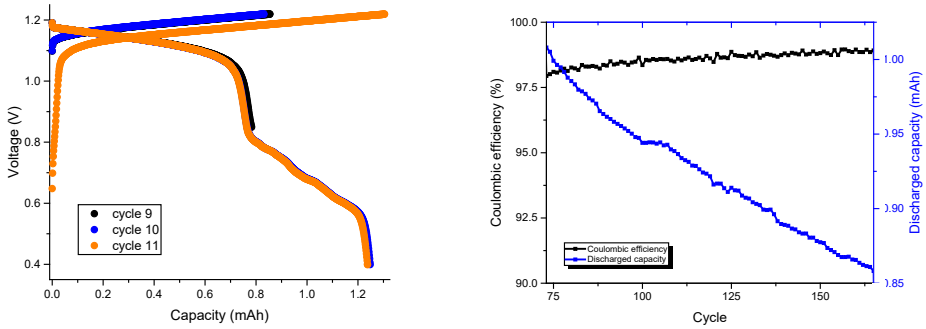

Figure 23. 5 mM $[Fe(II)(terpy)_2]^{2+}$ battery in 0.1 M NaCl. Expected capacity 2 mAh, capacity utilization 62 %, current density 1 mA cm^{-2}. On the left: capacity-voltage curves, cut-offs 0.85 V and 0.4 V for discharge, for charge 1.22 V. On the right: discharged capacity and CE *vs.* cycle number. Cut-offs 0 and 1.22 V.[II]

All compounds in this subsection show discharge plateaus at lower potentials, therefore, side reactions are present that decrease the energy efficiency of the battery. Strategies shown next were intended to decrease the side reactions within $[Fe(II)(terpy)_2]^{2+}$ and $[Fe(II)(DMe\text{-}phen)_3]^{2+}$ posolytes, as reported in **publication II**.

Increasing the current density helped to decrease the sluggish side reactions of the $[Fe(II)(terpy)_2]^{2+}$ battery (**Fig 24**), however, we are cycling a very small concentration of the active material, therefore decreasing the concentration of the oxidized species that could be going through side reactions. Below we can see the difference in the disappearing extra charge plateau and more separated discharge plateaus at lower voltage to state that the side reactions were decreased with increasing current density. CE increases to 99.5 % from 98.6 %, indicating better utilization of electrons to discharge the battery. Capacity decay was not detectable until the cut-off for charging was increased, again resulting in capacity decay due to utilization of higher concentration of the charged Fe(III) species, and therefore an increase in side reaction products.

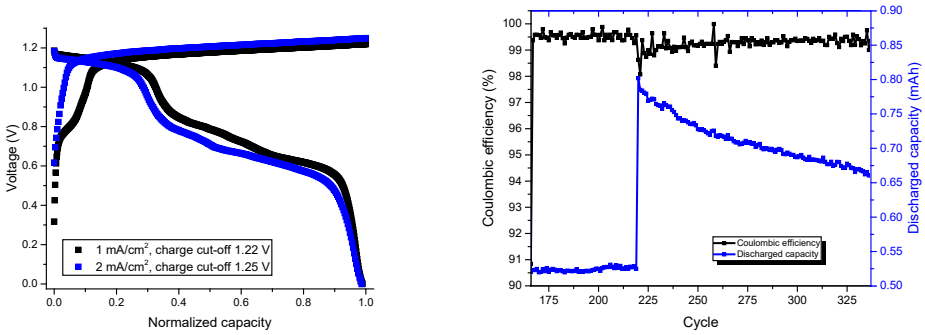

Figure 24. $[Fe(II)(terpy)_2]^{2+}$ battery On the left: capacity-voltage curves with different current densities and charge cut-offs. Capacity is normalized. On the right: Coulombic efficiency and capacity *vs.* cycle number with charge cut-off 1.22 V and charge cut-off 1.25 V, current density in both 2 mA cm^{-2}.[II]

Of the studied compounds in this subsection, the $[Fe(II)(DMe\text{-}phen)_3]^{2+}$ had the smallest lower voltage discharge plateau in size compared to the monomer discharge plateau, leading to further studies in a lab-scale FB. Below in **Fig 25**, we can see an attempt to improve the energy efficiency of the battery by cycling at higher cut-offs for 10 cycles, after which the material and side reaction products were discharged in one cycle at a lower discharge cut-off.

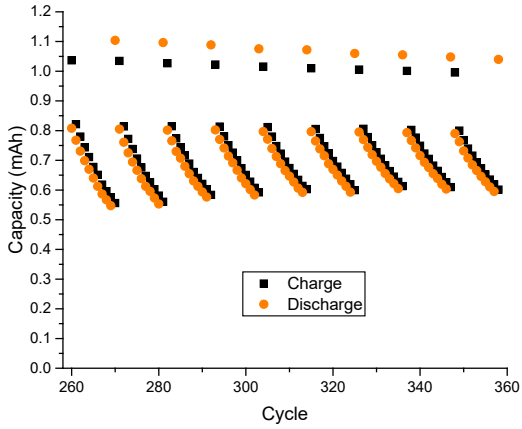

Figure 25. $[Fe(II)(DMe\text{-}phen)_3]^{2+}$ battery. Repeatedly 10 cycles cycled at 0.6–1.05 V after which 1 cycle with a lower discharge cut-off of 0 V to recover the capacity lost in those 10 cycles.[II]

6.3 Comparison of the battery studies

All the studied compounds, excluding $[Fe(II)(bpy)(CN)_4]^{2-}$, experienced discharging in 2 or more plateaus. $[Fe(II)(bpy)_3]^{2+}$ and $[Fe(II)(phen)_3]^{2+}$ experienced similar discharge behavior with 2 discharge plateaus; one at the same voltage as the charge occurred and another one at a significantly lower voltage. $[Fe(II)(terpy)_2]^{2+}$ experienced the discharge in several plateaus; one at a voltage corresponding to the charge plateau of the complex and ca. 2-3 other plateaus at lower potentials, which were not well separated from one another. $[Fe(II)(bpy)_3]^{2+}$, $[Fe(II)(phen)_3]^{2+,}$ and $[Fe(II)(terpy)_2]^{2+}$ also developed a new charging plateau at a lower potential than the original charge plateaus, that could be originating from the monomer that has lost one ligand as a result of dimer discharge or ligand dissociation. However, the discharge of the asymmetric $[Fe(II)(bpy)(CN)_4]^{2-}$ only in one plateau corresponding to the voltage of the charge, gives us an indication that the asymmetric metal complex design could be one of the keys to blocking the dimerization and the resulting side reactions, as is also reported rather recently in the literature for $[Fe(II)(Dcbpy)_2(CN)_2]^{4-}$.[48]

The discharge plateau at a lower voltage for $[Fe(II)(bpy)_3]^{2+}$ is associated with the dimerization of 2 charged monomers of $[Fe(III)(bpy)_3]^{3+}$ via an oxo-bridge, as reported in the literature by Holubowich et al.[56] The dimerization process was described in this thesis with the appropriate literature references in section 2.2.2.3. This side reaction process occurring to the oxidized species can be suggested to $[Fe(II)(phen)_3]^{2+}$ and $[Fe(II)(terpy)_2]^{2+}$ complexes, among the studied $[Fe(II)(bpy)_3]^{2+}$ complexes. $[Fe(II)(phen)_3]^{2+}$ has a very similar structure to $[Fe(II)(bpy)_3]^{2+}$ as well as battery performance with 2 discharge plateaus of which the other one is located at a lower voltage, while also an additional charge plateau at lower voltage is being formed, believed to be originating from the monomer with 2 ligands. $[Fe(II)(terpy)_2]^{2+}$ also has a similar structure to $[Fe(II)(bpy)_3]^{2+}$, however, it is tridentate instead of bidentate, but the ligand structure can be considered similar. pH drop during battery cycling for the compounds where the lower discharge plateau is detected increases the suspicion that one of the side reactions is dimerization occurring in the battery.

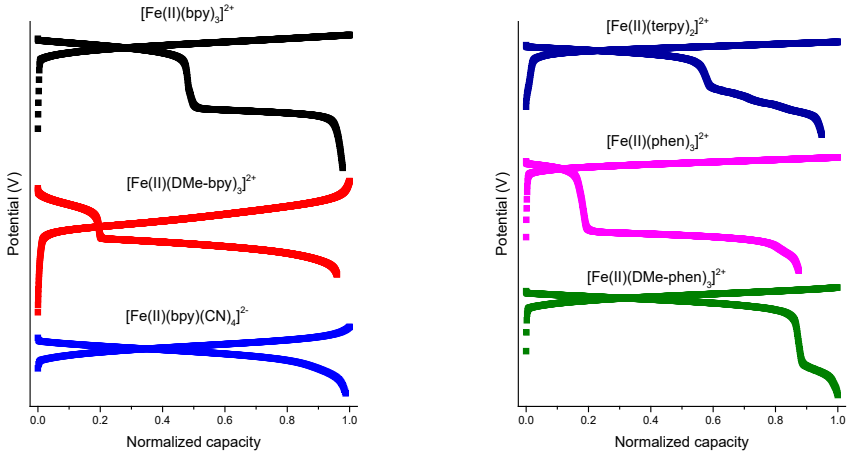

Figure 26. Normalized charge and discharge plateaus of the studied compounds: $[Fe(II)(bpy)_3]^{2+}$, $[Fe(II)(DMe\text{-}bpy)_3]^{2+}$ and $[Fe(II)(bpy)(CN)_4]^{2-}$ on the left, $[Fe(II)(phen)_3]^{2+}$, $[Fe(II)(DMe\text{-}phen)_3]^{2+}$ and $[Fe(II)(terpy)_2]^{2+}$ on the right. It is worth noting, that the plateaus are not exactly comparable due to different conditions regarding the concentration of the posolyte, electrolyte, capacity utilization, etc., but they do give an idea of the ratio of the side reaction. The potential scale values have been removed due to different negolytes, and the capacity was normalized with the value of the charged capacity of the cycle shown.

From **Fig 26**, we can see that the sizes of the dimerization discharge differ. We do note that the concentrations and cycling conditions, such as capacity utilization, etc., are differing, hence affecting these results. Therefore, we are evaluating these rather qualitatively. However, we can say that the batteries, where the dimerization discharge plateau was half or over half of the discharged capacity at the beginning of the cycling, had non-linear capacity decay (**Figs 18, 19,** and **21**). We believe this is due to accelerated dimerization. After the concentration decreases due to decomposition resulting from dimerization, we obtain a decrease in the capacity decay rate. Capacity decay rates were not calculated for these compounds: $[Fe(II)(bpy)_3]^{2+}$, $[Fe(II)(DMe\text{-}bpy)_3]^{2+}$ and $[Fe(II)(phen)_3]^{2+}$. However, capacity decays for the other studied compounds were calculated, and they are compared in **Fig 27** to values gathered from literature, noting that $[Fe(II)(DMe\text{-}phen)_3]^{2+}$ and $[Fe(II)(terpy)_2]^{2+}$ discharge in 2 or more plateaus. It is also worth noting that the FB cycling conditions in the batteries are different, therefore, the capacity decays are not exactly comparable. The capacity decay rates are compared to the redox potentials, as both are important factors for flow battery performance; redox potential should be as high as possible within the electrolyte (water) stability window, and the

capacity decay should be as low as possible. **Fig 27** shows that our compounds have relatively high capacity decay values, while the redox potentials are competitive.

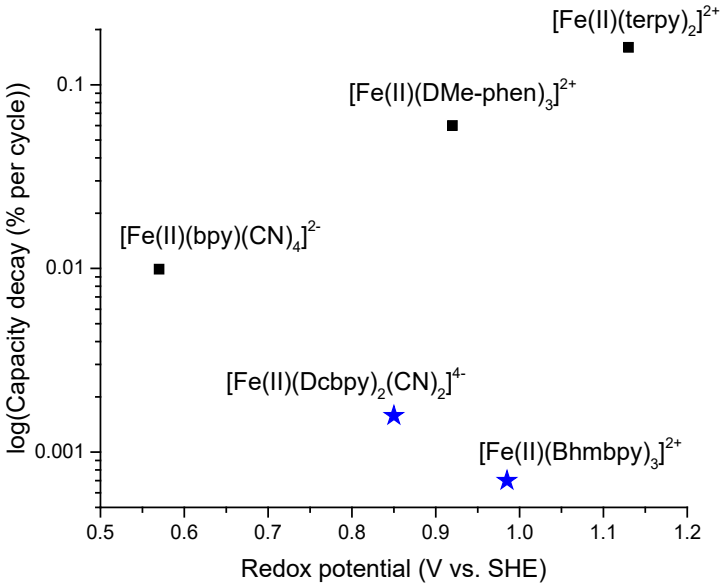

Figure 27. Redox potential vs capacity decay. Our best-performing compounds are marked with black squares and compounds from the literature[48,52] with blue stars.

With high redox potentials, the electrodes might suffer from carbon corrosion,[82] which could be seen as an increase in the system resistance. During our studies, we detected a rise in the cell voltage at the end of the charging process, which might originate from the electrode corrosion. However, this voltage increase can also be attributed to the side reactions of the studied complexes, like ligand oxidation, which might also form a layer on the electrode surface and increase the cell resistance. Further studies are needed to investigate the origin of the cell voltage increase.

The most relevant problem for these complexes when considering the flow battery operation is that when left in the charged state, these would, in time, increase the concentration of dimers. The higher the amount of time in the charged state is, the more of the other side reaction products are also formed, and those side reactions might not be as reversible as dimerization. Those side reactions are, for example, oxidation of the ligand, which cannot be re-coordinated to the iron center without reduction and deprotonation. Dimerization, while being a rather reversible process, also leads to proton release, which leads to self-discharge of the charged monomers.

Having the battery in a charged state is therefore not beneficial in the cases with dimerization, yet needed for a flow battery.

Additionally, the dimerization leads to poor energy efficiency, as some capacity is discharged at a lower voltage than charged. This is not practical for a flow battery application. Higher current densities could prevent some of the side reactions, but the battery would need to be discharged fast to prevent side reactions and the capacity utilization would be lowered significantly. Running the battery at a low concentration is not practical due to energy density; the battery size would increase considerably. Also, the strategy of cycling at higher cut-offs and then discharging the battery at lower voltage in one cycle would be problematic from the application view, since it would not take out the dimerization, we would only be improving the energy efficiency of the battery for a while, but the dimer concentration would be increasing during high cut-off voltage cycling, and with that the side reactions.

Regarding side reactions, in aqueous solutions, we are always prone to water´s nucleophilic attacks on the structure, while the metal complex center ion can be attacked by a chloride ion too. In this thesis work, all the batteries had a low concentration (5 mM or less) when they were studied in a flow battery, therefore neglecting the need to use a higher amount of the supporting electrolyte (0.1 M NaCl *vs.* 1 M NaCl), which could, in turn, accelerate the side reactions, if chlorides were a significant participant in side reactions. In all batteries, we can see an attempt to stabilize the capacity at a certain low value, where the analyte concentration must have reached a low enough value for the side reactions to have slowed down.

The solution to the voltage drop and low concentration would be to decrease the amount of the side reactions. This could be done by introducing CN ligands to the Fe(II) center with the used ligands; hence, improving the iron complex stability while keeping the redox potentials sufficiently high. CN ligands alter the redox potential to lower potentials, therefore decreasing the cell potential. However, as suggested by the performance of $[Fe(II)(bpy)(CN)_4]^{2-}$ (redox potentials 0.57 V *vs.* SHE; capacity decay 0.0099 % per cycle) in our studies, that could be a working solution. While the capacity decays are not exactly comparable, since the cycling conditions differ from one another, we are comparing this to $[Fe(II)(Dcbpy)_2(CN)_2]^{4-}$ reported in the literature (redox potentials 0.85 V *vs.* SHE; capacity decay 0.00158 % per cycle).[48] We can see that the asymmetric ligand design seems like a solution to block dimerization. Adding EWGs to the ligand structure avoids the problem of having a rather low redox potential when CN ligands are in the structure, as our asymmetric compound had without electron-withdrawing functional groups.

Finally, asymmetry would increase solubility, leading to possibilities for calculating the possible energy density and power values, as they require battery studies at higher concentrations. If a reasonable solubility would be reached and the redox potential would be sufficiently high, the cell voltage and power could be

increased, leading also to optimization of the battery set-up. However, among these compounds, a suitable candidate without side reactions and with high redox potential and solubility was not found. The focus in the future will be on adding asymmetry into the structure to achieve a well-performing redox material in all three aspects (high solubility, redox potential and stability). If successful, higher concentration FB measurements could be performed, and the resulting energy efficiency, power and cost per kWh could be calculated and compared to the existing FB materials.

7 Combined CV and flow battery studies for SOC and detection of redox-active side reactions

As mentioned earlier, the idea was to obtain SOC via half-cell OCP and simulations of peak currents of CVs. In addition, information on the changes in the redox active species during charging and discharging was obtained, as reasons for capacity decay.

Concentrations were obtained from half-cell OCP and validated with CV peak currents via COMSOL simulations. The SOC obtained from these was then separately compared to the theoretical Nernst equation. A COMSOL simulation model with an interpolation function to tie the experimental time and potential to the simulations was utilized, and the most relevant simulation results were discussed in section 5.3. Further information is in **publication V and its SI**. The number and the behavior of the redox active species were monitored as well as their changes in current, peak position and whether they were present or not at certain stages of the charging and discharging.

Next, we are going through the samples here one by one, starting with hexacyanoferrates and continuing with $[Fe(II)(bpy)_3]^{2+}$, after which a comparison of these is performed in terms of the usability of the method of studying the compounds in question.

7.1 $[Fe(II)(CN)_6]^{4-}$ / $[Fe(III)(CN)_6]^{3-}$

A symmetric lab-scale flow battery of iron(II) and iron(III) hexacyanoferrates was run on a lab table without a nitrogen atmosphere, and results were reported in **publication V**. The concentration of both species was 5 mM, the supporting electrolyte was 100 mM NaCl and the pH of the sample solutions was adjusted to 7.5. Cut-offs for the first 15 cycles were 0.4 V and -0.4 V, and for the rest of 30 cycles 0.3 V and -0.3 V, the current density was 1 mA/cm^2, and the protocol was CC. Cyclic voltammograms were recorded before the battery cycle, at half-charge, full charge, half-discharge, and full discharge for battery cycles 1 and 45. The battery showed a rather linear capacity decay of 0.98 % per cycle as shown in **Fig 28**. CE is 99.5 %. This capacity fade rate was rather surprising since hexacyanoferrate is the

most stable iron complex tested in FB, with 100 % retention capacity under the best conditions.[83,84] However, the conditions of this battery were not optimized.

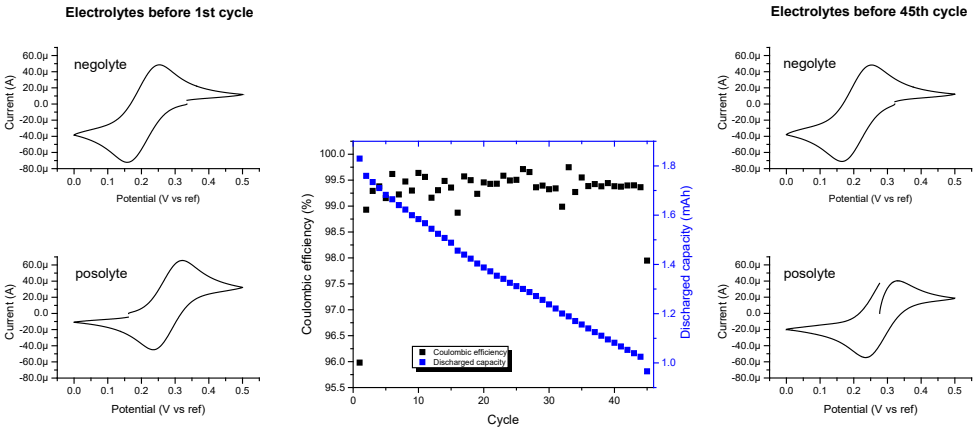

Figure 28. $[Fe(II)(CN)_6]^{4-}$ / $[Fe(III)(CN)_6]^{3-}$ battery. Discharged capacity and CE *vs.* cycle number.Posolyte and negolyte 5 mM in 100 mM NaCl. pH adjusted before the battery to 7.5. Cut-offs for the first 15 cycles were 0.4 V and -0.4 V and for the rest of the 30 cycles 0.3 and -0.3 V. The current density was 1 mA/cm^2. For CVs, WE was glassy carbon (diameter 3 mm), scan rate 100 mV/s. Both electrolytes had their own reference electrodes (same material Ag/AgCl), explaining the slight differences in the potential axis.[V]

The capacity decay was unexpected. The half-cell OCP values and the CVs show that the posolyte is imbalanced (**Fig 29**) after the 45th cycle compared to the negolyte. However, it does not seem to be a decomposition, as the returning peak current is at the same value as in the beginning. With COMSOL simulations of the experimental CVs (**Fig 29**), the total concentration on the posolyte side was confirmed to stay at 5 mM. Simulation results were given in section 5.3 and **publication V and its SI**, and they confirmed the Fe(III) concentration increasing on the posolyte side; Fe(II) starting concentration before the 45th cycle was 2.60 mM and Fe(III) starting concentration was 4.94 mM on negolyte side. The posolyte Fe(II) concentrations regarding the first and 45th cycle correspond to the charged capacities in the battery data: the 1st cycle c(Fe(II)) = 4.60 mM (OCP 209 mV) with 1.83 mAh battery capacity reached, and the 45th cycle c(Fe(II)) = 2.60 mM (OCP 277 mV) with 0.97 mAh. One explanation for the imbalance on the posolyte side would be the oxidation of Fe(II) to Fe(III) due to the non-inert atmosphere, catalyzed by the Pt wire used as the CE in the tanks. However, oxidation of Fe(II) to Fe(III) to occur also on the negolyte side is possible.

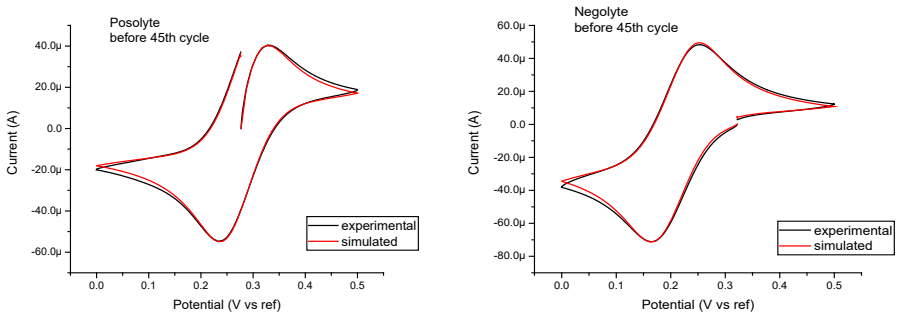

Figure 29. CVs of the posolyte and negolyte before the 45th cycle, black is experimental and red simulated. Both total concentrations were 5 mM. as determined by the simulations presented in section 5.3 and **publication V**.[V]

In **Fig 30** the half-cell SOCs were obtained via concentration determination via half-cell OCP with the Nernst equation, resulting in graphs of half-cell SOC *vs.* experimental charged capacity of the battery. We can see that the determination of the half-cell SOC from OCP fits well with the experimental charged capacities. Fe(II) and Fe(III) concentrations for SOC from half-cell OCP values on the negolyte and the posolyte sides were confirmed with simulations. The determined half-cell SOC values fluctuate on the 45th cycle between ca. 50-100 % SOC for the posolyte, whereas for the negolyte the half-cell SOC values change between 0 to ca. 50 %. This is consistent with the CVs presented in **Figs 28 and 29**, as well as with the shifts in the half-cell OCP values and battery capacity values. In addition, the color change of posolyte from pale yellow to yellow, as was the negolyte color, seems to support the Fe(II) forming Fe(III) on the posolyte side. With all the obtained data, the Fe(II) formation to Fe(III) is evidenced as the reason for the imbalance and detected capacity decay on the battery. Most likely, this is chemical oxidation due to a non-inert atmosphere, catalyzed by Pt wire. This reaction could be prevented by utilizing for example carbon as counter electrode.

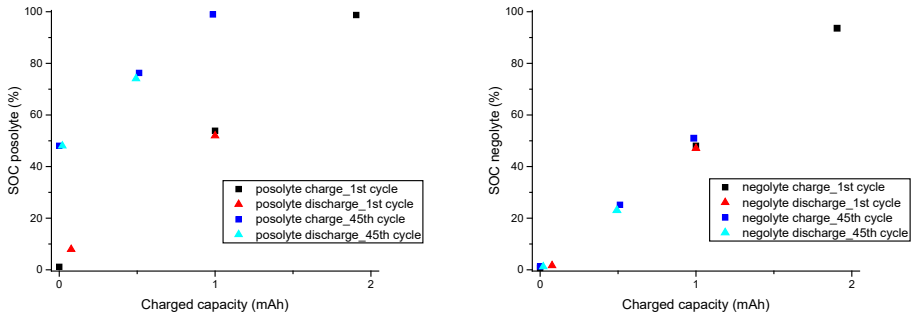

Figure 30. SOC was calculated from OCP values of half-cells and graphed as a function of OCP for both posolyte and negolyte.[V]

Regardless of the reasons behind the capacity decay, the CV and OCP measurements with simulations of experimental CV peak currents seem accurate ways to determine SOC during battery operation for a simple redox reaction that hexacyanoferrates possess. Studying each side individually helps detect the limiting side of the battery that causes the capacity decay. It also helps explain why capacity decay occurs, whether it is self-discharge or decomposition. Most importantly, this information is available reliably during FB operation.

7.2 $[Fe(II)(bpy)_3]^{2+}$

For $[Fe(II)(bpy)_3]^{2+}$, the battery data is given below in **Fig 31** as in **publication V**. This data was shown in **Fig 18** in section 6.1. The capacity decay (0.024 % per cycle, CE 99.7 %) is evident from the battery data. Additionally, the characteristic behavior of $[Fe(II)(bpy)_3]^{2+}$ in FB is noticed, as the charged species is discharged as monomer and dimer in 2 different voltage plateaus, of which higher voltage plateau is the charged monomer and the lower the dimer.[56] The forming additional charge plateau at a lower potential is suggested to be the one ligand lost $[Fe(II)(bpy)_2]^{2+}$ as its reduction potential is at 0.58 V *vs.* Ag/AgCl,[46] and of $[Fe(II)(bpy)_3]^{2+}$ is 0.87 V *vs.* Ag/AgCl.[49] This is consistent with the battery data of ca. 300 mV difference between the charge plateaus.

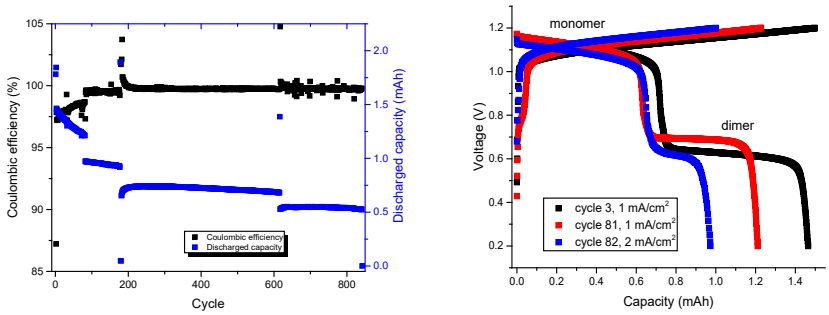

Figure 31. $[Fe(II)(bpy)_3]^{2+}$ battery against AZON3 in 100 mM NaCl, pH adjusted to 7 before the battery cycling. The capacity decay and CE *vs.* cycle number are on the left, and on the right are the voltage-capacity curves.[v] Breaks in the former curve data correspond to changes in the cut-offs and/or current densities, leading to changes in capacity utilization.

CVs were measured in the storage tank of the $[Fe(II)(bpy)_3]^{2+}$ to obtain information on the redox processes present during charge and discharge. The following CVs were obtained as presented in **Fig 32** during the first charge-discharge cycle.

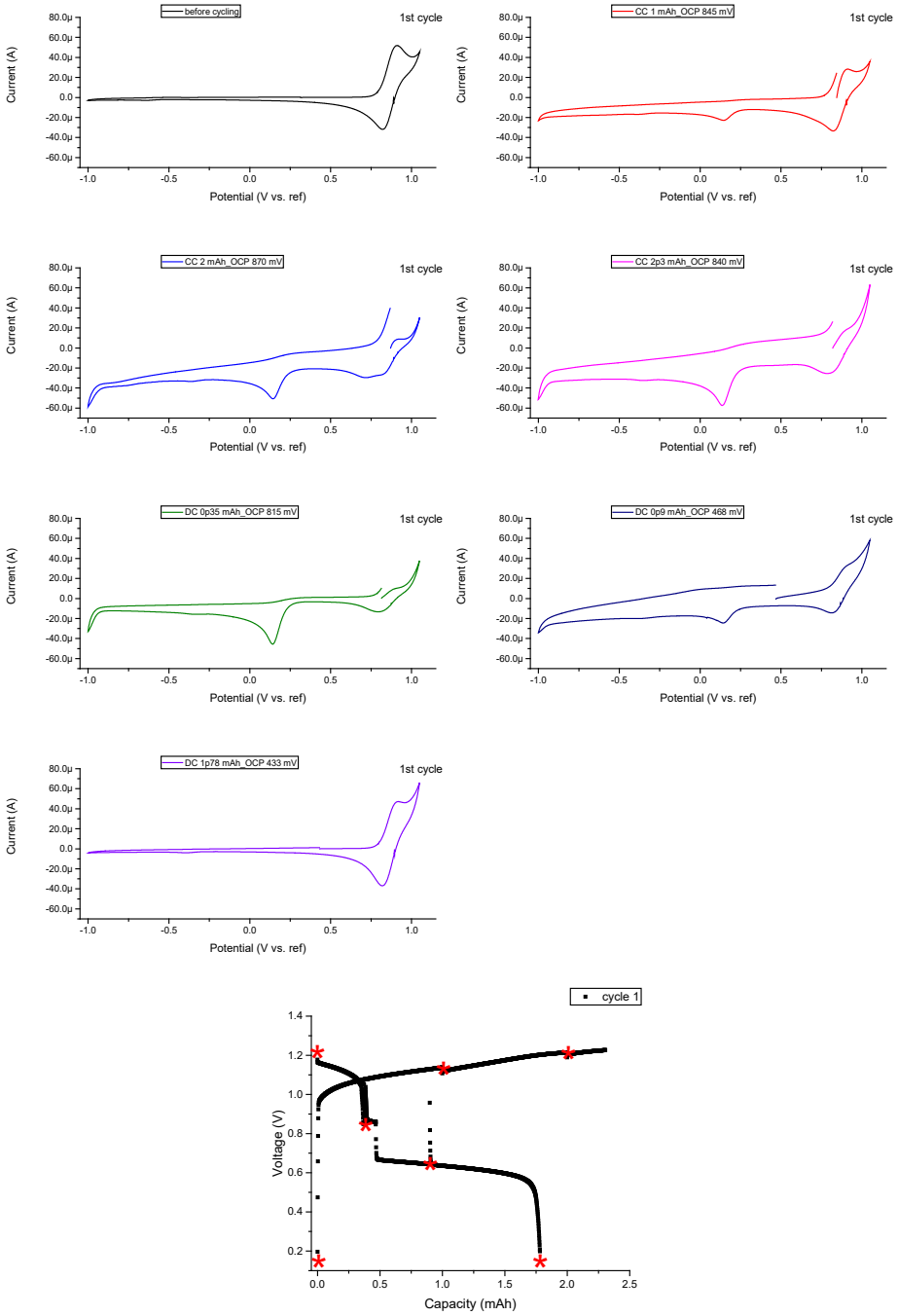

Figure 32. CVs at different stages of charge in $[Fe(II)(bpy)_3]^{2+}$ posolyte storage tank at first battery cycle and the battery cycle showing the places of measured CVs on the voltage-capacity curve.[v]

In **Fig 32**, the redox peak of the iron complex is at 0.86 V *vs.* Ag/AgCl. The oxidation and the reduction currents of the monomer decrease as the battery is charged. During discharge, the redox current peak of the monomer increases and after full discharge, the redox peak currents of the Fe complex pair return to the starting values. The dimer reduction peak at ca. 130 mV *vs.* Ag/AgCl increases upon charge and disappears at the end of discharge. More current profiles of these in the studied battery cycles have been presented in the SI of **publication V**.

Another interesting observation is the oxidation peak occurring in proximity to the oxidation of the monomer, partly overlapping the oxidation of the monomer and increasing its current in the later cycles. This oxidation seems to come closer or increase in value during charge and after discharge, and its peak is seen at a higher potential range to originate ca. 300 mV higher potential than the monomer oxidation peak. One option is that this is ligand oxidation. The ligand oxidation is known for some iron bpy complexes to be at the proximity of the oxidation of the iron complex, such as for $[Fe(II)(Dcbpy)_3]^{4-}$ at 0.97 V vs. Ag/AgCl,[49] and Dcbpy (4,4´-dicarboxylate-bpy) ca. 1.1 V vs. Ag/AgCl.[48] The oxidation peak in the experimental CVs could therefore indicate free ligands due to dimer formation releasing ligands. This would in addition, correspond to the experimental observations and is a strong candidate also when considering the ligand side reaction presented earlier in section 2.2.2.3 and the UV-Vis data in section 8.1.

This additional oxidation peak also seems to be the reason for an extra reduction peak located at 0.71 V *vs.* Ag/AgCl, which is ca. 100 mV lower in potential than the reduction peak of the iron complex redox pair. This reduction seems to be present only when the additional oxidation occurs at higher potentials than the Fe(II) complex oxidation peak. These reactions are presented in **Fig 33**. This signal seems to correspond to oxidation/reduction of the free ligand with slow kinetics.

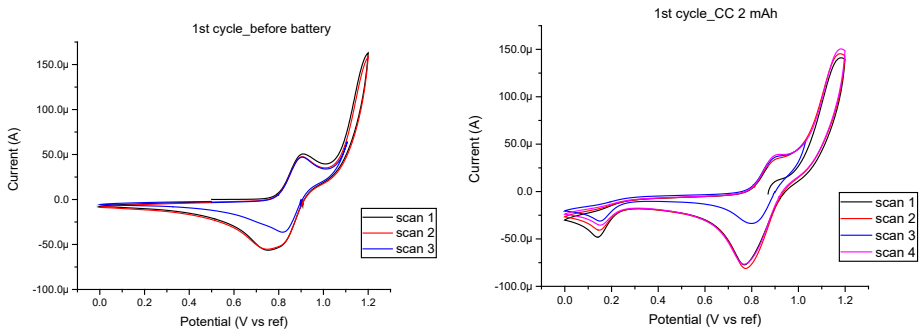

Figure 33. CVs in $[Fe(II)(bpy)_3]^{2+}$ posolyte storage tank at the first battery cycle before the cycle and at 2 mAh (theoretical capacity) charged.[V]

Half-cell OCP was recorded with the CVs measured in the storage tank of the $[Fe(II)(bpy)_3]^{2+}$ to obtain information on the half-cell SOC. However, the dimer decreases the OCP value of the posolyte solution drastically. Therefore, the OCP values cannot be used to determine the SOC for this kind of compound. Unfortunately, the additional oxidation peak at a higher potential than the redox pair made it impossible to use simulations to determine the SOC via peak currents. However, the peak currents can be used to evaluate that there is no significant degradation since the peak currents remain similar (SI in **publication V**).

In the comparison of hexacyanoferrates and $[Fe(II)(bpy)_3]^{2+}$ systems and their applicability to be monitored during battery operation with OCP analysis and peak current with simulations, we can see that for the hexacyanoferrates, this method is more accurate. It can be used to determine SOC reliably in both ways. For more complicated systems, such as the studied $[Fe(II)(bpy)_3]^{2+}$, this method is not reliable. With higher current densities and minimizing the time for side reactions to occur, we could increase the accuracy of this method for $[Fe(II)(bpy)_3]^{2+}$. However, we do not believe this is practical in most cases, as FBs should be able to be monitored during operation when they are in a charged state for longer periods. However, the CVs obtained for $[Fe(II)(bpy)_3]^{2+}$ system during battery operation are very practical, as they indicate the complexity of the system and can distinguish the side reactions occurring, as well as monitor the viability of the monomer regardless the side reactions via peak current values after discharge, hence obtaining qualitative information on the viability of the monomer during FB operation.

8 Decomposition mechanism via CVs and spectroscopic methods

Due to the applicability of the cyclic voltammetry as a monitoring tool of the redox active species during battery operation, $[Fe(II)(phen)_3]^{2+}$ and $[Fe(II)(terpy)_2]^{2+}$ were also characterized in the charged state with this method, and the results were reported in **publication II**. UV-Vis measurements were taken on charged and discharged states to obtain information on their changes spectroscopically. Also $[Fe(II)(bpy)_3]^{2+}$ results are discussed here with the CVs presented earlier, as in **publication V**.

8.1 $[Fe(II)(bpy)_3]^{2+}$

$[Fe(II)(bpy)_3]^{2+}$ CVs during battery operation were given in the previous section and in **publication V**, and we can see the dimer reduction peak form during charge and disappear during discharge. This mixture at the charged state contains the charged monomer and chemically formed dimer with the dissociated ligands. The UV-Vis samples were taken on the charged state and discharged state, and are provided below in **Fig 34**. The battery cycle of these samples was number 616.

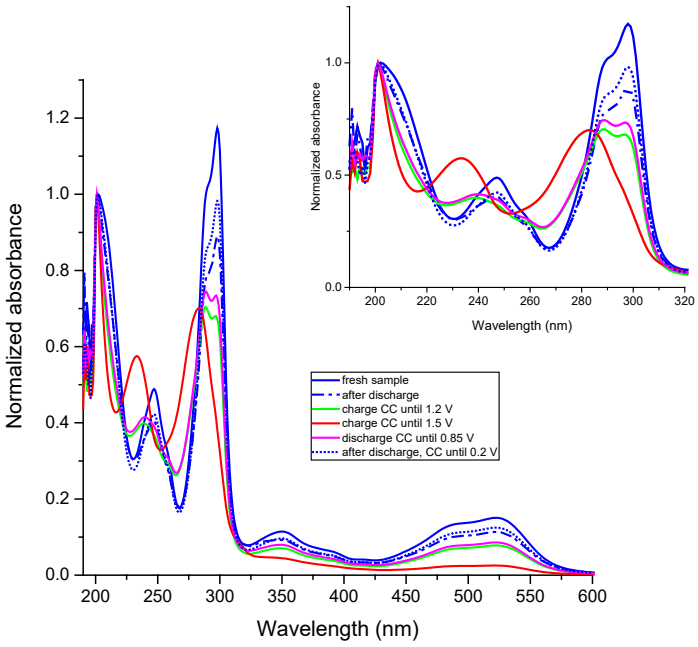

Figure 34. UV-Vis spectra of the $[Fe(II)(bpy)_3]^{2+}$ battery electrolyte at different states of battery cycling. The wavelengths of 190-600 nm show the absorbance events and the top right shows the changes around 300 nm more clearly. Voltages in the captions are from the battery data; 1.2 V is the cut-off for charging the monomer and 0.85 is the discharge voltage before the dimer plateau is discharged.[v]

The UV-Vis spectra of the starting solution and discharged have the same spectra, meaning the monomer is active in all and the discharge of the FB yields the monomer, even at battery cycle 616. Upon charge (CC until 1.2 V) and before the dimer discharge plateau, we can see the dimer present. The intensity of the peaks at ca. 290-300 nm shifts, as the one with higher wavelength decreases below the intensity of the lower wavelength peak, which is opposite to the starting material and after discharge. The peak at 247 nm shifts to 239 nm during charge. The broad absorbance peaks at ca. 500 nm and 350 nm decrease upon charge and increase during discharge. When we are overcharging the compound (CC until 1.5 V), we can see the spectra of the free ligand (ca. 280 and 235 nm, as in the literature (pH 5.8)),[85] meaning we have broken the complex by over-oxidizing. However, after the discharge of the Fe(III) center, we can see the monomer reformed in the solution. Therefore, over-oxidation and dimerization can be seen as rather reversible processes, as seen in the CVs and battery data.

The UV-Vis spectra correspond to the ones found in the literature.[56] The dimer formed was pure dimer in the solution, hence not comparing exactly to the one we

have, as we have the solution mixture from battery cycling. However, from the literature we can see the changes between $[Fe(II)(bpy)_3]^{2+}$ and its dimer are similar to the ones seen in our UV-Vis spectra; the lowering intensity of the absorbance peak at 300 nm upon dimerization, and absorbance peak at ca. 245 nm slight decrease in wavelength.

8.2 $[Fe(II)(phen)_3]^{2+}$

$[Fe(II)(phen)_3]^{2+}$ was studied separately against fluorenone (as the longer battery cycling data presented) and against diquat, both in excess. Both also increase the pH on the negolyte side upon charging and discharging to 10. The data presented here is the one cycled against diquat for one cycle and originates from **publication II**. Charged $[Fe(II)(phen)_3]^{2+}$ (5 mM, 15 ml) was generated in FB in the constant current method, by using 1 mA/cm^2 current density. Charging was performed until the theoretical capacity of 2 mAh was reached, after which the CV and UV-Vis samples were taken.

CVs in charged and discharged states can be seen in **Fig 35**. The CV responses (and battery data) of $[Fe(II)(phen)_3]^{2+}$ show similar responses as for $[Fe(II)(bpy)_3]^{2+}$ in our experimental battery and CV data and in the literature.[56] The reduction peak at lower potentials in the experimental CVs is forming during the charge of $[Fe(II)(phen)_3]^{2+}$. It is located at lower potentials (0.12 V *vs.* Ag/AgCl) and is ca. 700 mV lower potential than the monomer redox pair. This corresponds to the battery data, where the higher and lower discharge plateaus are 600-700 mV separated from one another.

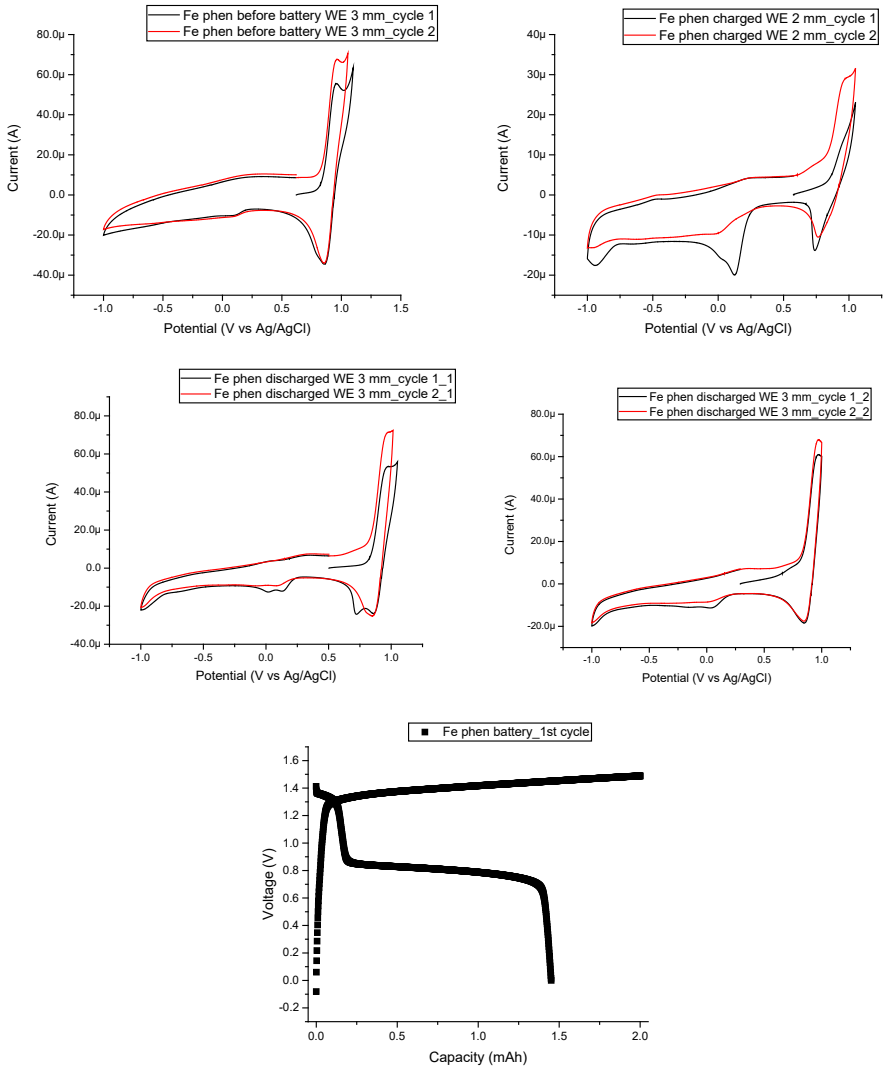

Figure 35. CVs of $[Fe(II)(phen)_3]^{2+}$ posolyte before the first battery cycle, after charge, and after discharge (2 graphs with different potential ranges) of the first cycle. Battery data of the cycle is presented in addition. The charged capacity was 2 mAh and the discharged capacity was 1.5 mAh. Note, that the WE diameters are given in the graphs, and they differ between 2 mm and 3 mm, therefore the currents are not directly comparable.[II]

UV-Vis data are given in **Fig 36**. We can see that there are structural changes during battery operation. The UV-Vis spectra of $[Fe(II)(phen)_3]^{2+}$ show the broad absorbance peak at 500 nm to disappear during charge. However, there is no formation of blue $[Fe(III)(phen)_3]^{3+}$ absorbance peak at the 600-700 nm wavelength range. This phenomenon has been noted in the literature,[86] where they concluded the

reduction step necessary in the regeneration of $[Fe(II)(phen)_3]^{2+}$ species, explaining the need to use the lower discharge cut-off for discharge, as we also detected in our battery studies. Additionally. the formation of $[Fe(III)(phen)_3]^{3+}$ is not preferred, but instead, the μ-O-dimer is.[87]

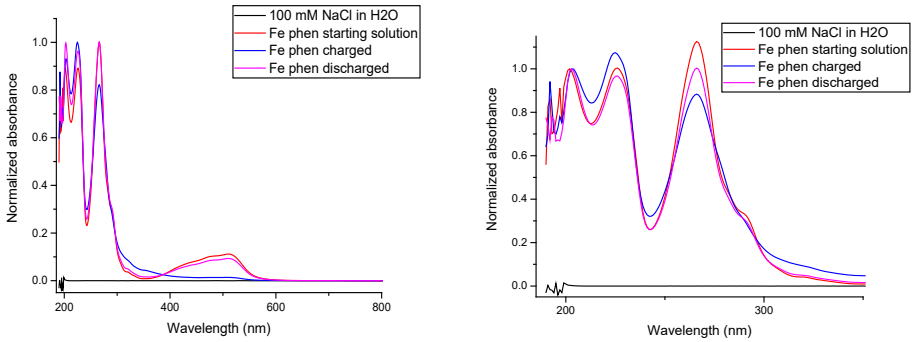

Figure 36. UV-Vis spectra of $[Fe(II)(phen)_3]^{2+}$ posolyte before the first battery cycle, after charge, and after discharge of the first cycle. On the left is a wider wavelength range, and on the right the absorbance peaks between 200-300 nm. Corresponding battery cycle data was presented in the previous figure.[II]

When comparing the changes in the UV-Vis spectra to the changes in $[Fe(II)(bpy)_3]^{2+}$ and its μ-O-dimer spectra, we can see similarities. The absorbance peak at 266 nm decreases upon oxidation, and the wavelength of absorbance spectra at 226 nm has a slight decrease.[56] Color change from deep red to brown-yellow solution is also noted experimentally and linked in the literature for dimer formation.[86] With this evidencing with UV-Vis, CVs, battery studies, color change, and ultimately literature acknowledgment of energetically favored formation of μ-O-dimer of oxidized $[Fe(II)(phen)_3]^{2+}$, we can conclude that we have dimer present in the charged state and it is the reason of low voltage efficiency of $[Fe(II)(phen)_3]^{2+}$ battery. It is suggested that the decomposition route of $[Fe(II)(phen)_3]^{2+}$ during charge and discharge might resemble the one presented in section 2.2.2.3, which relies on decomposition mechanisms of similarly structured $[Fe(II)(bpy)_3]^{2+}$ presented in the literature. Based on this, the forming charge plateau at lower voltage in the battery studies most likely originates from one ligand lost species of $[Fe(II)(phen)_3]^{2+}$, as noted earlier in section 6.2.

8.3 $[Fe(II)(terpy)_2]^{2+}$

Generation of $[Fe(II)(terpy)_2]^{2+}$ in the charged state was done according to the procedure presented in the previous section to $[Fe(II)(phen)_3]^{2+}$: the battery against diquat was charged with constant current until theoretical capacity (2 mAh) was reached, after which it was discharged, and 1.5 mAh was discharged on the first cycle. Results were reported in **publication II** and its SI.

The CVs at charged and discharged states are given in **Fig 37**. They show similar responses as $[Fe(II)(phen)_3]^{2+}$ and $[Fe(II)(bpy)_3]^{2+}$ during charge and discharge. The reduction peak forming during charge is located at 0.15 V *vs.* Ag/AgCl, which is ca. 700 mV lower potential than of the monomer. This follows the difference between the discharge plateaus during battery cycling (600-700 mV).

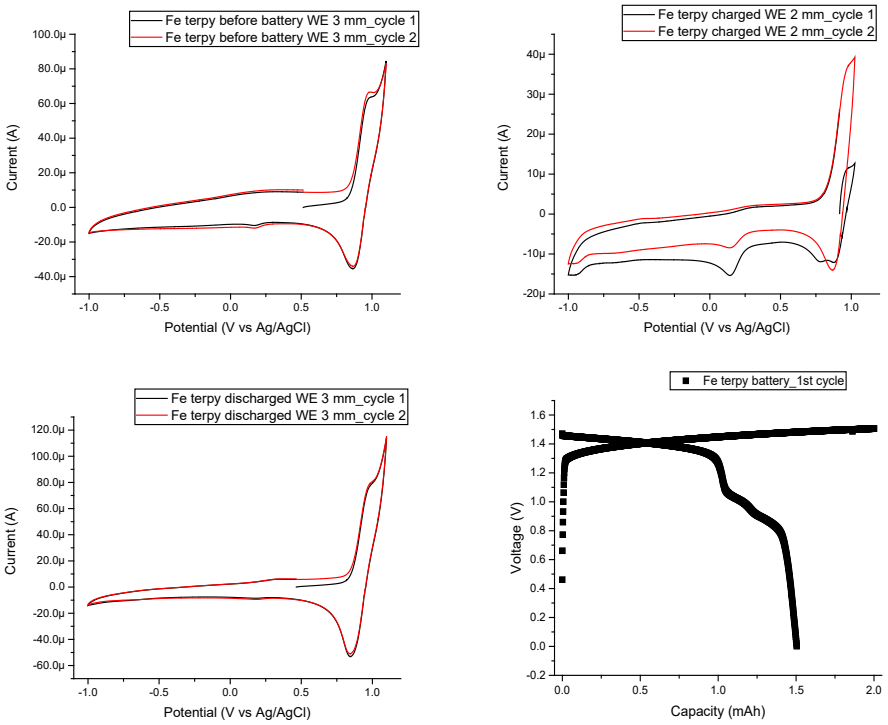

Figure 37. CVs of $[Fe(II)(terpy)_2]^{2+}$ posolyte before the first battery cycle, after charge, and after discharge (2 graphs with different potential ranges) of the first cycle. Battery data of the cycle is presented in addition. Charged capacity was 2 mAh and discharged capacity was 1.5 mAh. Note, that the WE diameters are given in the graph, and they differ between 2 mm and 3 mm, therefore the currents are not directly comparable.[II]

The UV-Vis samples were taken at the charged and discharged states. Spectra of these are given in **Fig 38**. The broad absorbance peak at ca. 550 nm decreases in half

intensity upon charge. The battery data of approximately 1:1 ratio of dimer and monomer during the discharge might explain the intensity decrease to half in normalized data. Absorbance peaks at 319 nm and ca. 275 decrease in intensity during charge, similarly to $[Fe(II)(bpy)_3]^{2+}$ and its dimer. There is no literature about the dimerization of $[Fe(II)(terpy)_2]^{2+}$, but the experimental data (CVs, UV-Vis, battery discharge plateaus, resembling metal complex structure to $[Fe(II)(bpy)_3]^{2+}$) are indications that dimerization is a possible side reaction to this compound. The multiple lower potential discharge plateaus are most likely to represent reorganization energies of the same structure. $[Fe(II)(terpy)_2]^{2+}$, has tridentate ligands and therefore 3 coordination sites available upon loss of a ligand for dimerization.

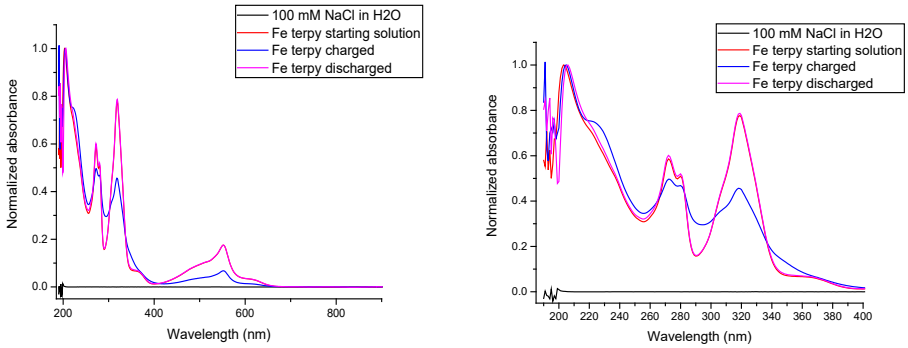

Figure 38. UV-Vis spectra of $[Fe(II)(terpy)_2]^{2+}$ posolyte before the first battery cycle, after charge, and after discharge of the first cycle. On the left is a wider wavelength range, and on the right the absorbance peaks between 200-400 nm. Corresponding battery cycle data was presented in the previous figure.[II]

8.4 Comparison

Similarly structured $[Fe(II)(bpy)_3]^{2+}$, $[Fe(II)(phen)_3]^{2+}$, and $[Fe(II)(terpy)_2]^{2+}$ might all be going through dimerization during battery studies. For $[Fe(II)(bpy)_3]^{2+}$ it has been proven to occur during FB cycling, and for $[Fe(II)(phen)_3]^{2+}$ the literature acknowledges the dimer formation. For these 2, we can state with rather certainty, that dimerization is the reason for low energy efficiency in FBs due to the dimer being discharged at a lower voltage than the monomer is being charged. The decomposition mechanism presented in section 2.2.2.3 is therefore most likely valid for both. In addition to multiple discharge plateaus, CVs during charge, and UV-Vis data, battery studies also show the additional charge plateau at lower voltage for all of the studied compounds. This most likely originates from one ligand lost species

in all three compounds. Therefore, all can be suggested to undergo ligand dissociation and dimerization as presented in section 2.2.2.3.

The CVs run during battery cycling show the oxidation of most likely the ligand at proximity to the metal complexes. This might cause irreversibility in the regeneration of the monomers as they need to coordinate a ligand after dimer discharge. If free ligands undergo side reactions, such as electrochemical oxidation, due to the inability to separate the oxidation processes of the monomer and the ligand properly, these complexes might lose stability due to ligand side reactions.

9 Summary/Conclusions

Several iron(II) complexes with bpy (**publication I**), phen (**publication II**), and terpy (**publication II**) ligands with various functional groups, Fe(II) with a combination of bpy and CN ligands ($[Fe(II)(bpy)(CN)_4]^{2-}$), and $[Ti(IV)(ncat)_3]^{2-}$ (**publication III**) were tested for aqueous flow battery applications. Suitable redox potentials were obtained: 0.57–1.29 V *vs.* SHE for posolytes and the only studied negolyte $[Ti(IV)(ncat)_3]^{2-}$ had a redox potential of -1.18 V *vs.* SHE. Derivations of the ligands of bpy, phen, and terpy all showed that EDGs adjusted the $E^{0'}$ to more negative potentials and EWDs to an opposite way from the non-substituted Fe(II) complex. This relates to the changing electron density near the iron(II) center; with EDGs the iron(II) environment is more negative than with the non-substituted and therefore oxidation of the Fe(II) is easier, whereas the opposite occurs when the functional groups are EWGs.

Simulations of the experimental cyclic voltammograms enable the evaluation of the redox reaction kinetics and the stability of the iron complexes (**publications I, II, V**). However, rising baseline, adsorption, and the possible other reactions overlapping the redox pair response are causing deviations to the obtained values. k^0 is a very sensitive value, since it can have large fluctuations with small visible changes in the CVs: uncertainty is approximately 50 % for k^0 values in the range of 10^{-3} to 10^{-2} cm/s. The D values and k_c values rely on the possible other events on the CV, such as rising baseline or other possible overlapping redox reactions, hence causing deviation into them. D values calculated with Randles-Ševčík and the COMSOL model are in agreement. For $[Fe(II)(bpy)_3]^{2+}$ we could see a difference between different counterions with an explanation from the literature and the D values were also comparable to those found in the literature. This validates using the model to evaluate these values (**publication I**). k_c values could be determined more reliably for the $[Fe(II)(phen)_3]^{2+}$ and $[Fe(II)(terpy)_2]^{2+}$ complexes if the baseline and other reactions were implemented in the simulation model, as their effect on the chemical reaction rate was too great (**publication II**). However, baseline contribution is rather hard to remove in experimental work at high potentials, and including the side reactions to the model would require detailed information on their

nature and kinetics, which we do not have. However, the model can be used to evaluate the kinetic parameters.

Battery studies of $[Fe(II)(bpy)_3]^{2+}$, $[Fe(II)(DMe\text{-}bpy)_3]^{2+}$, $[Fe(II)(bpy)(CN)_4]^{2-}$, $[Fe(II)(phen)_3]^{2+}$, $[Fe(II)(DMe\text{-}phen)_3]^{2+}$ and $[Fe(II)(terpy)_2]^{2+}$ showed two or more discharge plateaus with significant voltage drop during discharge, but $[Fe(II)(bpy)(CN)_4]^{2-}$ showed only one discharge plateau. The lowest capacity decays were 0.0099 % per cycle for $[Fe(II)(bpy)(CN)_4]^{2-}$ and 0.06 % per cycle for $[Fe(II)(DMe\text{-}phen)_3]^{2+}$. Voltage drop upon discharge leads to poor energy efficiency and is not optimal for FB operation. Therefore, further ligand design is needed, and asymmetry needs to be added to the metal complex structures to increase stability and avoid the voltage drop during discharge originating from side reactions.

Cyclic voltammetry during battery operation (**publication V**) is a simple and inexpensive tool to obtain information on the redox processes occurring in the storage tanks. The peak currents can be utilized to obtain information on the redox events and the SOC via simulations. SOC can also be calculated based on simple half-cell OCP measurements. We can obtain information on self-discharge and decomposition, as well as the closeness of other redox processes for complexes, and these can affect the stability of the compounds during battery cycling. The closeness of the ligand oxidation and of other additional redox events might not be visible in battery studies; therefore, implementing a CV measurement on storage tanks gives us additional information on the events during FB operation. Obtaining CVs during charged and discharged states is a practical in situ monitoring tool for SOC and state of health monitoring for the FB electrolytes individually from one another.

CVs measured in storage tanks coupled with UV-Vis during different states of charge suggest that dimerization occurs in all the studied compounds exhibiting discharge during battery studies in 2 plateaus (**publications II and V**). Most likely, the reactions during charge and discharge follow a similar decomposition mechanism as proven to $[Fe(II)(bpy)_3]^{2+}$, leading to ligand dissociation and dimerization with possible ligand side reactions such as oxidation at the proximity of the monomer oxidation.

This thesis aimed to screen possible candidates for aqueous flow battery electrolytes and to provide experimental data for computational modeling to obtain information on the redox potentials of metal complex candidates for FBs. Suitable candidates in terms of redox potentials were found, but their performance in lab-scale flow batteries was mostly not suitable for FBs due to observed side reactions and the resulting voltage drop during discharge, leading to poor energy efficiency with the studied $[Fe(II)(bpy)_3]^{2+}$, $[Fe(II)(phen)_3]^{2+}$ and $[Fe(II)(terpy)_2]^{2+}$ compounds. $[Fe(II)(bpy)(CN)_4]^{2-}$ was an exception; however, these results would need to be confirmed in a higher concentration battery. The COMSOL model to simulate electron transfer kinetics of CVs does not work for all compounds, and it is sensitive

to the changes in the baseline, which might be caused by possible ongoing side reactions, adsorption, OER, and ligand oxidation. Implementing these reactions to the model would improve its accuracy, but it would require knowing the kinetics and nature of the interfering reactions, making it rather challenging. However, the model can be used in some cases accurately, while apparent rates can be obtained in other cases. Additionally, implementing CV measurements on the half-cells gave us a suitable tool to monitor the SOC via OCP and simulations of the CV peak current, and to obtain information on the redox processes during the charge and discharge of the FB, revealing the redox active side reactions of the charged species.

In the future, density functional theory should be utilized further to obtain redox potentials of FB candidates to speed up the experimental work. Based on my results and the literature, the focus should be on obtaining asymmetric metal complexes for improved stability and solubility in water. In addition, experimental fast screening techniques should be utilized further. Therefore, my future work will focus on fast screening of redox potentials of metal complexes and finding a stabilizing effect to protect the Fe(III) center from side reactions via asymmetric ligand design and functional group design for iron complexes. With an asymmetric metal complex design, I think it is possible to obtain highly soluble compounds with high redox potential and stability, and these metal complexes can compete with the best-performing FB materials available at the moment.

Acknowledgements

Firstly, I want to acknowledge the University of Turku and the Materials Engineering unit for enabling the thesis work. In addition, I want to acknowledge the financial support gathered by my supervisor from Jane ja Aatos Erkon säätiö and Teknologiateollisuuden 100-vuotissäätiö through the Future Makers program for the Digipower project, from European Union for the DualFlow project, and the financial support via personal grants from the University of Turku Graduate School (Finalizing the doctoral thesis and Travel); all of these have enabled me to work on my thesis for the past few years and gain connections and knowledge while working on interesting projects.

I want to thank Pekka for giving me an exciting topic to work on, supervising the work and being there with advice every time it was needed, with some additional reminders to also take rest. Pekka is a kind person with answers to everything, and I appreciate the freedom he gives to follow one´s own ideas. I want to thank the network and collaborators he introduced me to, and also the possibility to travel to conferences, where I was able to present our research results and have interesting conversations on research. I also want to thank my other supervisor Ulriika for listening and giving advice. In addition, I want to thank Mikael and his team for keeping the labs up and running, hence enabling the research in labs. I would like to thank the co-authors in the published papers in our unit and in the collaborating universities (University of Jyväskylä and Aalto).

Our research group has awesome people in it, and I want to thank Jenni, Gabriel and Kimmo for all the discussions of work and not-work related topics; your support has been indescribable and the laughs and talks we have had together have kept me going during the hardest times. I am very happy to have met all of you and I cannot see how I could have done this without you all. I have also met some great people in our research group who have already continued to other jobs or universities. Still, I want to thank Jonnathan, Mahdi, Cedrik, Santiago and Juan for their general positivity and work attitude, and for all the talks we have had and will continue to have. I have very much liked working with you all and also spending time with you outside work. In general, I have learned something important from all of you.

Last but not least, I want to thank my mum, dad, sister and Urho for all the love and support. My family has always believed that I can do this and they have been very supportive in countless ways during this journey. Urho has been helping me in taking me for walks to get some fresh air and showing me that just staring at things outside is one of the most relaxing activities. I want to thank Gabriel for helping me see things from a better perspective in hard times and helping me keep balance with all the support in work and personal life. I want to thank Jasmin for the days-of-fun and therapy sessions, Jenni for all the wool craziness, Laura, Teemu and Joni for the escape rooms and dinners; these activities have been very much needed to balance the stress of all this. Thank you to all who have helped me along the way; I could not have done this alone.

22.4.2025, Piikkiö

Jenna Hannonen

List of References

1. Nasajpour-Esfahani, N. *et al.* Comprehensive review of lithium-ion battery materials and development challenges. *Renewable and Sustainable Energy Reviews* **203**, 114783 (2024).
2. Li, X. & Palazzolo, A. A review of flywheel energy storage systems: state of the art and opportunities. *J Energy Storage* **46**, 103576 (2022).
3. Blakers, A., Stocks, M., Lu, B. & Cheng, C. A review of pumped hydro energy storage. *Progress in Energy* **3**, 022003 (2021).
4. Budt, M., Wolf, D., Span, R. & Yan, J. A review on compressed air energy storage: Basic principles, past milestones and recent developments. *Appl Energy* **170**, 250–268 (2016).
5. Dissanayake, K. & Kularatna-Abeywardana, D. A review of supercapacitors: Materials, technology, challenges, and renewable energy applications. *J Energy Storage* **96**, 112563 (2024).
6. May, G. J., Davidson, A. & Monahov, B. Lead batteries for utility energy storage: A review. *J Energy Storage* **15**, 145–157 (2018).
7. Elalfy, D. A., Gouda, E., Kotb, M. F., Bureš, V. & Sedhom, B. E. Comprehensive review of energy storage systems technologies, objectives, challenges, and future trends. *Energy Strategy Reviews* **54**, 101482 (2024).
8. Koohi-Fayegh, S. & Rosen, M. A. A review of energy storage types, applications and recent developments. *J Energy Storage* **27**, 101047 (2020).
9. Mitali, J., Dhinakaran, S. & Mohamad, A. A. Energy storage systems: a review. *Energy Storage and Saving* **1**, 166–216 (2022).
10. Elalfy, D. A., Gouda, E., Kotb, M. F., Bureš, V. & Sedhom, B. E. Comprehensive review of energy storage systems technologies, objectives, challenges, and future trends. *Energy Strategy Reviews* **54**, 101482 (2024).
11. Kumar, R. *et al.* Different energy storage techniques: recent advancements, applications, limitations, and efficient utilization of sustainable energy. *J Therm Anal Calorim* **149**, 1895–1933 (2024).
12. Soeder, D. J. Fossil Fuels and Climate Change. in *Fracking and the Environment* 155–185 (Springer International Publishing, Cham, 2021). doi:10.1007/978-3-030-59121-2_9.
13. Thaller, L. H. Electrically Rechargeable Redox Flow Cells, 9th Intersociety Energy Conversion Engineering Conference. in 924–928 (1974).
14. Thaller, L. Electrically rechargeable REDOX flow cell. [Fe/sup +3//Fe/sup +2/ and Cr/sup +2//Cr/sup +3/ couples]. (1976).
15. Thaller, L. Redox Flow Cell Energy Storage Systems, Terrestrial Energy Systems Conference. in 989 (1979).
16. Gahn, R. F., Hagedorn, N. H. & Johnson, J. A. Cycling Performance of the Iron-Chromium Redox Energy Storage System; National Aeronautics and Space Administration. in (1985).
17. Adams, G. B. Lockheed Missiles & Space Company, Inc., Electrically rechargeable battery, US Patent, 4,180,623A. (1979).
18. Skyllas-Kazacos, M., Rychcik, M., Robins, R. G., Fane, A. G. & Green, M. A. New All-Vanadium Redox Flow Cell. *J Electrochem Soc* **133**, 1057–1058 (1986).

19. Ulaganathan, M. *et al.* Recent Advancements in All-Vanadium Redox Flow Batteries. *Adv Mater Interfaces* **3**, (2016).
20. Hu, X., Zou, C., Zhang, C. & Li, Y. Technological Developments in Batteries: A Survey of Principal Roles, Types, and Management Needs. *IEEE Power and Energy Magazine* **15**, 20–31 (2017).
21. European Commission. *Study on the Critical Raw Materials for the EU 2023 – Final Report*. (2023).
22. Minke, C., Kunz, U. & Turek, T. Techno-economic assessment of novel vanadium redox flow batteries with large-area cells. *J Power Sources* **361**, 105–114 (2017).
23. Wang, W. *et al.* Recent progress in redox flow battery research and development. *Adv Funct Mater* **23**, 970–986 (2013).
24. Hogue, R. W. & Toghill, K. E. Metal coordination complexes in nonaqueous redox flow batteries. *Curr Opin Electrochem* **18**, 37–45 (2019).
25. Shoaib, M. *et al.* Advances in Redox Flow Batteries – A Comprehensive Review on Inorganic and Organic Electrolytes and Engineering Perspectives. *Adv Energy Mater* (2024) doi:10.1002/aenm.202400721.
26. Gong, K. *et al.* All-Soluble All-Iron Aqueous Redox-Flow Battery. *ACS Energy Lett* **1**, 89–93 (2016).
27. Belongia, S., Wang, X. & Zhang, X. Progresses and Perspectives of All-Iron Aqueous Redox Flow Batteries. *Adv Funct Mater* **34**, (2024).
28. Okazawa, A., Kakuchi, T., Kawai, K. & Okubo, M. Iron-based catholytes for aqueous redox-flow batteries. *APL Mater* **11**, (2023).
29. Nambafu, G. S. *et al.* Phosphonate-based iron complex for a cost-effective and long cycling aqueous iron redox flow battery. *Nat Commun* **15**, 2566 (2024).
30. Zhang, W., Lu, J. & Guo, Z. Challenges and future perspectives on sodium and potassium ion batteries for grid-scale energy storage. *Materials Today* **50**, 400–417 (2021).
31. Bai, H. & Song, Z. Lithium-ion battery, sodium-ion battery, or redox-flow battery: A comprehensive comparison in renewable energy systems. *J Power Sources* **580**, 233426 (2023).
32. Soloveichik, G. L. Flow Batteries: Current Status and Trends. *Chem Rev* **115**, 11533–11558 (2015).
33. Weber, S., Peters, J. F., Baumann, M. & Weil, M. Life Cycle Assessment of a Vanadium Redox Flow Battery. *Environ Sci Technol* **52**, 10864–10873 (2018).
34. da Silva Lima, L. *et al.* Life cycle assessment of lithium-ion batteries and vanadium redox flow batteries-based renewable energy storage systems. *Sustainable Energy Technologies and Assessments* **46**, 101286 (2021).
35. Hemmati, R. & Saboori, H. Emergence of hybrid energy storage systems in renewable energy and transport applications – A review. *Renewable and Sustainable Energy Reviews* **65**, 11–23 (2016).
36. Zumdahl, S. *Chemical Principles*. (2007).
37. Blau, F. Über neue organische Metallverbindungen. *Monatsh.Chem.* **19**, 647–689 (1898).
38. F. Blau. Die Destillation pyridinmonocarbonsaurer Salze. *Ber. Dtsch. Chem. Ges.* **21**, 1077–1078 (1888).
39. Hammett, L. P., Walden, G. H. & Chapman, R. P. A REVERSIBLE OXIDATION INDICATOR OF HIGH POTENTIAL ESPECIALLY ADAPTED TO OXIDIMETRIC TITRATIONS. *J. Am. Chem. Soc.* **53**, 3908 (1931).
40. Matsuda, Y. *et al.* A rechargeable redox battery utilizing ruthenium complexes with non-aqueous organic electrolyte. *J Appl Electrochem* **18**, 909–914 (1988).
41. Yang, C. *et al.* Designing Redox-Stable Cobalt–Polypyridyl Complexes for Redox Flow Batteries: Spin-Crossover Delocalizes Excess Charge. *Adv. Energy Mater.* **8**, 1–10 (2018).
42. Xing, X., Zhao, Y. & Li, Y. A non-aqueous redox flow battery based on tris(1,10-phenanthroline) complexes of iron(II) and cobalt(II). *J. Power Sources* **293**, 778–783 (2015).

43. Xing, X., Zhang, D. & Li, Y. A non-aqueous all-cobalt redox flow battery using 1,10-phenanthrolinecobalt(II) hexafluorophosphate as active species. *J. Power Sources* **279**, 205–209 (2015).
44. Mun, J. *et al.* Non-aqueous redox flow batteries with nickel and iron tris(2,2 ′-bipyridine) complex electrolyte. *Electrochem. Solid-State Lett.* **15**, A80–A82 (2012).
45. Mun, J. *et al.* Highly Soluble Tris(2,2'-bipyridine) Metal Bis(trifluoromethanesulfonyl)imide Complexes for High Energy Organic Redox Flow Batteries. *J. Electrochem. Soc.* **165**, A215–A219 (2018).
46. Vanýsek, P. *CRC Handbook of Chemistry and Physics, 89th Edition*. *Tables of Standard Electrode Potentials* vol. 18 (Marcel Dekker, 1978).
47. Chen, Y.-W. D., Santhanam, K. S. V & Bard, A. J. Solution Redox Couples for Electrochemical Energy Storage I. Iron (lll)-Iron (11) Complexes with O-Phenanthroline and Related Ligands. *J. Electrochem. Soc.* **128**, 1460–1467 (1981).
48. Li, X. *et al.* Symmetry-breaking design of an organic iron complex catholyte for a long cyclability aqueous organic redox flow battery. *Nat. Energy* **6**, 873–881 (2021).
49. Hannonen, J., Kiesilä, A., Mattinen, U., Pihko, P. M. & Peljo, P. Electrochemical characterization of redox activity and stability of various tris(2,2‘-bipyridine) derived complexes of iron(II) in aqueous solutions. *Journal of Electroanalytical Chemistry* **950**, (2023).
50. Luo, J. *et al.* Unprecedented Capacity and Stability of Ammonium Ferrocyanide Catholyte in pH Neutral Aqueous Redox Flow Batteries. *Joule* **3**, 149–163 (2019).
51. Kolthoff, I. M. & Pearson, E. A. Stability of potassium ferrocyanide solutions. *Industrial & Engineering Chemistry Analytical Edition* **3**, 381–382 (1931).
52. Gao, J. *et al.* A High Potential, Low Capacity Fade Rate Iron Complex Posolyte for Aqueous Organic Flow Batteries. *Adv Energy Mater* **12**, (2022).
53. Jing, Y., Gordon, R. G. & Aziz, M. J. Chapter 6.1 Aqueous organic flow batteries. in *Redox Flow Batteries. From Fundamentals to Applications.* (eds. Roth, C., Noack, J. & Skyllas-Kazacos, M.) vol. 2 (Weinheim: Wiley-VCH., 2023).
54. Carnelley, T. XXI. Chemical symmetry, or the influence of atomic arrangement on the physical properties of compounds . *Lond.Edinb.Dubl.Phil.Mag.* **13**, 180–193 (1882).
55. Carino, E. V. *et al.* BF3-promoted electrochemical properties of quinoxaline in propylene carbonate. *RSC Adv.* **5**, 18822–18831 (2015).
56. Holubowitch, N. E. & Nguyen, G. Dimerization of [FeIII(bpy)3]3+in Aqueous Solutions: Elucidating a Mechanism Based on Historical Proposals, Electrochemical Data, and Computational Free Energy Analysis. *Inorg Chem* **61**, 9541–9556 (2022).
57. Bard, A. J. & Faulkner, L. R. *Electrochemical Methods: Fundamentals and Applications*. (John Wiley & Sons Inc., 2001).
58. Murtomäki, L., Kallio, T., Lahtinen, R. & Kontturi, K. *Sähkökemia*. (Aalto-yliopiston teknillinen korkeakoulu, 2010).
59. Arévalo-Cid, P., Dias, P., Mendes, A. & Azevedo, J. Redox flow batteries: a new frontier on energy storage. *Sustain Energy Fuels* **5**, 5366–5419 (2021).
60. Wu, B., Aspers, R. L. E. G., Kentgens, A. P. M. & Zhao, E. W. Operando benchtop NMR reveals reaction intermediates and crossover in redox flow batteries. *Journal of Magnetic Resonance* **351**, 107448 (2023).
61. Zhao, E. W. *et al.* Coupled *In Situ* NMR and EPR Studies Reveal the Electron Transfer Rate and Electrolyte Decomposition in Redox Flow Batteries. *J Am Chem Soc* **143**, 1885–1895 (2021).
62. Nolte, O., Volodin, I. A., Stolze, C., Hager, M. D. & Schubert, U. S. Trust is good, control is better: a review on monitoring and characterization techniques for flow battery electrolytes. *Mater Horiz* **8**, 1866–1925 (2021).
63. Gandomi, Y. A. *et al.* Critical Review—Experimental Diagnostics and Material Characterization Techniques Used on Redox Flow Batteries. *J Electrochem Soc* **165**, A970–A1010 (2018).

64. Ghimire, P. C. *et al.* In-Situ Tools Used in Vanadium Redox Flow Battery Research—Review. *Batteries* **7**, 53 (2021).
65. Small, L. J., Pratt, H. D., Fujimoto, C. H. & Anderson, T. M. Diels Alder Polyphenylene Anion Exchange Membrane for Nonaqueous Redox Flow Batteries. *J Electrochem Soc* **163**, A5106–A5111 (2016).
66. Stolze, C., Meurer, J. P., Hager, M. D. & Schubert, U. S. An Amperometric, Temperature-Independent, and Calibration-Free Method for the Real-Time State-of-Charge Monitoring of Redox Flow Battery Electrolytes. *Chemistry of Materials* **31**, 5363–5369 (2019).
67. Neyhouse, B. J., Tenny, K. M., Chiang, Y.-M. & Brushett, F. R. Microelectrode-Based Sensor for Measuring *Operando* Active Species Concentrations in Redox Flow Cells. *ACS Appl Energy Mater* **4**, 13830–13840 (2021).
68. Volodin, I. A. *et al.* Beyond steady-state conditions: Chronoamperometric state-of-charge and state-of-health measurements in flow battery electrolytes. *Sens Actuators B Chem* **403**, 135101 (2024).
69. von Bülow, F. & Meisen, T. A review on methods for state of health forecasting of lithium-ion batteries applicable in real-world operational conditions. *J Energy Storage* **57**, 105978 (2023).
70. Xiao, Y. *et al.* A comprehensive review of the lithium-ion battery state of health prognosis methods combining aging mechanism analysis. *J Energy Storage* **65**, 107347 (2023).
71. Wiberg, C., Evenäs, L., Busch, M. & Ahlberg, E. Naphthalene diimides (NDI) in highly stable pH-neutral aqueous organic redox flow batteries. *Journal of Electroanalytical Chemistry* **896**, (2021).
72. Artault, M. *et al.* Azoniafluorenones: A New Family of Two-Electron Storage Electrolytes for Sustainable Near-Neutral pH Aqueous Organic Flow Battery. *Adv Energy Mater* 2401635 (2024) doi:10.1002/aenm.202401635.
73. Mouselly, M., Alawadhi, H. & Senthilkumar, S. T. Current status of ferro-/ferricyanide for redox flow batteries. *Curr Opin Electrochem* **48**, 101581 (2024).
74. Rahbani, N., de Silva, P. & Baudrin, E. Density Functional Theory-Based Protocol to Calculate the Redox Potentials of First-row Transition Metal Complexes for Aqueous Redox Targeting Flow Batteries. *ChemSusChem* **16**, (2023).
75. Kurapati, N., Pathirathna, P., Chen, R. & Amemiya, S. Voltammetric Measurement of Adsorption Isotherm for Ferrocene Derivatives on Highly Oriented Pyrolytic Graphite. *Anal Chem* **90**, 13632–13639 (2018).
76. Wopschall, R. H. & Shain, Irving. Effects of adsorption of electroactive species in stationary electrode polarography. *Anal Chem* **39**, 1514–1527 (1967).
77. Cammack, C. X., Pratt, H. D., Small, L. J. & Anderson, T. M. A higher voltage Fe(ii) bipyridine complex for non-aqueous redox flow batteries. *Dalton Trans.* **50**, 858–868 (2021).
78. Kuta, J. & Yeager, E. The influence of cations on the electrode kinetics of ferricyanide-ferrocyanide system on the rotating gold electrode. *Electroanalytical Chemistry and Interracial Electrochemistry* **59**, 110–112 (1975).
79. Bui, H. & Holubowitch, N. E. Isopropyl alcohol and copper hexacyanoferrate boost performance of the iron tris-bipyridine catholyte for near-neutral pH aqueous redox flow batteries. *Int. J. Energy Res.* **46**, 5864–5875 (2022).
80. Konopka, S. J. & McDuffle, B. Diffusion Coefficients of Ferri- and Ferrocyanide Ions in Aqueous Media, Using Twin-Electrode Thin-Layer Electrochemistry. *Anal Chem* **42**, 1741–1746 (1970).
81. Reiter, J., Uhlířová, T. & Owen, J. R. Electrochemical behaviour of hexacyanoferrate(II)/(III) and ferrocene/ferricinium in lyotropic liquid crystals of polyoxyethylene (10) cetylether (Brij 56). *Journal of Electroanalytical Chemistry* **646**, 18–23 (2010).
82. Eifert, L., Banerjee, R., Jusys, Z. & Zeis, R. Characterization of Carbon Felt Electrodes for Vanadium Redox Flow Batteries: Impact of Treatment Methods. *J Electrochem Soc* **165**, A2577–A2586 (2018).

83. Fell, E. M. *et al.* Long-Term Stability of Ferri-/Ferrocyanide as an Electroactive Component for Redox Flow Battery Applications: On the Origin of Apparent Capacity Fade. *J Electrochem Soc* **170**, 070525 (2023).
84. Luo, J. *et al.* Unraveling pH dependent cycling stability of ferricyanide/ferrocyanide in redox flow batteries. *Nano Energy* **42**, 215–221 (2017).
85. Nakamoto, K. ULTRAVIOLET SPECTRA AND STRUCTURES OF 2,2'-BIPYRIDINE AND 2,2',2″-TERPYRIDINE IN AQUEOUS SOLUTION [1]. *J Phys Chem* **64**, 1420–1425 (1960).
86. Walczak, M. M. & Flynn, N. T. Spectroelectrochemical study of the generation of tris-(1,10-phenanthroline) iron(II/III) from μ-oxo-bis[aquabis(1,10-phenanthroline) iron(III)]. *Journal of Electroanalytical Chemistry* **441**, 43–49 (1998).
87. Plowman, J. E., Loehr, T. M., Schauer, C. K. & Anderson, O. P. Crystal and molecular structure of the (.mu.-oxo)bis[aquobis(phenanthroline)iron(III)] complex, a Raman spectroscopic model for the binuclear iron site in hemerythrin and ribonucleotide reductase. *Inorg Chem* **23**, 3553–3559 (1984).

TURUN
YLIOPISTO
UNIVERSITY
OF TURKU

Painosalama, Turku, Finland 2025

ISBN 978-952-02-0190-6 (PRINT)
ISBN 978-952-02-0191-3 (PDF)
ISSN 2736-9390 (Print)
ISSN 2736-9684 (Online)